1506
UNIVERSITÀ
DEGLI STUDI
DI URBINO
CARLO BO

Università degli Studi di Urbino Carlo Bo

Department of Pure and Applied Science

Ph.D. PROGRAMME in: **Research Methods in Science and Technology**

CYCLE: **XXXV**

DESIGN, SYNTHESIS AND CHARACTERIZATION OF POLYAMINE- AND SQUARAMIDE-BASED FLUORESCENT CHEMOSENSORS FOR SELECTIVE RECOGNITION OF ORGANIC MOLECULES AND METAL CATIONS IN SOLUTION

ACADEMIC DISCIPLINE: **CHIM/03**

Coordinator: Chiar.mo Prof. Alessandro Bogliolo

Supervisor: Chiar.mo Prof. Vieri Fusi

Co-Supervisor: Chiar.mo Prof. Luca Giorgi

Ph.D. Student: Luca Mancini

ACADEMIC YEAR: **2021/2022**

Contents

Abstract

The present thesis describes two classes of optical receptors able to be used as chemosensors for anionic species: the first class is constituted by seven squaramide-based system (**L1**-**L7**) and the second one lies to two tetraazapyridinophane systems (**L8**-**L9**).

Bis-squaramide ligands **L1-L4** (Scheme 1) bearing a dansyl moiety were synthesised and their potential applications as fluorescent probes were investigated towards non-steroidal anti-inflammatory drugs (NSAIDs) Naproxen (NPX) and Ketoprofen (KET). As mentioned, each ligand contains two squaramide units connected via a dipropylenamine spacer bearing a dansyl group as fluorescent signaling unit linked to the central nitrogen atom. The four ligands show different structural features: **L1** and **L2** have a macrocyclic topology to increase the rigidity and the pre-organization of the binding unit. In particular, **L1** is a 22-membered hexaazamacrocycle containing two dansyl groups and **L2** is an 18-membered pentaazamacrocycle containing only one dansyl unit. **L3** and **L4** are open-chain ligands in which each terminal squaramide units bear a benzyl group to increase the area of hydrophobic interaction (**L3**) or an indole ring to increase the number of hydrogen bonding (HB) donor sites (**L4**). The non-fluorescent ligand **L5**, reported in Scheme 1, showing the same macrocyclic topology of **L1** has been also studied for comparison. The aim of the study is to understand how and at which extent the molecular topology and the number of HB donors of the receptors influence the selectivity and the signaling efficiency towards the selected targets analytes NPX and KET in their anionic forms (NPX^- and KET^-, respectively, Scheme 1). Benzoate (BzO^-, Scheme 1) was also considered for the sake of comparison.

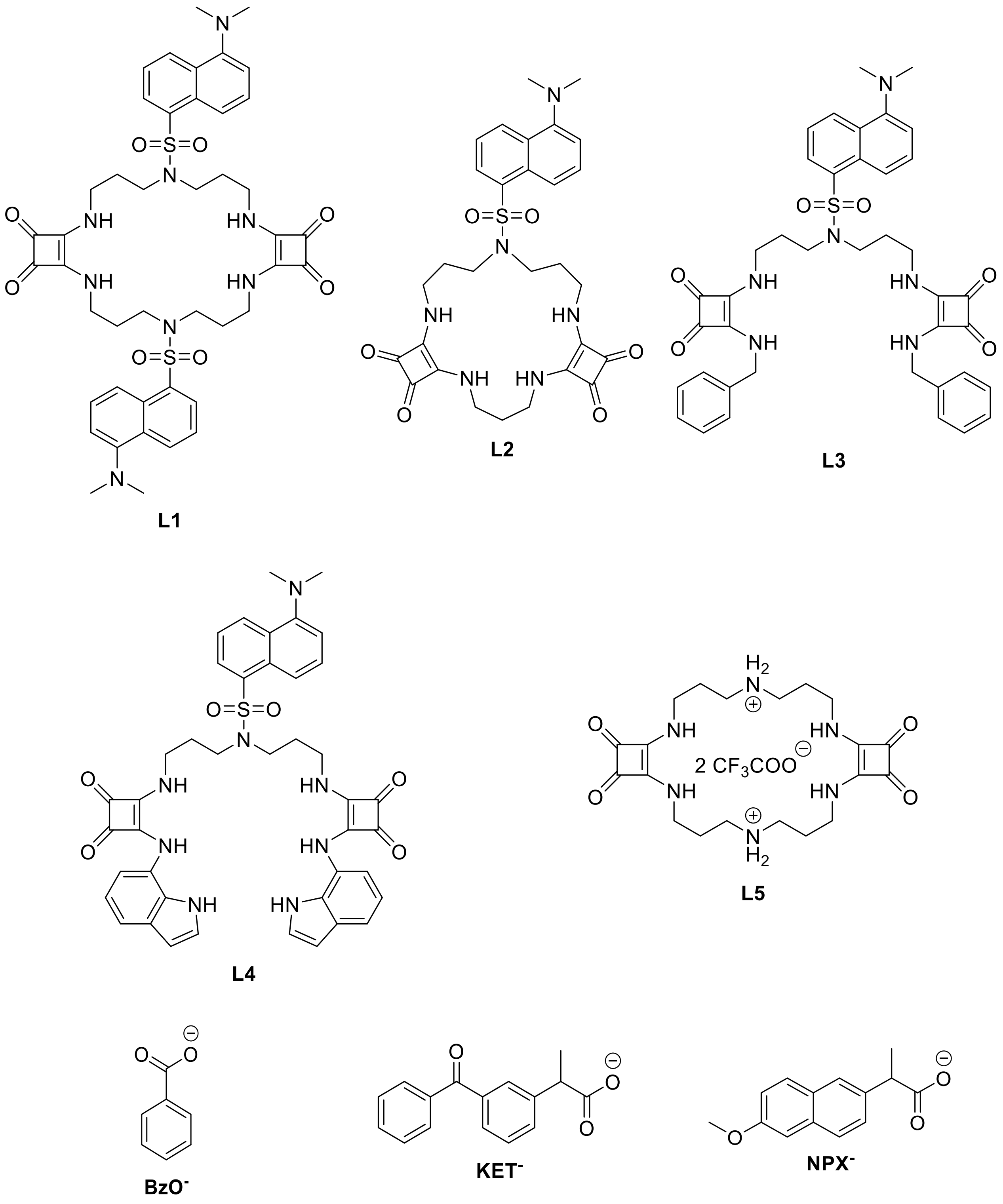

Scheme 1. Ligands **L1-L5** discussed in the thesis and their targets in anionic form.

The ligands **L6** and **L7** showed excellent ability to selectively bind NSAIDs through converging hydrogen bonds with a clear spectrophotometric output; donor groups are placed at a suitable distance to be able to coordinate an oxygen atom of the carboxylate group. **L6** and **L7**, reported in Scheme 2, represent the single-arm and the double-arm version of the same ligand. They are both open-chain sensors in which the coordinating unit is represented by a squaramide covalently bonded to a 7-amino-4-(trifluoromethyl)coumarin. While the squaramide moiety is responsible for the hydrogen bonding, the coumarin has the ability to actively participate in the coordination through hydrophobic interactions and aromatic stacking. In the case of **L6** the spacer that connects the two equivalent branches is a m-xylylenediamine, therefore a benzylamine was used for the synthesis of **L7**. The rationale in the design of these two ligands lies in looking for an eventual selectivity between the anions of four specific NSAIDs – Ibuprofen (IBU), Ketoprofen (KET), Diclofenac (DCL) and Naproxen (NPX), Scheme 2 – and a possible synergistic effect of the two branches in the case of the double sensor with respect to its single analogue.

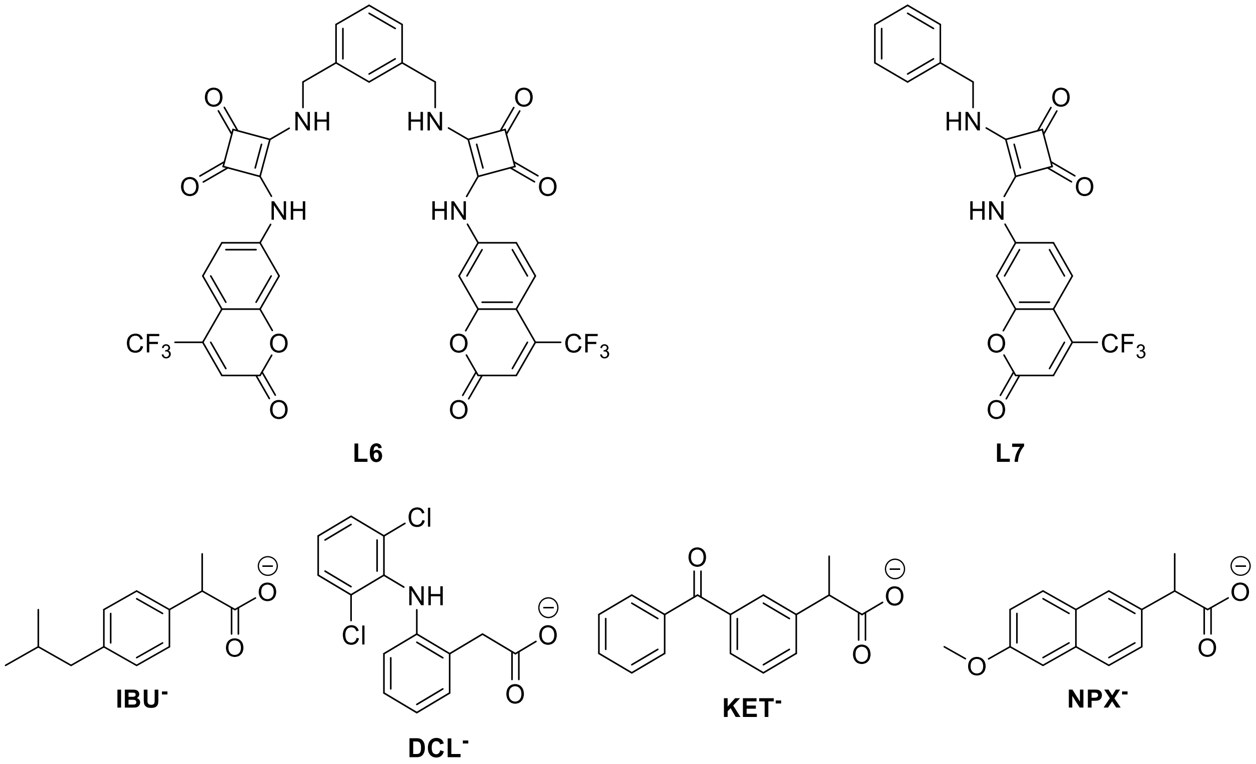

L6

L7

IBU$^-$

DCL$^-$

KET$^-$

NPX$^-$

Scheme 2. Ligands **L6** and **L7** discussed in the thesis and their targets in anionic form.

The receptor **L8** consists of two “scorpiand” polyamine subunits connected by a luminescent biphenol spacer. Each polyamine subunit is built up by annelation of a tosylated diethylentriamine (den) moiety with a 2,6-bis(bromethyl)pyridine in the presence of an alkaline carbonate as base in high dilution conditions. The receptor has been salified with HCl making it perfectly soluble in an aqueous environment as well as characterized by potentiometric means. The fluorescent spacer is a linker composed of 12 aromatic carbon atoms while the coordination polyazamacrocycles are 12-membered rings composed of 4 N and 8 C. These two units are connected by an N-methylethanamine. The coordination and the fluorescence behavior of the binuclear species [Zn_2**L**] in an aqueous environment both in the total pH range and in a buffered environment was studied. The focus of the project was to try to understand and explain the unusual fluorescence behavior of **L8** in the presence of Zn^{2+} using different characterization techniques. Preliminary studies have also been carried out in the presence of organic molecules such as L-aspartic acid (Asp), L-glutamic acid (Glu), succinic acid (Suc) and glutaric acid (Glt). **L8** and his targets are reported in Scheme 3.

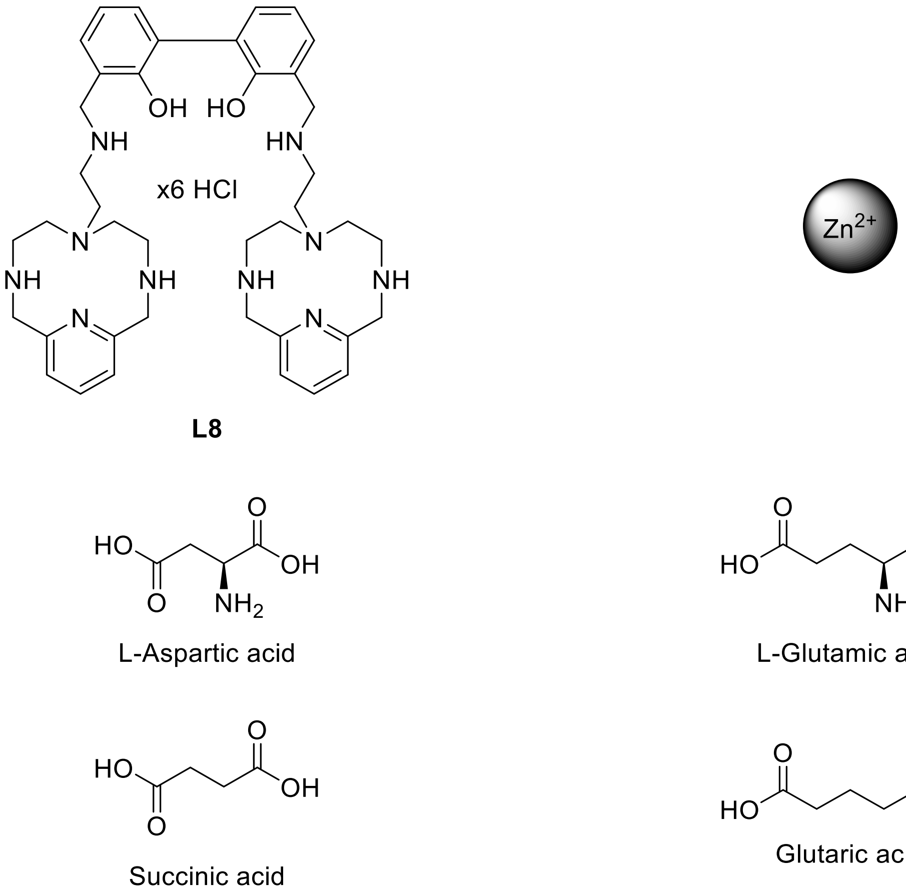

Scheme 3. Ligand **L8** discussed in the thesis and its targets.

The scorpiand-type polyamine chemosensor **L9** (Scheme 4), bearing a fluorescent acridine moiety as signalling unit, has been designed and synthesized to selectively recognize nucleotides in aqueous media. Similar to **L8**, **L9** has the same 12-membered polyamine macrocycle and this sensing material is connected to the acridinine-based fluorescent signal transducer via an N^1-ethylpropane-1,3-diamine chain. The elongation of the linker was done with the intention of increasing the coordination power of the sensor by giving it greater flexibility. The chosen nucleotides were those of the “triphosphate” series: ATP, GTP and UTP to which was also added the “monophosphate” GMP (Scheme 4).

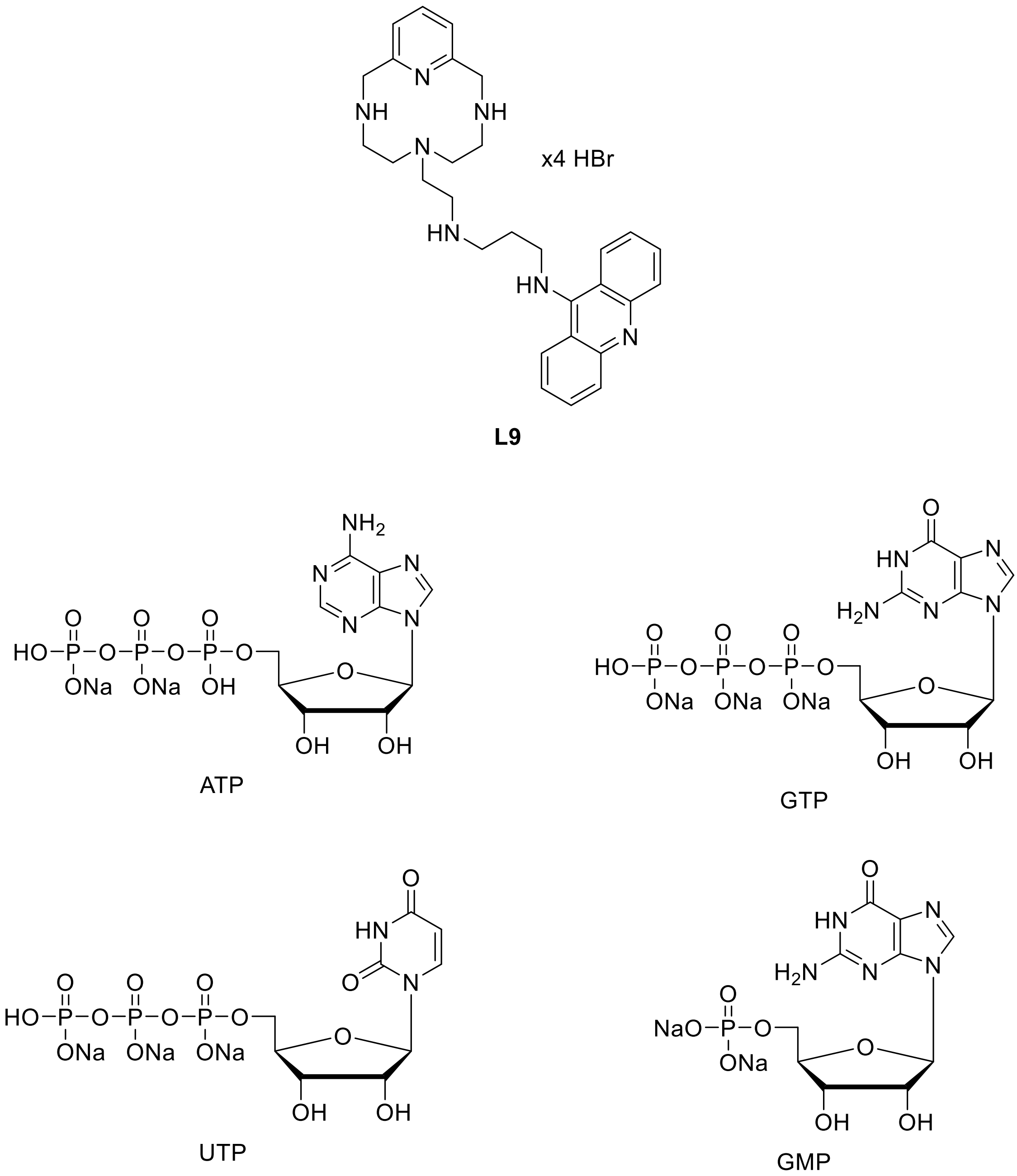

Scheme 4. Ligand **L9** discussed in the thesis and its targets.

Chapter 1 – Introduction

1.1 Supramolecular Chemistry

1.1.1 Definition of Supramolecular Chemistry and of Host-Guest

Supramolecular chemistry deals with highly complex organized entities that derive from the association of two or more chemical species held together by intermolecular forces. Its development requires the use of all theoretical and experimental resources of molecular chemistry combined with well-designed manipulations of non-covalent interactions, in such a way as to form entities called *supramolecules* with well-defined characteristics. This branch of chemistry is actually defined as "*chemistry of molecular assemblies and intermolecular bonds*" or, with its more classical expression, "*chemistry beyond the molecule*".[1]

The aforementioned chemical species are nothing more than a host and a guest. The *host* is defined as a molecular entity which possess *convergent* binding sites that give it the ability to bind, or even better to coordinate with a *guest*, a second molecular entity with *divergent* binding sites that with their counterparts lead to the formation of a *complex*.[2]

Hosts can be divided into two main classes: *cavitands* and *clathrands*, represented in Figure 1. The former have a permanent intramolecular cavity as an intrinsic molecular property and is recognizable both in solution and in the solid state. The latter, on the other hand, have an extramolecular cavity represented by the gaps between several host molecules and can therefore be found only in the solid or crystalline state. The host-guest aggregates formed by cavitands are called *cavitates*, while those formed by clathrands are called *clathrates*.

There is also a third situation in which two molecules can aggregate using non-covalent interactions but which do not fit with the description of host and guest: we speak of self-assembled aggregates, which exist both in solution and in the solid state.[3]

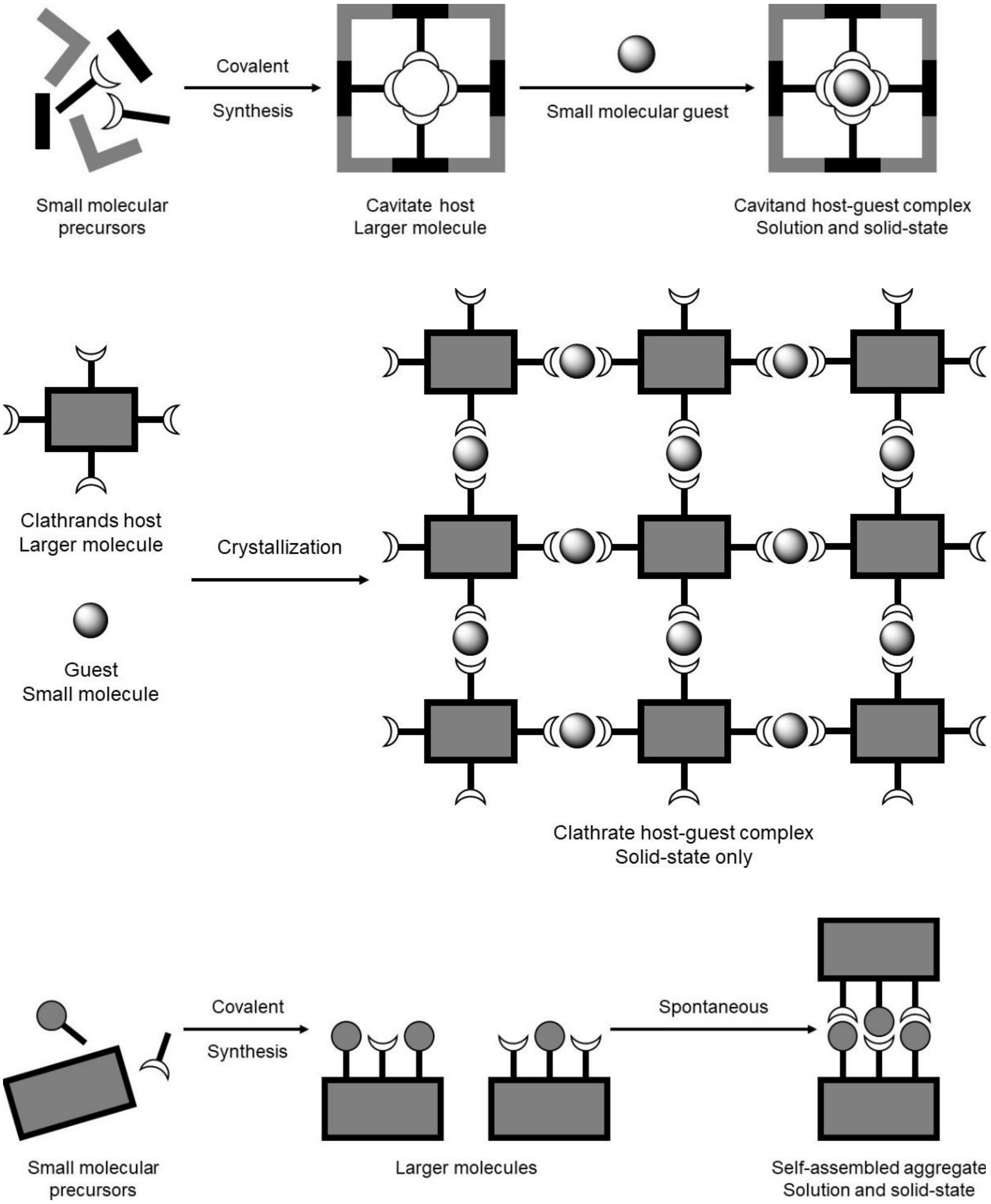

Figure 1. Classification of host-guest compounds.

1.1.2 Binding Constants: Definition, Use and Measurement

In thermodynamics the stability of a complex, in a given solvent and at a given temperature, is measured through the binding constant *K*. This parameter is dimensionless and is of fundamental importance in supramolecular chemistry for evaluating the affinity of a given host for a particular guest in solution. *K* is calculated as the equilibrium constant for the reaction:[4]

$$\mathrm{G(solvent)_n} + \mathrm{L} \rightleftarrows \mathrm{GL} + \mathrm{n(solvent)}$$

$$K = \frac{[\mathrm{GL}]}{[\mathrm{G(solvent)_n}][\mathrm{L}]}$$

$$\mathrm{G} = \text{Guest coordinated with n solvent molecules; } \mathrm{L} = \text{Host or ligand}$$

A host-guest complex is all the more stable the higher the binding constant is and this implies that at the equilibrium there will be a greater concentration of bound guest. In the event that the complexation involves more than one guest, it will be necessary to measure the *K* both for the complexes in the 1:1 ratio and for those in the 1:2 ratio.

$$\mathrm{G(solvent)_n} + \mathrm{L} \overset{K_1}{\rightleftarrows} \mathrm{GL} + \mathrm{n(solvent)}$$

$$\mathrm{G(solvent)_n} + \mathrm{GL} \overset{K_2}{\rightleftarrows} \mathrm{G_2L} + \mathrm{n(solvent)}$$

$$K_2 = \frac{[\mathrm{G_2L}]}{[\mathrm{G(solvent)_n}][\mathrm{GL}]}$$

When these conditions are satisfied is possible to define a global binding constant, *β*:

$$\beta = (K_1 * K_2)$$

Furthermore, binding constants are often reported in logarithmic function as log *K*:

$$\log \beta = \log\,(K_1 * K_2) = \log K_1 + \log K_2$$

Finally, these constants can also be defined in terms of rate constants *k* of the complexation and decomplexation reactions:

$$\mathrm{G(solvent)_n} + \mathrm{L} \underset{k_{-1}}{\overset{k_1}{\rightleftarrows}} \mathrm{GL} + \mathrm{n(solvent)}$$

$$K = \frac{k_1}{k_{-1}}$$

K can be calculated through all those experimental techniques that provide information about the concentration of the complex as a function of a variation in the concentration of the host or the guest. The following are the most used techniques to determine the binding constants, which are the same used in this experimental thesis.[5]

Potentiometric Titrations. In the case of ligands with acid-base properties, the protonation constants (and therefore the pK_a values) can be determined using pH electrodes to monitor a simple acid-base titration. Initially this will give the acid dissociation constant (pK_a) of the conjugate acid of the ligand, HL^+. The addition of a guest will then disturb the basicity of the ligand (ability to bind one or more protons) due to the competition between the guest and the H^+ for the non-binding electron pair(s) and consequently the shape of the titration curves.

Nuclear Magnetic Resonance (NMR) Titrations. If the exchange of complex and non-complex guests is slow on the NMR time scale, the binding constant can be roughly estimated using this technique. In an NMR titration, aliquots of a guest solution of known concentration are added to a known amount of host dissolved in a known amount of deuterated solvent, acquiring the spectrum at each single addition. The coordination of the guest affects the magnetic surroundings of the ligand nuclei causing changes in its chemical shift ($\Delta\delta$). Thanks to this it is possible to obtain information about the regioselectivity of the guest’s bond, by studying the nuclei most affected by the perturbation, and about the *K* by extrapolation from the curve obtained by plotting the $\Delta\delta$ as a function of the guest additions.

Fluorescence Titrations. In this type of titration, the measurements are based on the proportionality between the fluorescence intensity and the concentration of the fluorophore at low level of concentration (the fluorescent species can be both the guest and the host). What we are looking for is a variation in the intensity of the light emitted and/or a shift of the latter (by exciting the system at a fixed wavelength), that is an indication of an interaction between the two species in solution. Also in this case it is possible to obtain a K by graphing the fluorescence variations at the wavelength corresponding to the maximum emission intensity as a function of the titrant additions.

UV-Visible Titrations. With these spectroscopic titrations it is possible to monitor the intensity of an absorption band at a specific wavelength typical of the species. In order to calculate the K, a plot of the absorption intensity at that wavelength is generated as a function of the concentration of guest added to a host solution with a known and constant concentration. This technique also allows to observe the isosbestic points: areas of the spectrum in which the absorption intensity is constant during the titration and which allow to highlight the conversion of the free host in the complex without involving intermediate species.

1.2 Chemosensors

1.2.1 Definition and Properties

A *chemosensor* (or *ligand*, see Figure 2) is defined as a molecular device capable of transforming a chemical information, ranging from the concentration of a single component of the sample under analysis (cations, anions, neutral organic/inorganic/biological molecules) to the concentration of all the components of the entire matrix, in an analytically useful signal. Depending on the application of the sensor, it is possible to develop multiple strategies for signal transduction and among the most common systems, as well as those present in this thesis, we find photochemical sensors operating in UV-Visible and fluorescence spectroscopy. The changes in the photo-physical and physico-chemical properties of these chemosensors, following the interaction with the bound analyte, are due to the perturbation by the analyte of photoinduced processes such as electron transfer, charge transfer, energy transfer, formation or disappearance of excimers or exciplexes, etc.

The main components of these devices are basically three:

- The *sensing material* or *receptor unit*, which is the fragment involved in the process of recognizing the analyte with which it directly bonded
- The *signal transducer* or *signalling unit*, which produces a measurable signal upon the interaction with the analyte
- The *spacer*, that connects the receptor unit to the signalling system

Although all the components determine the performance of the final device, the sensing material is essential for the selectivity and, together with the signal transduction, for the sensitivity of the entire system. For this reason, the realization of a chemosensor requires a sophisticated chemical design based on classical organic synthesis. These two components can be linked directly to each other or connected via a third unit which is defined as a *spacer*: by connecting the receptor unit and the signalling unit together, it allows their electronic interaction and the regulation of their distance and spatial arrangement.

The broad diffusion of chemosensors is motivated by distinct advantages offered by the detection of the interaction in terms of *sensitivity, selectivity, response time, local observation* and *chemical stability of the system*. Sensitivity and selectivity are very important because the association process must be fast and reversible and the receptor must have a sufficiently high selectivity for the analyte targeted with respect to the possible interfering agents. Moreover, the higher the sensitivity, the lower the detection limit, which means that the system is able to detect the substrate even in samples in which it is present only in traces. Another fundamental feature is the response time since, depending on the technique used, the detection of the signal emitted when the guest is connected must be fast enough to make the experiment practical; in host-guest chemistry this factor is influenced by the kinetics of complex formation.

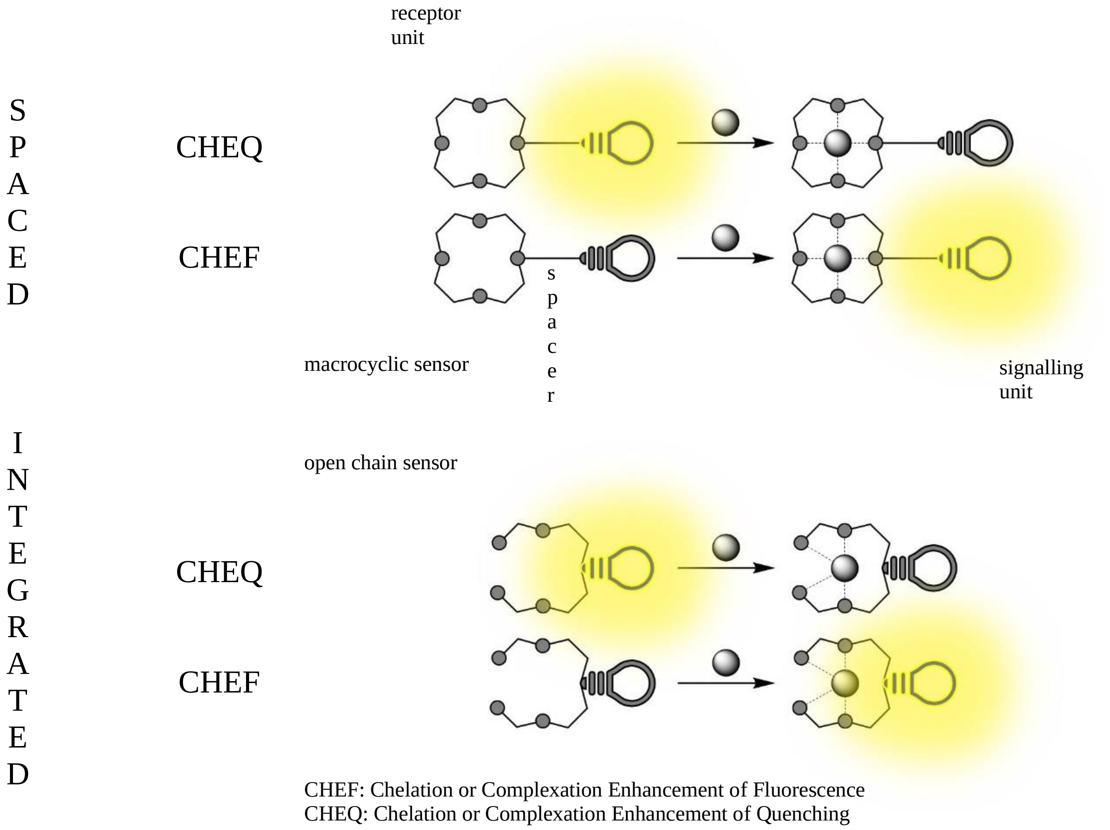

Figure 2. General schematic representation of a chemosensor.

1.2.2 Fluorescent Chemosensors and Fluorescence Mechanisms

Fluorescence is a highly versatile spectroscopic method, whose signal transduction provides results in real time and with the use of extremely low sensor and analytical concentrations (in the order of 10^{-6} M). Therefore, in the case of fluorescent chemosensors the signalling moiety of the molecular machine takes the name of *fluorophore* and the optical response generated by this unit, following the recognition event, is an optical signal whose characteristic is that of having an emission wavelength longer than that of excitation.[6]

As mentioned in the previous paragraphs, a fluorescent ligand must have the ability to signal the presence of a determined guest through changes in its fluorescence properties, that could be a variation in the emission intensity or in the wavelength, as well as the appearance of a new fluorescence band. In general, the coordination of the analyte to the ligand can result in an increase in the emission of fluorescence, called *Chelation* or *Complexation Enhancement Fluorescence effect (CHEF)*, or in a quenching of the same, called *Chelation* or *Complexation Enhancement Quenching effect (CHEQ)*; both effects can be coupled with a red- or a blue-shift of the emission band. The next paragraphs discuss the mechanisms underlying the signal transduction occurring upon the host-guest interaction.[7]

Paramagnetic Fluorescence Quenching. The presence of paramagnetic species in the proximity of a fluorophore promotes the *intersystem crossing (isc)*, from S1 to T1, a spin forbidden transition that in normal condition behaves as a very slow process. Subsequently the excited T1 state, having a long lifetime, is quenched by Stern Volmer collisional mechanism bringing to a partial or total quenching of the fluorescence (Figure 3). This phenomenon is the principal cause of the fluorescence quenching of ligands caused by the coordination to paramagnetic metal ions such as d^9 Cu^{2+}, d^5 Fe^{3+} and Co^{2+}, and d^1 Cr^{3+}.

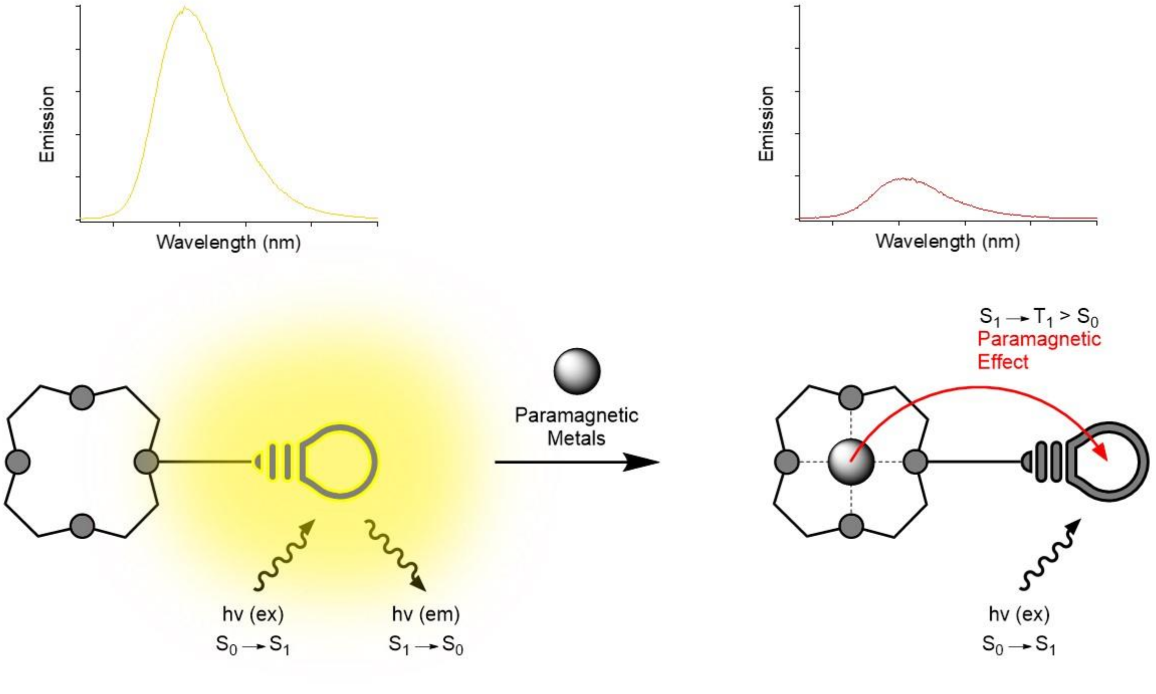

Figure 3. Paramagnetic fluorescence quenching mechanism.

Photoinduced Electron Transfer (PET).[8] PET, Figure 4, is a deactivation process that can be caused by an electron exchange occurring upon photoexcitation, in principle it involves an internal red-ox reaction between the excited state of the fluorophore and another species able to donate or to accept an electron. This is possible because in the excited state the properties of the molecules are quite different compared to those of the ground state and therefore, due to its higher energy content, an excited state is both a stronger reducing and oxidant than the corresponding ground state. An excited electron in the *lowest unoccupied molecular orbital (LUMO)* of an electron donor (D^*), formed upon photoirradiation of D, transfers to the LUMO of an electron acceptor (A) by triggering frontier orbital overlap interactions to form a radical ion pair ($D^{\bullet+}$, $A^{\bullet-}$) – *oxidative electron transfer*. On the other hand, an electron in the *highest occupied molecular orbital (HOMO)* of D transfers to the HOMO of A^* through frontier orbital overlap interactions, affording the same radical ion pair ($D^{\bullet+}$, $A^{\bullet-}$) – *reductive electron transfer*. In fluorescent sensors, PET takes place from a lone pair of the coordinating atoms (e.g. N, O, S, P) to the HOMO of the excited fluorophore. The presence of a coordinated guest lowers the energy of the lone pair involved in the coordination preventing the PET, thus causing the switch-ON of the fluorescence. Likewise, the protonation of these electron pairs prevents the PET effect from occurring by causing light emission.

The electron transfer process efficiency increases with the dielectric constant of the solvent thus generally PET mediated chemosensors are more fluorescent in apolar-low dielectric constant solvent (such as alkanes, dichloromethane or chloroform) than in polar-high dielectric constant environments (water, alcohols, DMSO, ACN, DMF). This indicates that solvation and microenvironmental physical parameters are crucial aspects to be considered in the studies.

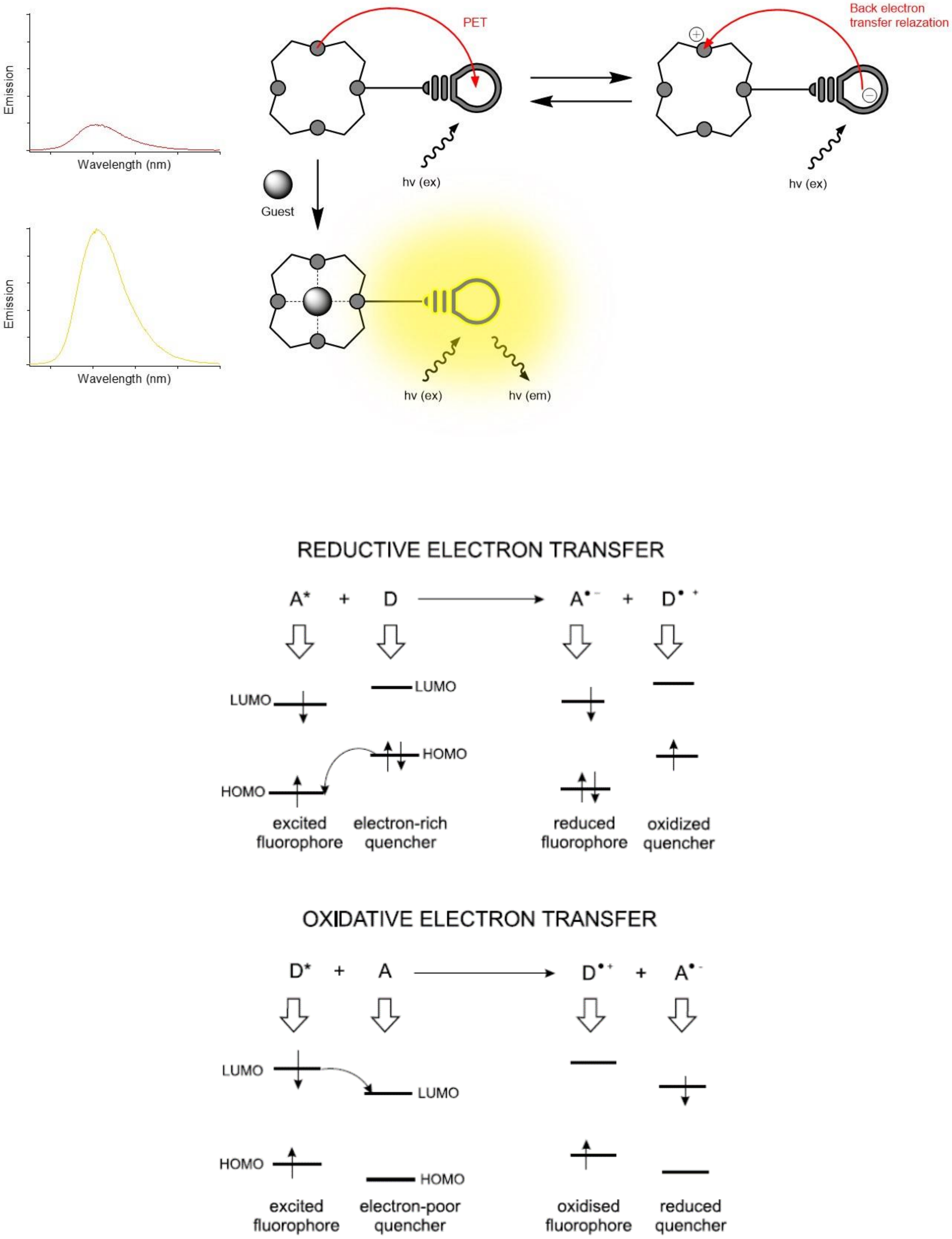

Figure 4. Photoinduced electron transfer (PET) mechanism.

Photoinduced Charge Transfer (PCT). This mechanism occurs when the host-guest interaction results in a re-distribution of the charge density in the fluorophore resulting in the displacement of the emission wavelength. In this kind of sensors, the receptor and the fluorophore units are integrated into the same structure, see Figure 5, and the fluorophore directly participate in the bond with the guest.

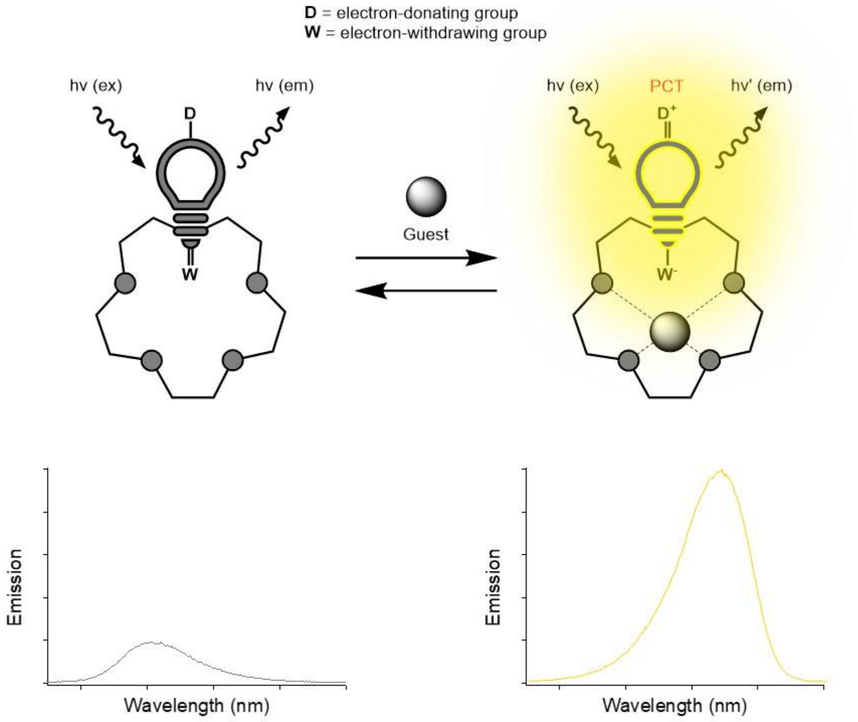

Figure 5. Photoinduced Charge Transfer (PCT) mechanism.

Fluorescence Resonance Energy Transfer (FRET). FRET (Figure 6) is a distance dependent interaction between the excited state of a fluorophore and a second fluorophore in which, during excitation, energy is transferred from a donor group to an acceptor moiety without photon emission. This means that by exciting a fluorophore at a determined wavelength, if FRET occurs, the emission of the second one is detected. Some conditions are essential for the occurrence of FRET: (i) the donor and the acceptor must be close enough to interact with each other (10-100 Å), (ii) the donor fluorescence emission wavelength must overlap the acceptor absorption wavelength for the energy transfer and (iii) donor and acceptor transition dipoles orientation must be approximately parallel. The presence of a guest forces the two fluorophores to move farther or closer to each other. In the first case, by exciting the free fluorophore A, the emission spectrum of the same is recorded as the FRET is prevented due to the distance between the two fluorophores. In the second case, instead, through coordination with the guest, a rearrangement occurs that causes the distance between the two fluorophores to decrease by switching-ON the FRET and thus recording the emission spectrum of B by exciting A.

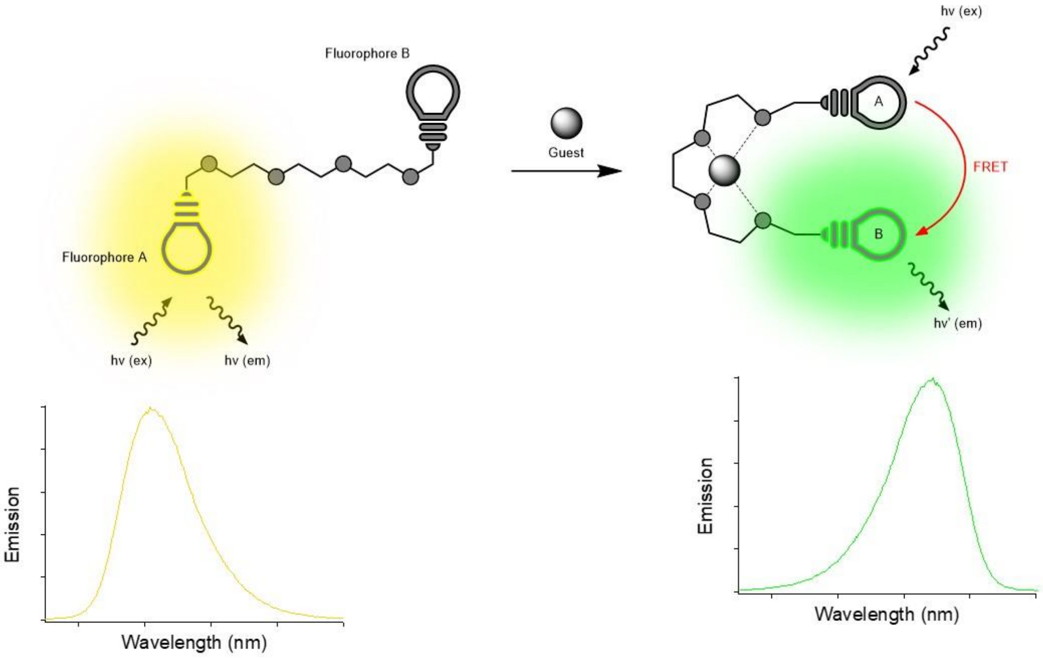

Figure 6. Fluorescence resonance energy transfer (FRET) mechanism.

Excimer or Exciplex Formation. Such new chemical species are formed in a sensor if the interaction between the excited components and those of the ground state is sufficiently strong, Figure 7. The process of formation of excimers and exciplexes is reversible and both entities can be luminescent.

The emission of an excimer or exciplex is always at lower energy compared with the monomer emission and usually the corresponding band is rather weak and broad. Similarly to the previous case, the presence of a guest strongly encourages or disrupts the formation of these species affecting the emission spectrum. It is also possible to obtain a quantitative measure of the content of an analyte from the ratio between the emission intensity of the monomer and of the excimer, conceptually these sensors are defined as “*ratiometric sensors*”.

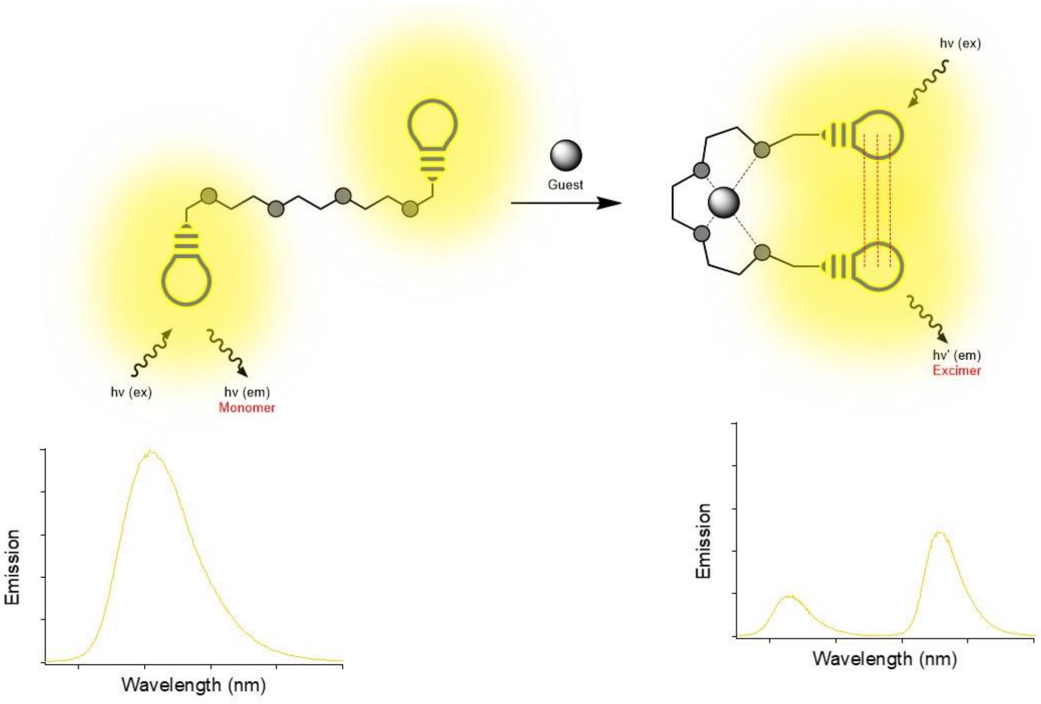

Figure 7. Excimer or Exciplex formation mechanism.

Irreversible reaction-based sensors: Chemodosimeters. The purpose of chemodosimeters is to obtain ligands that work in OFF-ON mode for the detection of those analytes (e.g. Cu^{2+}) that normally turn-OFF the fluorescence, see Figure 8. The conversion from non-emissive to emissive molecules is promoted by the guest via a non-reversible chemical reaction. They often require some specific conditions such as high temperature and organic solvents.

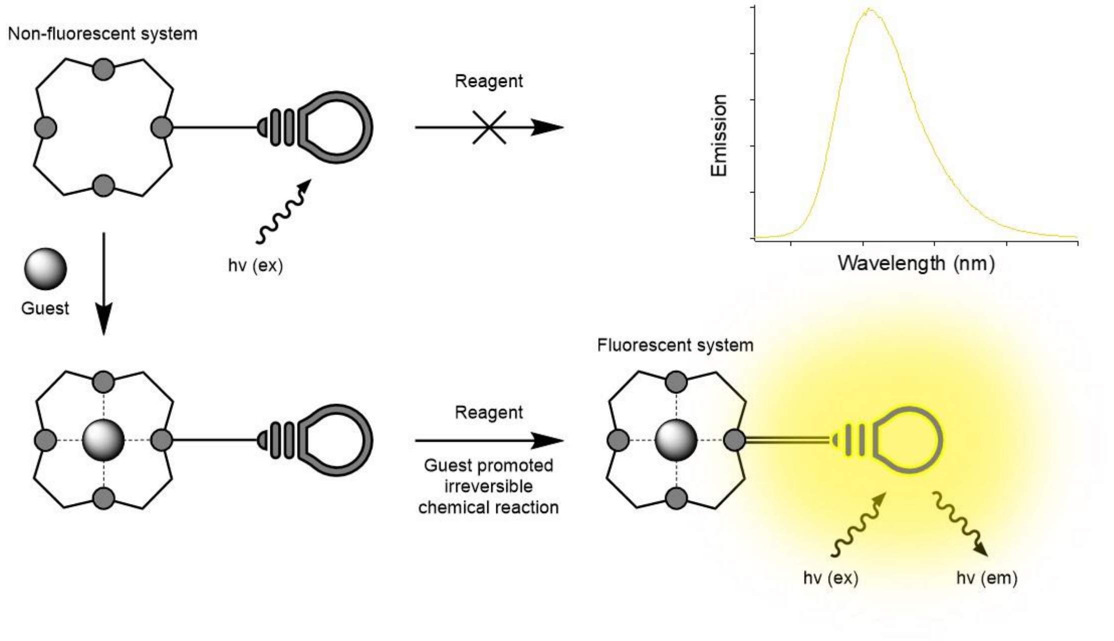

Figure 8. Irreversible reaction-based sensors.

Excited-State Intramolecular Proton Transfer (ESIPT). ESIPT is a four-level photochemistry process, reported in Figure 9, that involves an enol (E) to keto (K) transformation in the excited state through an intramolecular hydrogen bond, during which a proton is transferred from a hydroxyl or amino group to an electronegative atom, giving rise to a high Stokes shift. For this reason, the presence of an unsaturated H-bond acceptor, such as C=N or C=O, and a H-bond donor like NH or OH is essential. In the ground-state these systems are stable in their E forms. Upon the excitation (E^*), there is a redistribution of the electronic density causing an increase of both the acidity of the hydrogen bond donor and the basicity of the acceptor, giving rise to the K^* form that is the most stable form in the excited state. If the excited keto-form radiatively decays, a *reverse proton transfer (RPT)* takes place to give back the original E form, and this can be detected through a change in fluorescence emission along with a marked red-shift of the wavelength. This is attributed to the fact that in the ground-state the enol form is more stable than the keto form, while in the excited state the stability is inverted, resulting in a higher absorption energy gap between E and E* than between K* and K. ESIPT fluorophores can be often used as ratiometric sensors because of the dual-emission spectra arising from the emission bands of the enol (E^*) and keto (K^*) excited states.

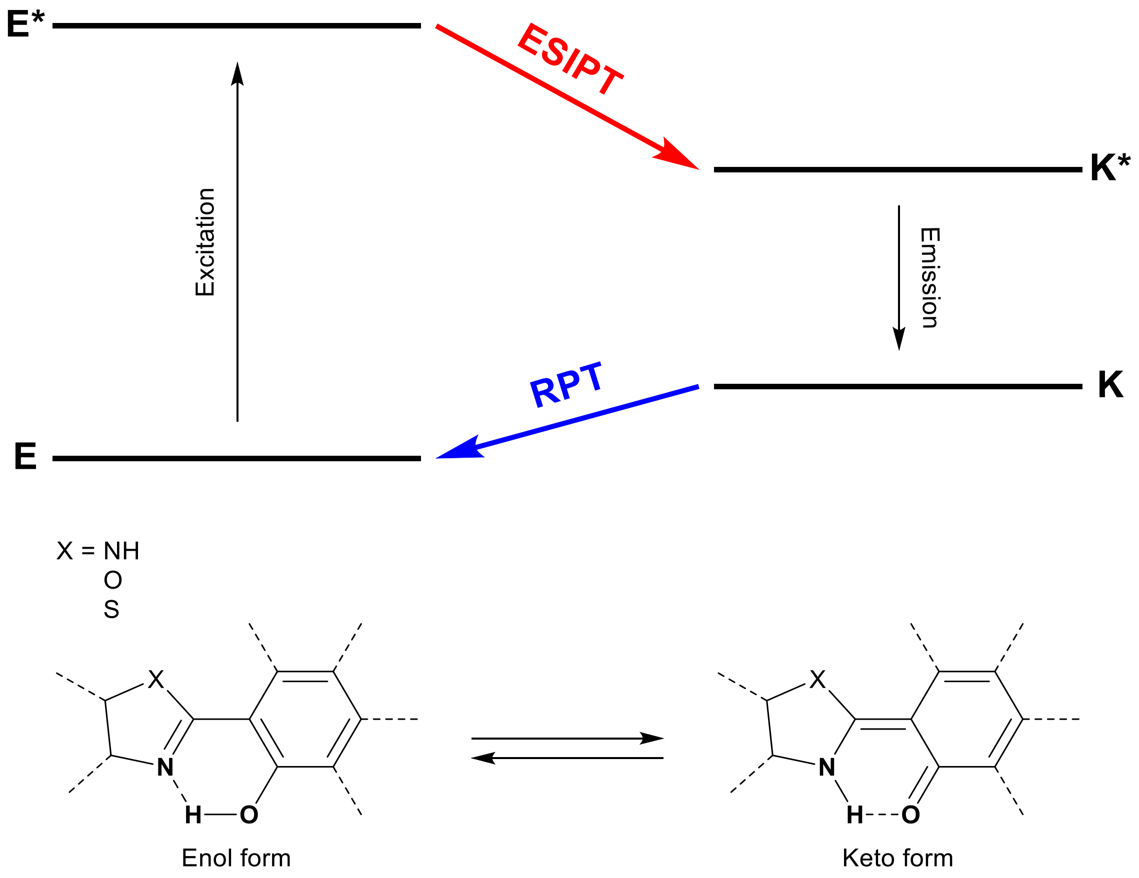

Figure 9. Excited-state intramolecular proton transfer (ESIPT) mechanism.

1.2.3 Fluorophores[7]

Dansyl. What makes Dansyl (DNS, Figure 10) an attractive fluorophore is its strong fluorescence, long emission wavelength (λ_{em} = 400-600 nm) and Stokes shift (λ_{exc} = 330-350 nm). As will be illustrated in the next chapters of this work, DNS is easy to insert inside ligands to make them fluorescent, this is possible by binding the S to an amine (obtaining an aminonaphthalenesulphonamide) or to a hydroxyl (obtaining an amino -naphthalenesulphonate). The polarity of the solvent affects the emission band and it shows a charge transfer character, caused by the mixing of the ^1L_a and ^1L_b states of naphthalene with a charge transfer state resulting from the promotion of a lone-pair electron on the amino group in an orbital of anti-bonding of the naphthalene ring. The deprotonation of sulphonamide hydrogen, induced by complexation with metal ions, usually quenches the fluorescence but it is also possible to appreciate an improvement and a blue-shift with metal ions capable of increasing the electronic density on the naphthenic ring, moving the state of charge transfer from amine to naphthalene towards higher energy. The DNS also has acid-base properties and the pH regulates its emission: protonating the dimethylamine group ($pKa \simeq 4$) prevents charge transfer and decreases the fluorescence while deprotonating the NH ($pKa \simeq 10$) increases the fluorescence compared to neutral fluorophore.

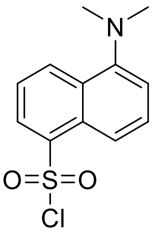

Figure 10. Dansyl chloride.

Coumarin. Coumarin and its derivatives (Figure 11) show a large Stokes shift, excellent quantum yields that prevent overlap between the excitation and emission spectra and a high dipole moment of the excited state. The photophysical parameters of these compounds can be modulated: both the wavelength of the fluorescence and the quantum yield of emission strongly depend on the nature and position of the substituent and also on the rigidity of the molecule. For instance, the absorption band of coumarin derivatives can be centred from 350 to 500 nm with emission spectra centred from 450 to 600 nm. Moreover, depending on the topology of the ligand, the coumarin carbonyl group can take part in the coordination. The analysis conducted in this thesis show how incorporating an electron-donor group in the 7-position (NH_2) and an electron-withdrawing group in 4-position (CF_3) the resulting coumarin derivatives show absorption bands in the visible region as a result of effective PCT induced by the electron push-pull system.

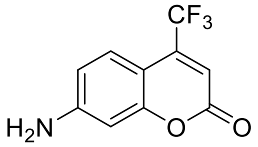

Figure 11. 7-Amino-4-(trifluoromethyl)coumarin.

Biphenol. The intensity of the biphenol (BPH, Figure 12) fluorescence emission strongly depends on the protonation state of the ligand, the most intense fluorescence is recorded in its monodeprotonated form and the least intense in the neutral one (more than six times lower), while the dianionic form, although fluorescent, it is obtainable only at very high pH values (pH > 15). By functionalizing the biphenol with amino functions, it is possible to form a network of H-bonds involving the BPH and the closest nitrogen atoms. In fact, as reported for the free BPH, the formation of an intramolecular H-bond that occurs between the two oxygen atoms of the BPH in stabilizing the hydrogen atom in the monoanionic species gives the maximum intensity of the fluorescence. On the contrary, the formation of intermolecular H-bonds with H-accepting molecules, such as water or amines (protonated and non-protonated), give rise to a very fast non-radiant process throughout the H-bond, thus leading to a change in the fluorescence (this occurs for example in the neutral form of excited BPH).[9] The fluorescence emission intensity of this kind of functionalized structures depends on at least three distinct factors: (i) the increase in electronic density on the phenolic oxygen atoms that enhances the fluorescence emission together with a red-shift of the emission wavelength through PCT mechanism; (ii) the increase in electronic density on the benzyl amine functions that quenches the emission intensity due to PET mechanism; (iii) the increase in the rotational freedom degree of the PH–PH bond that quenches the fluorescence via *TICT (Twisted Intramolecular Charge Transfer)* mechanism.[10]

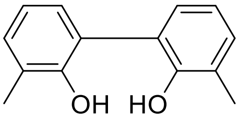

Figure 12. 3,3'-dimethyl-[1,1'-biphenyl]-2,2'-diol.

1.3 Non-Steroidal Anti-Inflammatory Drugs as Emerging Pollutants

Environmental water pollution is today a fundamental topic in the control and the safeguard of public health because water is of crucial importance for life sustainability. The problem is becoming more and more urgent due to the continuously increasing number of chemicals spread into the environment, which makes the bunch of compounds with potential ecological and toxicological risk enormous. Among the chemicals present in environmental water, *emerging pollutants (EPs)* are of particular interest because they are not routinely monitored. The Directive 2013/39/EU of European Union defines EPs as "*synthetic or naturally occurring chemicals or any microorganisms that are not commonly monitored in the environment but have the potential to enter the environment and cause known or suspected adverse ecological and/or human health effects*".[11,12] Many of them are used and released continuously into the environment even in very low quantities. The potential lethal impact on human and wildlife endocrine systems is already known for a certain number of EPs, even when they are present in trace quantities.[13] For instance they may cause chronic toxicity, endocrine disruption in humans and aquatic wildlife and the development of bacterial pathogen resistance.[14] EPs listed in European aquatic environments account about 700 compounds divided into 20 categories, the most representative being pharmaceuticals, personal care products, endocrine disrupting chemicals (EDCs), hormones and steroids, perfluorinated compounds (PFCs), surfactants, flame retardants, plasticizers, industrial and fuel additives, and antiseptics.[15]

To date, more than 600 chemicals of a pharmaceutical nature have been detected in the waters of 71 countries and among these, although in very low concentrations, the most frequent and ubiquitous are *non-steroidal anti-inflammatory drugs (NSAIDs)*.[16] Given the relatively low levels of detection, their negative effects on humans and the biosphere are related to their constant releases into the environment, leading to long-term high concentrations.[17] NSAIDs enter the environment mainly through industrial, municipal and hospital wastewater; this entry into the sewers demonstrates the lack of strict control over drug turnover, so that unused (defective and/or expired) drugs, including NSAIDs, enter without pre-treatment. The problem of these molecules – some of which are represented in Figure 13 – lies in their chemical structure and in their reactive groups: hydroxides and amides, which possess high reactivity, biological activity and stability which gives them resistance to biodegradation, ecotoxicity, persistence and consequently make them a threat to the environment and migration in the food chain.[16] At the metabolic level, NSAIDs are not completely metabolized and unused compounds are excreted unchanged or in complexes with glucuronic acid.

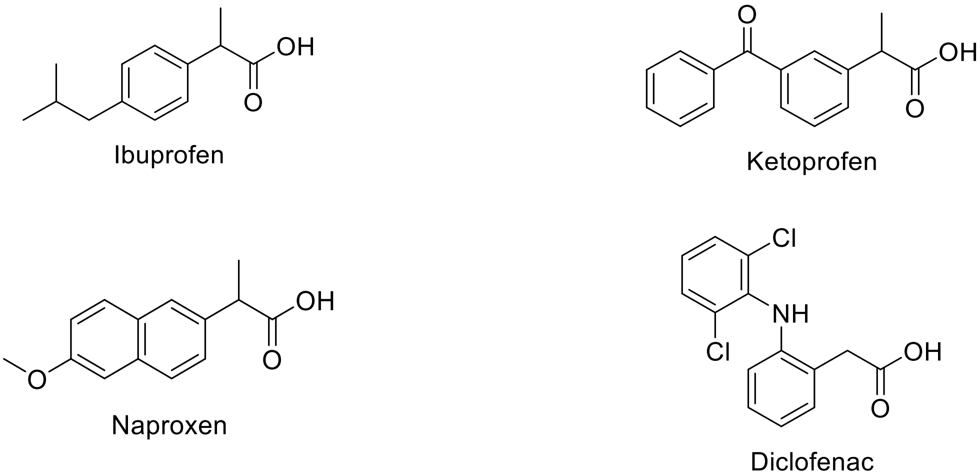

Ibuprofen

Ketoprofen

Naproxen

Diclofenac

Figure 13. Structures of the NSAIDs studied in this project.

Among the disorders caused by NSAIDs[16] in the organs of living organisms, the most common is induced oxidative stress, which involves changes in the activity of antioxidant enzymes, in the total number of proteins and in lipid peroxidation. Disturbances in the body’s self-purification system are also important: cytological changes of kidneys and liver in fish exposed to DCL are known, as well as cardiovascular defects and cardiac anomalies have been found in freshwater fish in the presence of DCL, that is the most resistant NSAID to biological transformation.[18] Moreover, other issues are linked to metabolic disturbances ranging from changes in the activity of detoxifying enzymes to mitochondrial dysfunction and decreased functional stability of membranes. Further and worrying consequences of the accumulation of NSAIDs include: the modification of the content of chlorophyll, anthocyanins and carotenoids in higher plants and algae, the inhibition of the growth of river biofilms and the impediment of the normal physiological activity of microorganisms responsible for ecological processes in the biosphere such as the carbon and nitrogen cycles. Together with DLC, NPX[19], KET[20] and IBU are continuously monitored and different strategies for their removal have been proposed, such as bacterial degradation, photodegradation or absorption on zeolites.[19] They present carboxylic acid moiety that can be easily deprotonated. Indeed, they are mostly commercialized in their anionic form as sodium or lysine salts. NPX is often considered the first-line treatment for a wide variety of disorders that require anesthetic clinical treatment, and nowadays high levels of this drug are found in the environment, in particular in water.[17] The effect of NPX on living organisms and its biodegradation have not been fully studied yet, but there is some evidence that this drug and its biotransformation products can be mutagenic and teratogenic, and can have adverse effects on the fertility and reproduction of aquatic animals and plants.[19] KET is less toxic. Indeed, studies demonstrated that exposure to KET caused biochemical alterations in freshwater species, such as macrophyte and microcrustacean species, but these alterations did not cause deleterious effects on their physiological and populational traits.[21] IBU, on the other hand, is the most commonly prescribed NSAID as an analgesic, antipyretic and anti-inflammatory agent in conditions like osteoarthritis, rheumatoid arthritis, juvenile idiopathic arthritis, and acutely painful musculoskeletal conditions. The adverse effects associated with IBU[22] stem from prostaglandins' important roles, and thromboxanes play in various organ systems, including maintaining gastric mucosal integrity and renal blood flow. IBU can, therefore, cause dyspeptic symptoms and gastrointestinal ulcers. In the kidneys, this can lead to decreased renal perfusion in the afferent renal vessels, especially in the individuals with preexisting dehydration or renal impairment, thereby leading to reduced glomerular filtration rate.

There have been reports of metabolic acidosis after an acute overdose of ibuprofen and other NSAIDs, which may be explained by the accumulation of acidic metabolites in the blood.

These chemicals are currently determined by off-site analysis that requires collection, transportation, eventual pre-treating of the sample, expensive instrumentations and specifically trained staff. Thus, providing devices able to allow a rapid on-site detection of target analytes would have a dramatic impact in the environmental control with significant economic benefits.[23] The development of chemical sensors has been conceived to bypass the restrictions related to the classical analytical protocols and the use of conventional laboratory techniques for environmental control. While the technological foundation for chemical sensors already exists, their application to emerging pollutants detection is complicated by the difficulty in the design of selective ligands due to the large number and the diversity of listed EPs.[24] Ideally, a ligand able to bind NSAIDs in their anionic forms should include strong hydrogen bond (HB) donors to interact with the carboxylate moiety and an aromatic portion able to interact with the aromatic rings of the drugs via hydrophobic or π-stacking interactions.[25]

1.4 Squaramides

1.4.1 A general overview

Squaramides (3,4-diamino-3-cyclobuten-1,2-dione) are conformationally rigid and stable cyclobutene ring derivatives from squaric acid composed of two carbonyl hydrogen bond acceptors in proximity to two NHs hydrogen bond donors. These compounds, with interesting chemical and physical properties,[26] possess the ability to form strong hydrogen bonds, directionally converging or bidirectionals (see Figure 14), responsible for increasing the aromatic character of the four membered aromatic unit. This fact is highly advantageous in all processes of self-assembly and molecular recognition in which ones benefit from a thermodynamically favourable stability determined by the aromatic gain.[27] Recent studies indeed established that the increase in aromaticity upon HB formation represents the main driving force to bind anions forming stable complexes and justifies the extensive use of the squaramide scaffold in the design of ligands and chemosensors.[28,29,30]

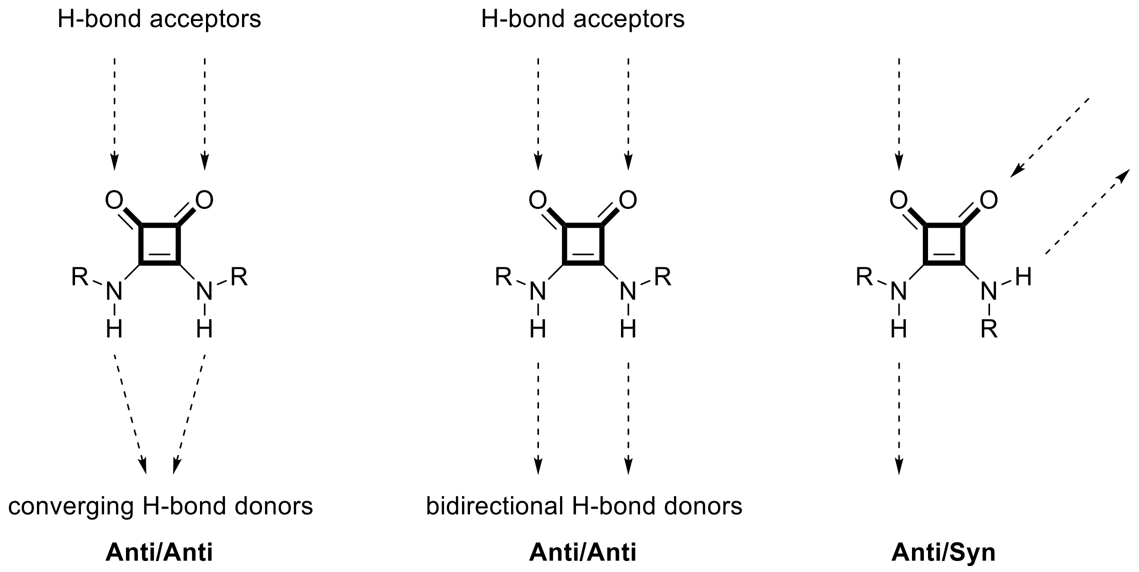

Figure 14. Representations of the *anti/anti*- and *anti/syn*-conformations of bis-secondary squaramides.

The C–N bonds of squaramide compounds (similarly to amide structures) exhibit a partially limited rotation around the C–N bond, thus giving rise to *syn*- and *anti*-conformations. It exists an energy barrier of approximately 63 kJ·mol^{-1} between the *syn*- and *anti*-modes of the various squaramide structures, allowing for prompt interconversion between the two conformers at room temperature. NMR evidences support the existence of *sin/anti*- and *anti/anti*-conformation mixtures, nevertheless the *syn/syn*-conformation was not observed as the result of a high energy barrier determined by a significant steric hindrance.[31]

A crystallographic study of a cyclic squaramide found that macrocycles containing squaramides show a preference for *trans-trans* conformers in their crystalline forms.[32] Moreover, the same squaramide was found to assemble in the solid state in a “head-to-tail” hydrogen bonding assembly where only one of the squaramide carbonyls participates in hydrogen bonding with a neighbouring NH and the second carbonyl exhibits just a close contact with an aromatic hydrogen. This behaviour is rare for *trans-trans* squaramides, for which the usual arrangement is with both amide protons bonding to both carbonyls in a ribbon-type structure. The DMSO solvate of this compound (analogy to the single-arm ligand **L7** present in this experimental work) exactly matched the reported crystal structure in Figure 15: the macrocycle displayed a *trans-trans* squaramide conformation with each of the NH groups hydrogen bonded to the DMSO oxygen.[33]

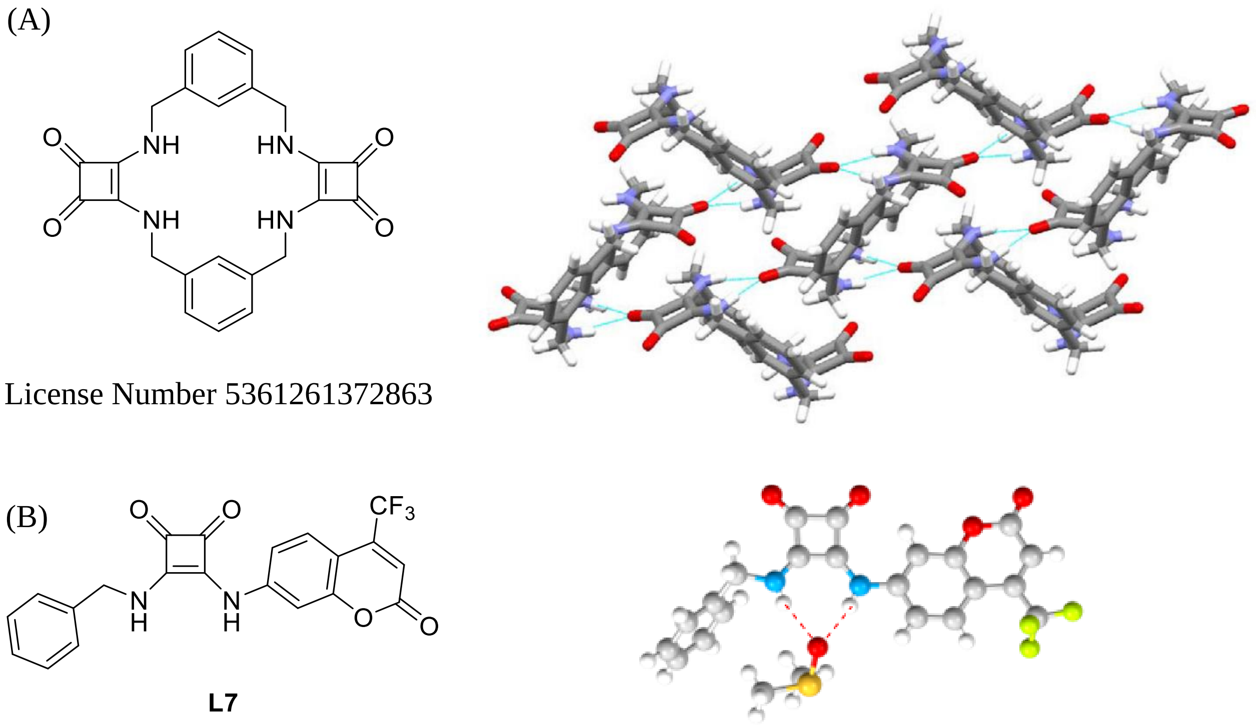

License Number 5361261372863

L7

Figure 15. (A) X-ray crystal structure of squaramide macrocycle exhibiting the *trans-trans* conformation and demonstrating "head-to-tail" hydrogen bonding assembly; (B) X-ray crystal structure of single-arm squaramide ligand **L7** coordinated with DMSO.

On a synthetic level, by intervening on the reaction temperature and the solvent (and with the possible use of catalysts such as, for example, Sc^{3+} and Zn^{2+} triflates – see Figure 16)[34] it is possible to selectively obtain a symmetrical double attachment or a single bond with a specific nucleophile from the starting squaric ester. This latter situation is known as *sequential substitution* and is a particularly useful feature as the higher aromatic stabilization provided by the first substitution reaction, with respect to the parent squarate, makes the monosubstituted intermediate less reactive, thus allowing easy synthetic access to the asymmetric squaramides.[35]

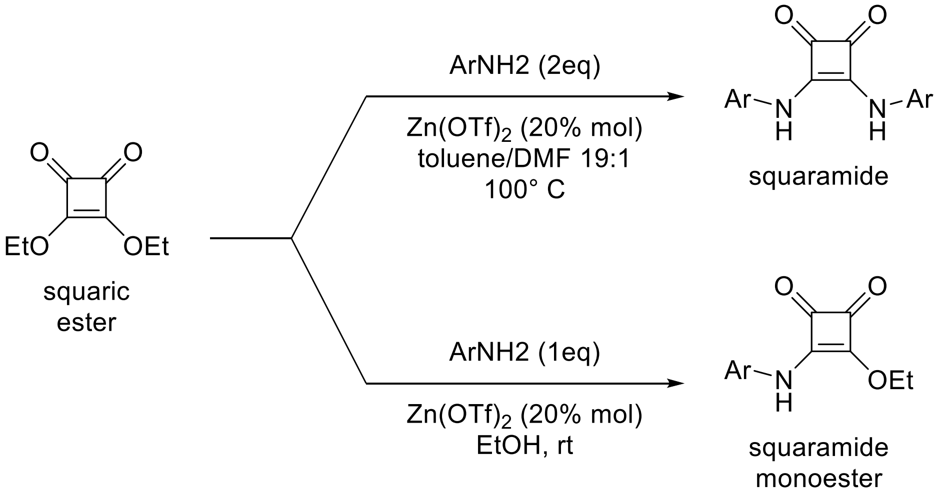

Figure 16. Preparation of symmetrically and unsymmetrically substituted N,N'-diarylsquaramides by Zn(OTf)$_2$-catalyzed condensation.

1.4.2 Squaramides as anion recognition motifs

The applications of squaramide derivatives range across a wide variety of chemistry fields from medicinal chemistry to biochemistry, from material science to organometallic chemistry, from organocatalysis to molecular recognition.[27(a)] The field of anion recognition, in particular, has developed considerably in recent years and a large collection of research has now been reported in the areas of anion receptors, anion sensors, and, more recently, anion transporters. Numerous binding motifs dedicated to hydrogen bonding have been exploited for the recognition of anions and it was inevitable that squaramides, with their several advantageous characteristics, were also explored as anionic recognition motifs, evolving from anionic receptors to sensors and even as highly effective anion carriers.

The two secondary enamine NH groups of squaramide ring can be considered as vinylogue analogous of amides and possess strong HB donor capability towards anionic species. Specifically, squaramide-based ligands designed to bind carboxylate anions were successfully developed, working as effective anion receptors even in highly competitive medium such as water or DMSO, due to two principal factors: (i) the two NH groups can cooperate in binding the COO^- functions and (ii) when squaramide is involved in H-bonding the cyclobutene ring gains an additional aromatic character[26,27(a)] that increase their effectiveness during the anionic complexation. The binding of squaramides to anionic species is influenced by the acidity of the NH protons (which can be enhanced by using solvents such as DMSO) and the overall receptor structure. The presence of electron withdrawing groups, in fact, is responsible for the increase in the acidity of the NH groups, increasing their hydrogen bond donation capacity, the proton-transfer processes and favouring in this way the formation of complexes.

In addition, the coupling of more than one squaramide moieties in a macrocyclic framework reinforces the anion binding properties of the ligand, allowing to bind inorganic oxa-anions in water with selectivity depending on the pH.[36,37] As regards, however, the peculiarity of the deactivated squaramides containing aromatic molecules, as hydrogen bond donors, depends as well on the contribution of the aromatic CH bonds in the interaction since it has been proven that the cooperation of CH groups, belonging to electron deficient aromatic substituents on the receptor, is quite common in the formation of receptor-anion adducts.[38]

1.5 Pyridinophane polyamine

Ligands containing polyamine chains are characterized by high water solubility and ability to coordinate metal ions, anions and neutral molecules according to their degree of protonation. Their applications are manifold, especially where an aqueous media is needed: biological studies, water analysis, soil contamination, etc. They are often associated with fluorescent signalling units that allow an immediate visual response to the adduct formation, most commonly through a PET driven signal transduction.[39]

It is possible to summarize these ligands in three categories depending on the polyamine topology, as reported in Figure 17: *open chain*, *branched* and *macrocyclic* (receptors with greater preorganization). In the latter case, the cyclic structure allows the formation of polyammonium receptors in aqueous solution, under specific pH conditions, with a high positive charge density that are sufficiently flexible to coordinate anions and stabilize them through electrostatic interactions and/or H-bonds.[40] The addition of functional groups, such as squaramides, can increase their ability to bind anionic species.

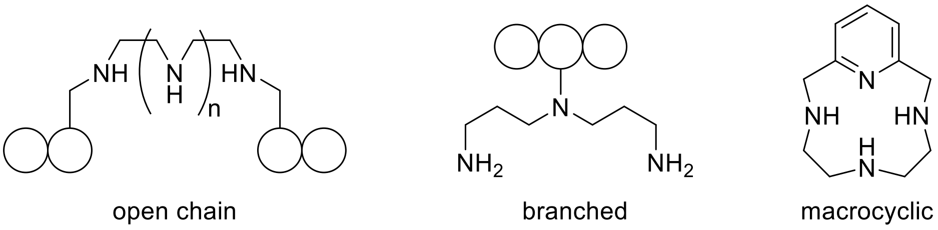

open chain branched macrocyclic

Figure 17. Representation of polyamine ligands by category.

The polyazamacrocycle reported in this thesis was synthesized by modifying the Richman-Atkins procedure (see Figure 18),[41] attaching two arms of the full-tosylated polyamine N,N,N-tris(2-aminoethyl)amine with 2,6-bis(bromomethyl)pyridine in 1:1 molar ratio using K_2CO_3 as a base in refluxing ACN. The compound is characterized by the formation of H-bonds between the amino group of the tail and those of the macrocycle, making the protonation sequence unclear. Furthermore, it is not possible to measure the fourth protonation constant that ought to involve the central tertiary amino nitrogen of the macrocyclic ring, which should have a very low value since it will involve electrostatic repulsion with charged polyammonium groups each separated by an ethylene chain, at the same time as the solvation effects of the water which make it less basic in this solution.[42]

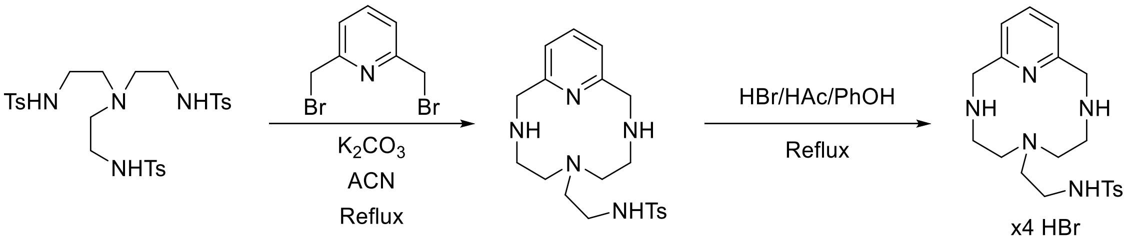

Figure 18. Synthesis of the polyazamacrocycle moiety.

The sensors carrying this molecular moiety are called “azascorpiand-like ligands” and consist of a fixed macrocyclic nucleus with a pendant arm containing groups of additional donors that play an active role in coordination within the cavity. The molecular movements of the flexible arm and the reorganization with respect to the macrocyclic nucleus, in extended and closed conformations, are guided by the pH of the solution (based on the minimization of electrostatic repulsion and the formation of H-bonds) and the presence of metal ions. The metal free macrocycle can interact through H-bonds and, when protonated, through charge-charge interactions with the anions; in the case of the metal complex, on the other hand, there is the possibility of providing coordinative bonds by the metal site itself.[43] The structure of the polyazamacrocycle was studied for the $[CuL]^{2+}$ complex, Figure 19. The coordination geometry of Cu^{2+} is slightly distorted square pyramidal, with the primary nitrogen atom in the tail occupying one of the equatorial positions; the remaining positions in the base of the pyramids are formed by the two secondary amino groups of the macrocyclic cores and by pyridine nitrogen, which has the shortest distance from the metal. The slightly elongated axial position is occupied by the tertiary amino group.[42]

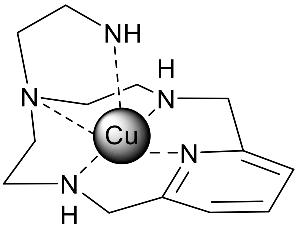

Figure 19. Structure of the polyazamacrocycle as $[CuL]^{2+}$ complex.

Chapter 2 – Discussion

2.1 Results and Discussion of L1, L2, L3, L4 and L5

2.1.1 Synthesis

The synthetic strategy adopted to obtain ligands **L1**-**L4** is outlined in Scheme 5, whereas the synthesis of macrocycle **L5** is reported in Scheme 6.

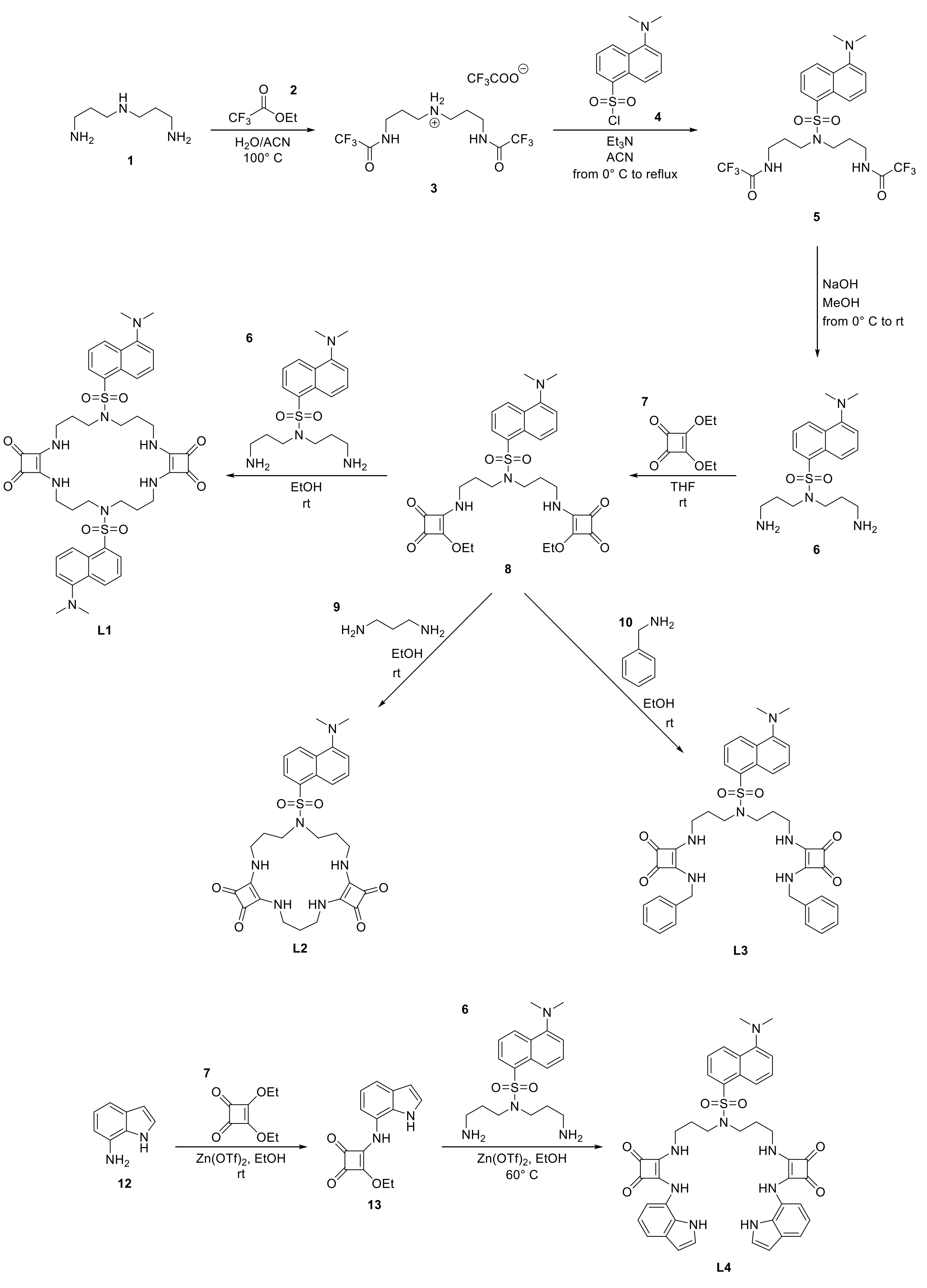

Scheme 5. Synthesis pathway to obtain ligands **L1**-**L4**.

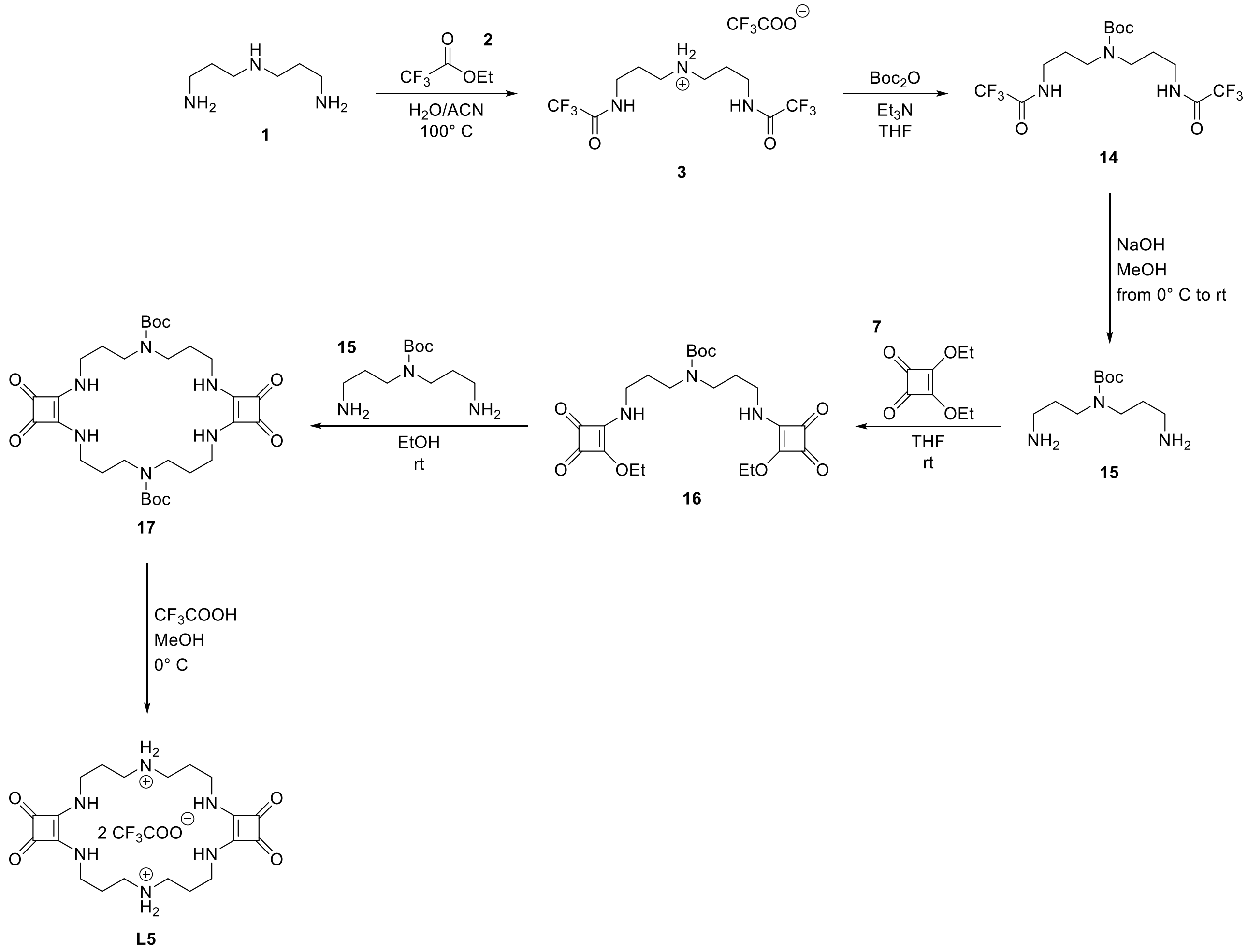

Scheme 6. Synthesis pathway to obtain ligand **L5**.

The key intermediate **6** was synthesized starting from dansyl chloride **4** and N,N-bis(3-trifluoroacetylaminopropyl)ammonium trifluoroacetate **3**, synthesized as reported in literature,[44] and subsequent de-acetylation of the primary amine functions under basic methanolic conditions. The intermediate **6** was converted into its bis-ethoxysquaramide derivative **8** by following a coupling reaction with two equivalents of diethylsquarate **7**. The macrocyclic systems **L1** and **L2** were obtained in good yields by a modified high-dilution Richman-Atkins cyclization[41(a)] using **8** as electrophilic difunctional intermediate and diamines **6** or **9**, respectively, as nucleophilic reagents. The open chain ligand **L3** was obtained by direct coupling of the intermediate **8** with two equivalents of benzylamine **10** in ethanol at room temperature. Due to the lower reactivity of aromatic amines, the ligand **L4** was obtained in two steps: first by coupling the diethylsquarate **7** with the 7-aminoindole **12** in the presence of a catalytical amount of zinc triflate, and then by reacting the intermediate **13** with **6**, in hot ethanol in the presence of zinc triflate, to obtain the desired product. All ligands precipitated from the reaction mixture. **L1**-**L3** were purified in acceptable yields by crystallization from hot concentrated DMF solutions. The synthetic strategy to obtain **L5** is comparable to that to obtain **L1**, with the difference that the formation of the trifluoroacetate salt is exploited for the protection, through the use of Boc, of the central secondary amine. In the final step the system is deprotected with trifluoroacetic acid at 0° C obtaining **L5** as a trifluoroacetate salt, which has greater solubility than other salts such as, for example, sulphates.

2.1.2 ^{1}H-NMR studies

Preliminary host-guest interaction studies were conducted on **L1**-**L4** by means of ^{1}H-NMR titrations using DMSO-d_6/0.5% water as a solvent mixture and the guests as their sodium salts. All the ligands interacted with the guests considered under these experimental conditions. The scarce solubility of **L1**-**L4** prevented to conduct ^{1}H-NMR studies in other solvents such as CD_3CN-d_3. There are no titrations with **L5** as it is poorly coordinated and above all because it will be substantially used to explain the basic absorption and fluorescence of the ligands **L1**-**L4** given by the squaramide macrocycle.

As shown by the stack-plots in Figures 20-25, in the case of **L1**-**L3**, the addition of increasing amounts of BzO$^-$ and KET$^-$ caused the broadening of the signals attributed to the squaramide NHs, and their overlapping with signals of the guests in the aromatic region. For these reasons, the calculation of reliable association constants was not possible. In the case of NPX$^-$ it was not possible to conduct titration experiments due to solubility issues.

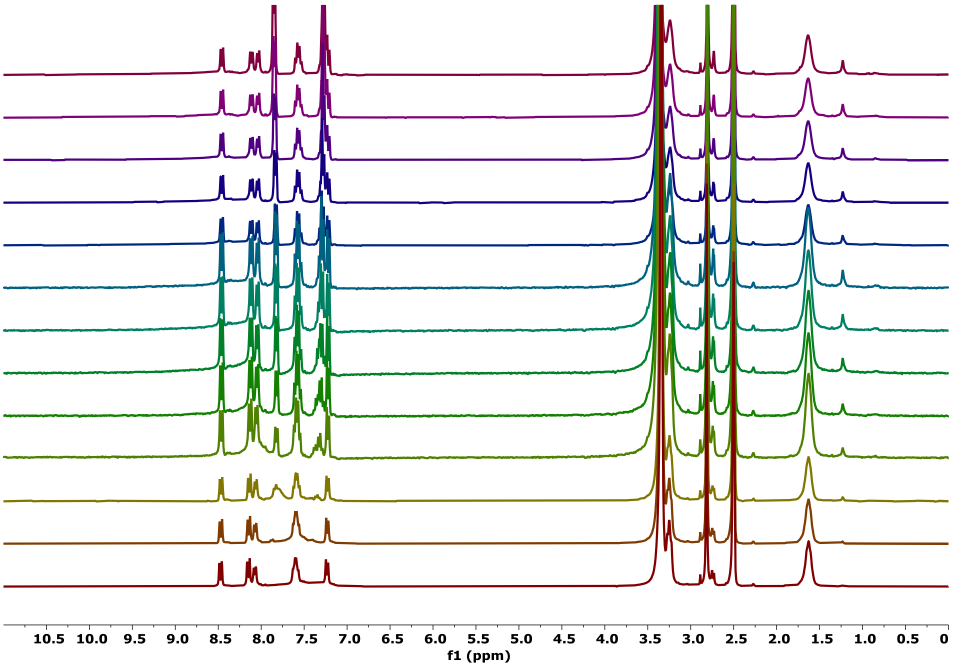

Figure 20. Stack plot of the ^{1}H-NMR titration of **L1** ($5.0\mathrm{x}10^{-3}$ M) in DMSO-d_6/0.5% water at 298 K in the presence of increasing molar ratios of NaBzO (0.075 M).

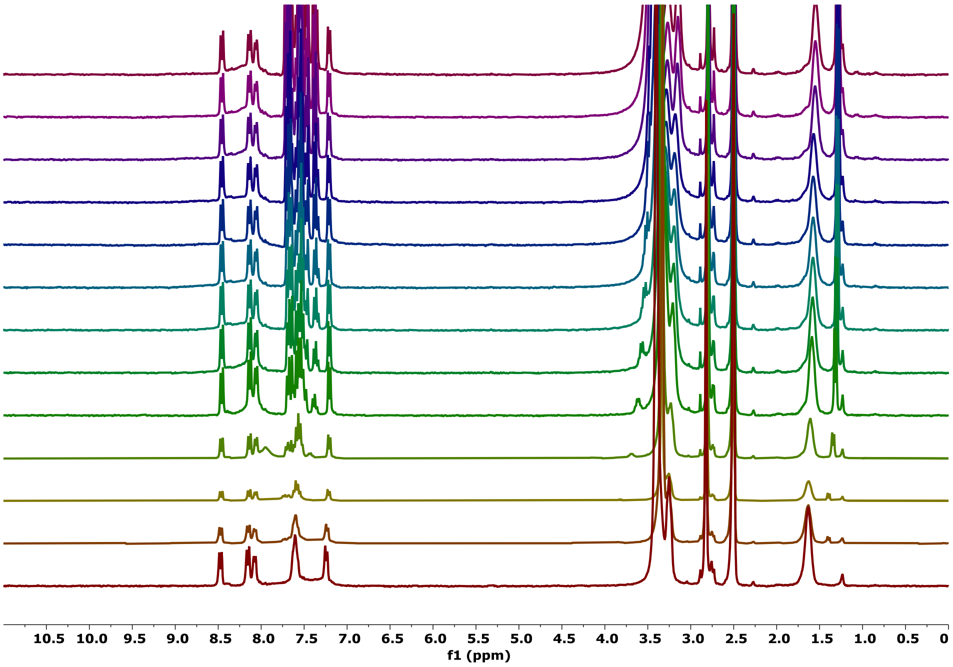

Figure 21. Stack plot of the ^{1}H-NMR titration of **L1** ($5.0\mathrm{x}10^{-3}$ M) in DMSO-d_6/0.5% water at 298 K in the presence of increasing molar ratios of NaKET (0.075 M).

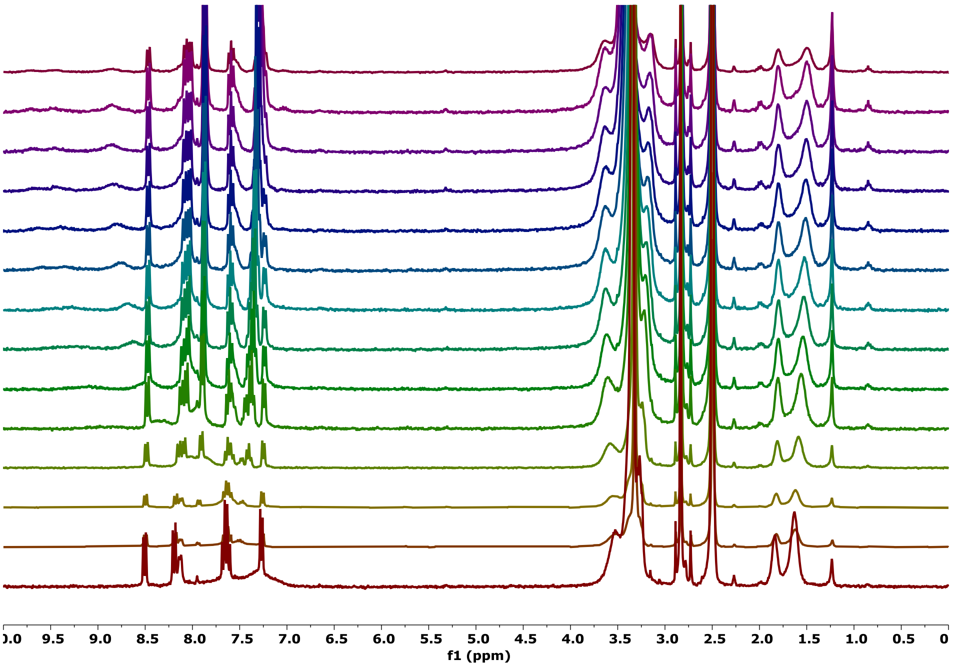

Figure 22. Stack plot of the ^{1}H-NMR titration of **L2** ($5.0x10^{-3}$ M) in DMSO-d_6/0.5% water at 298 K in the presence of increasing molar ratios of NaBzO (0.075 M).

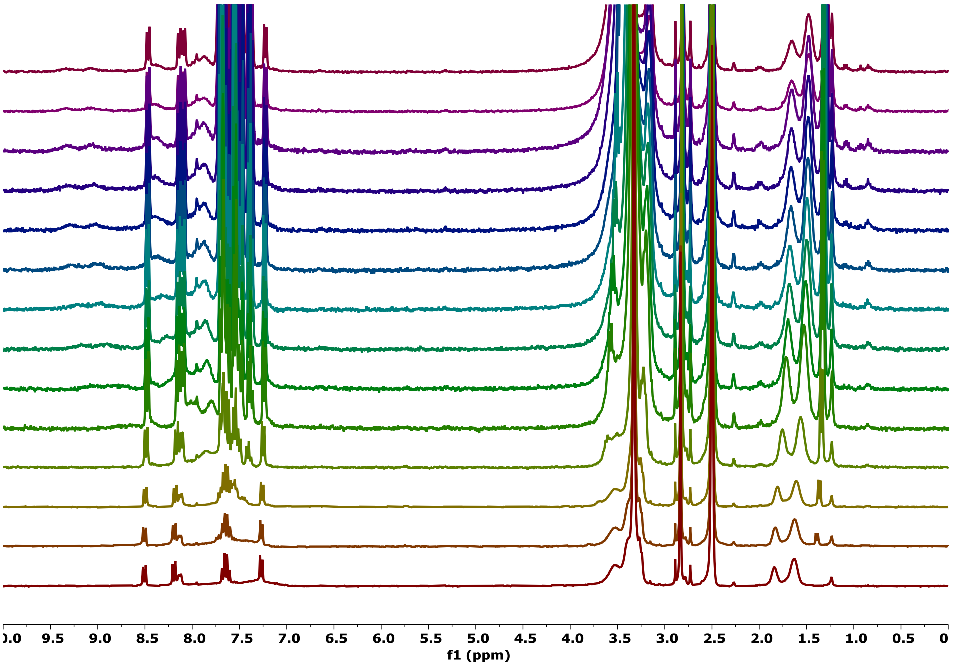

Figure 23. Stack plot of the ^{1}H-NMR titration of **L2** ($5.0x10^{-3}$ M) in DMSO-d_6/0.5% water at 298 K in the presence of increasing molar ratios of NaKET (0.075 M).

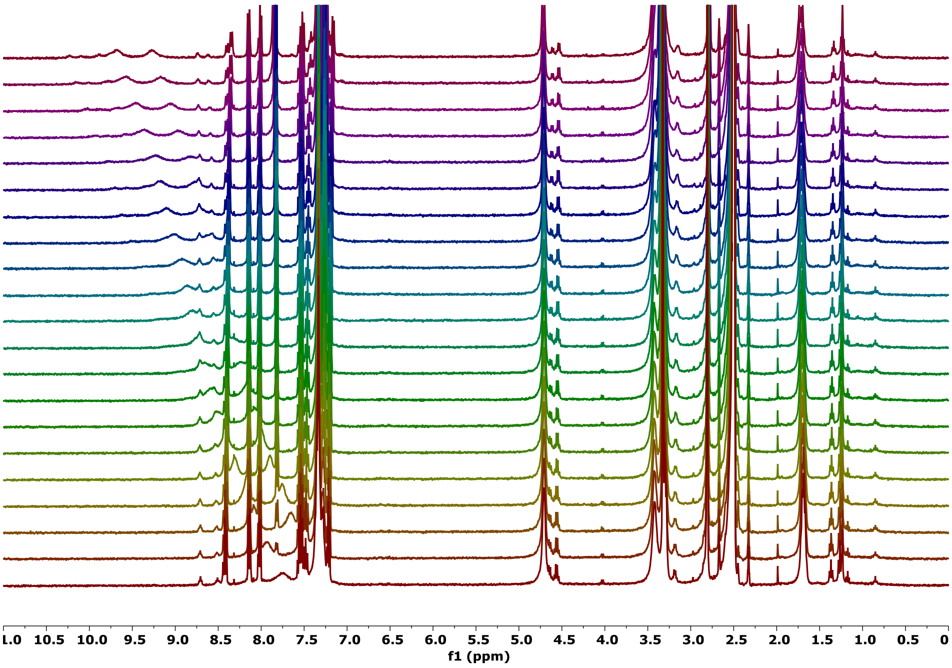

Figure 24. Stack plot of the ^{1}H-NMR titration of **L3** ($5.0x10^{-3}$ M) in DMSO-d_6/0.5% water at 298 K in the presence of increasing molar ratios of NaBzO (0.075 M).

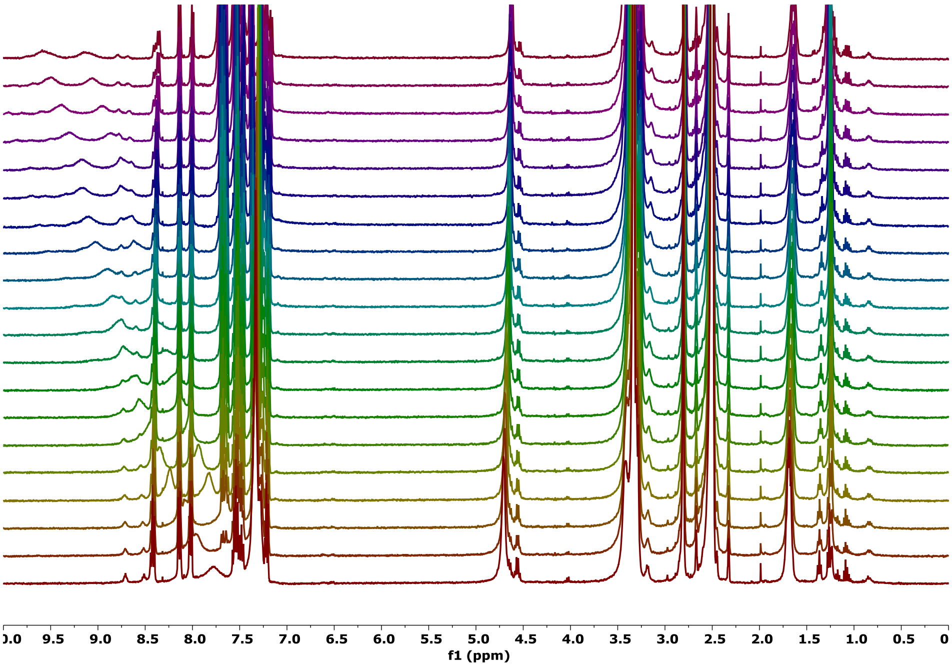

Figure 25. Stack plot of the ^{1}H-NMR titration of **L3** ($5.0x10^{-3}$ M) in DMSO-d_6/0.5% water at 298 K in the presence of increasing molar ratios of NaKET (0.075 M).

Interestingly, in the case of **L4** we were able to clearly follow the downfield shift of the signal attributed to the indole NHs upon the addition of increasing amounts of BzO⁻, NPX⁻ and KET⁻, added as their sodium salts. Figure 26-28 shows the stack plot of the titration of **L4** in the presence of NPX⁻, KET⁻ and BzO⁻ respectively.

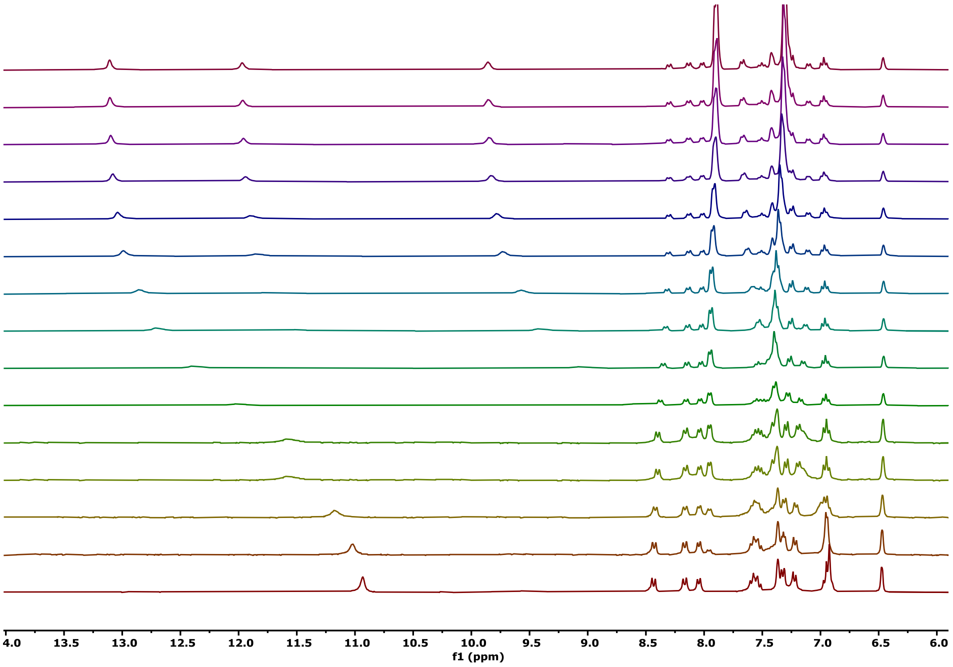

Figure 26. Stack plot of the ^{1}H-NMR titration of **L4** (5.1×10^{-3} M) in DMSO-d_6/0.5% water at 298 K in the presence of increasing molar ratios of NaBzO (0.083 M).

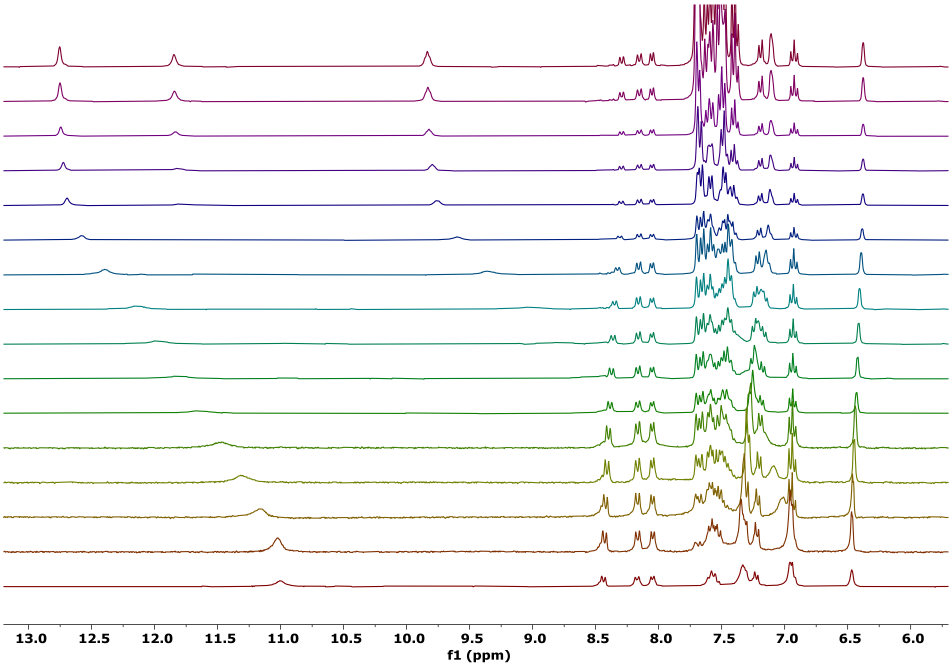

Figure 27. Stack plot of the ^{1}H-NMR titration of **L4** (5.1×10^{-3} M) in DMSO-d_6/0.5% water at 298 K in the presence of increasing molar ratios of NaKET (0.076 M).

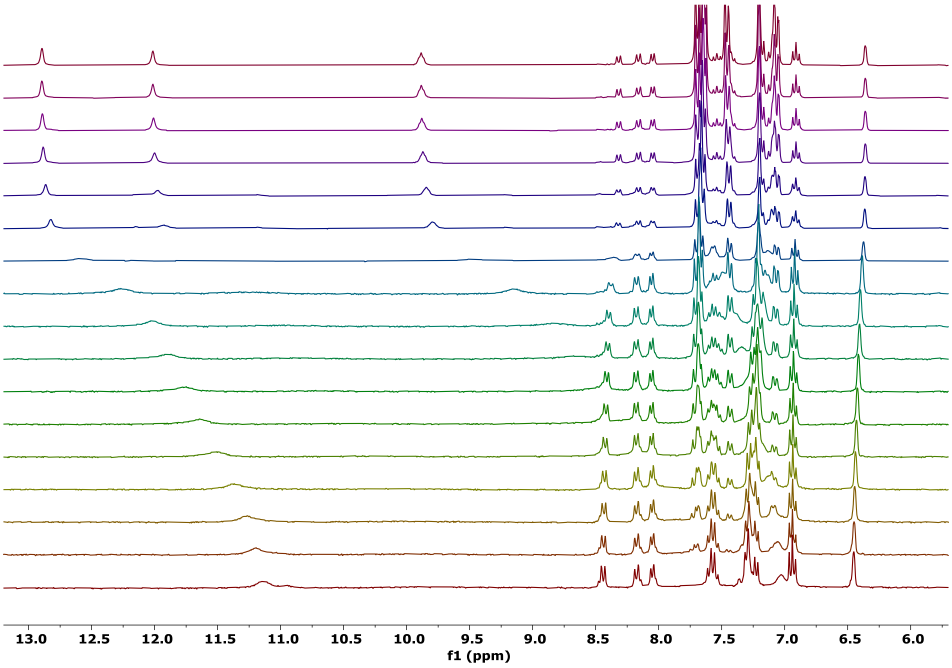

Figure 28. Stack plot of the ^{1}H-NMR titration of **L4** (5.0×10^{-3} M) in DMSO-d_6/0.5% water at 298 K in the presence of increasing molar ratios of NaNPX (0.075 M).

In all cases, upon the addition of about 0.3 equivalents of the anion, a downfield shift of the signal attributed to the indole NH (11.0 ppm) was observed.

During the titrations we were also able to observe the appearance of the two signals at 9.5 ppm and 11.5 ppm attributed to the squaramide NHs. Although it was not possible to follow their chemical shift throughout the titration, we can assess that they are involved in the formation of HB interactions with the target guests.

2.1.3 Photophysical characterization

Preliminary spectrophotometric and spectrofluorimetric studies were conducted on **L1**-**L5** in DMSO. In these conditions just small changes in the absorption and the emission spectra were observed upon the addition of increasing amounts of NPX^{-} and KET^{-}. In order to enhance the optical response of the probes, we decided to conduct the measurements in a less competitive medium, i.e. CH_3CN/DMSO solution (9:1 v/v) The absorption spectrum in CH_3CN/DMSO solution (9:1 v/v) of **L5** containing two squaramides units shows an intense band ($\varepsilon = 51000$ $M^{-1}\cdot cm^{-1}$) centred at 285 nm. In the case of **L1**, **L2** and **L3**, a shoulder is present in the 310-340 nm region, where the dansyl chromophore absorbs (the dansylamide showing a maximum at 330 nm with a $\varepsilon = 3800$ $M^{-1}\cdot cm^{-1}$). As expected, the spectra of these hosts are very similar to the sum of the absorption spectra of **L5** and one (**L2** and **L3**) or two (**L1**) dansyl units. In the absorption spectrum of **L4**, the band of the squaramide is strongly perturbed by the nearby indole unit, with the maximum being red-shifted to 335 nm – as supported by the theoretical calculations reported below – in coincidence with the maximum of the dansyl unit; the total absorption coefficient at this wavelength is $\varepsilon = 30500$ $M^{-1}\cdot cm^{-1}$ (Figure 29).

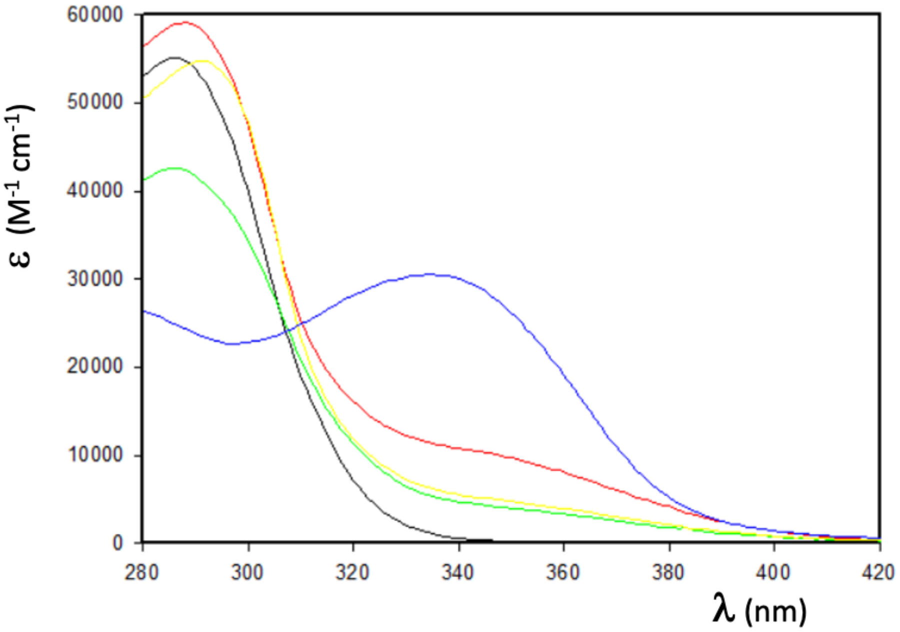

Figure 29. Absorption spectra in CH_3CN/DMSO solution (9:1 v/v) of the hosts **L1** (red), **L2** (green), **L3** (yellow), **L4** (blue) and **L5** (black).

As far as the emission spectra are concerned, at room temperature in CH_3CN/DMSO solution (9:1 v/v) **L5** does not show any fluorescence, while **L1** (Φ = 0.77; t = 13,2 ns), **L2** (Φ = 0.77; τ = 12,6 ns), **L3** (Φ = 0.75; τ = 13,7 ns), and **L4** (Φ = 0.095; τ = 11,3 ns), as shown in Figure 30, display the typical fluorescence band at 525 nm of the dansyl chromophore under the same experimental conditions, as it can be observed for the dansylamide (λ_{max} = 510 nm, Φ = 0.88; τ = 12.9 ns). In all cases when at least a dansyl unit is present, the shape of the corrected excitation spectrum is similar to that of the absorption spectrum of the dansylamide. On the contrary, the contribution attributable to the squaramides is almost completely absent, indicating that the energy transfer from these units to the dansyl moiety does not occur. The absence of energy transfer between the chromophoric units present in the host can also explain the lower quantum yield observed for **L4**, since in this case the contribution of the dansyl unit to the absorption at 330 nm (the excitation at which the quantum yield has been measured) can be estimated to be only 12%, the 88% being absorbed by the indole units.

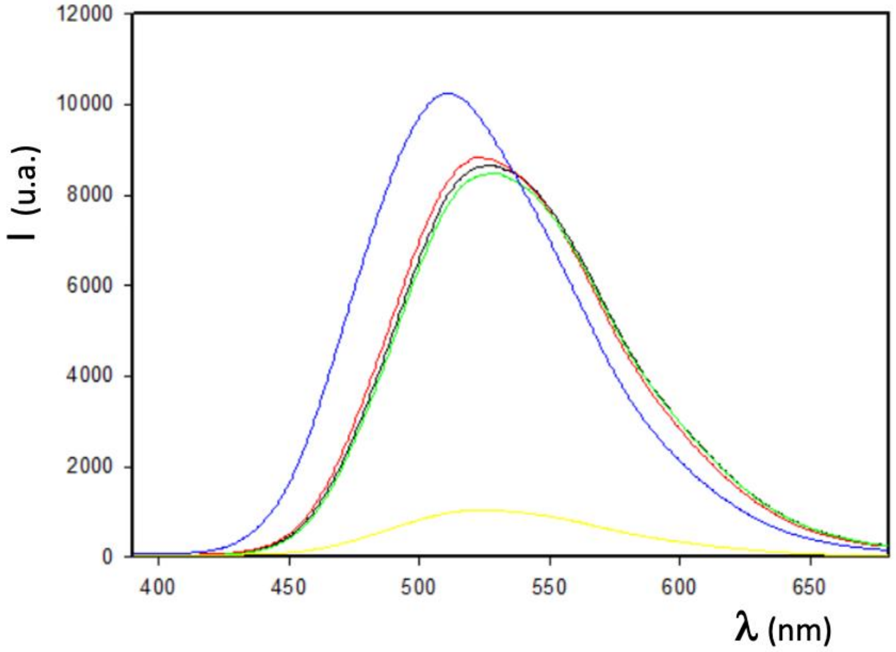

Figure 30. Fluorescence spectra (λ_{exc} = 350 nm) in CH_3CN/DMSO solution (9:1 v/v) of **L1** (black curve), **L2** (red curve), **L3** (green curve)**, L4** (yellow curve), and dansylamide (blue curve). The concentration was in all cases 10 µM.

The addition of KET, NPX and BzO as their sodium salts does not cause any change in the absorption spectra – excluding the expected increase due to the absorption of the added molecules – in the case of all hosts except **L4**. In this latter case, in fact, the addition of guest species causes a pronounced red-shift of the absorption band to 350 nm accompanied by an intensity increase (Figure 31-33). An isosbestic point can be clearly observed in all cases (for NPX, adding an equal amount of the drug to the reference, to take into account its absorption) at 330 nm. These changes in the absorption spectra can be attributed to the involvement of the indole units in the hydrogen bonding with the analytes, in agreement with what observed in the ^{1}H-NMR studies.

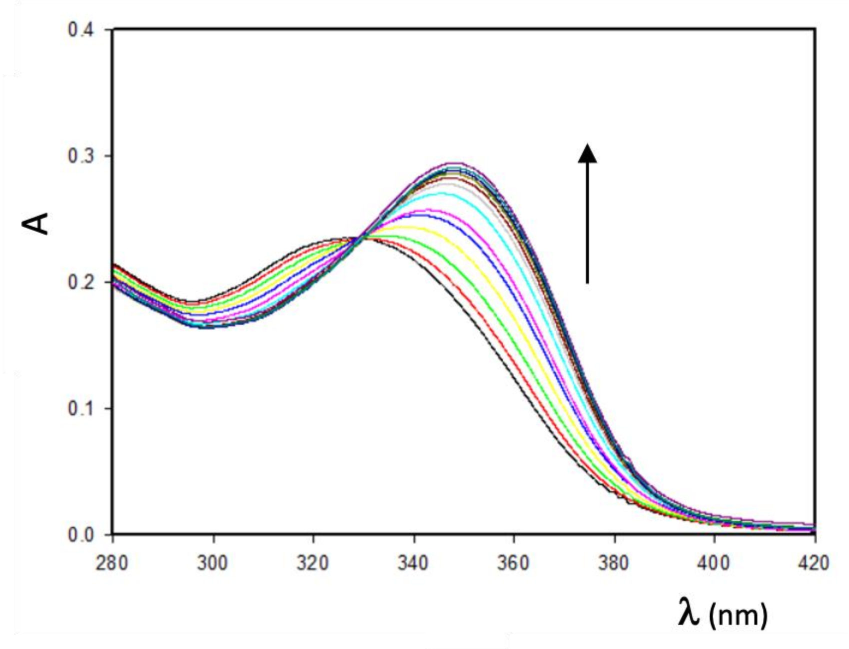

Figure 31. Absorption spectra in CH_3CN/DMSO solution (9:1 v/v) of **L4** (10 µM) upon addition of increasing amounts (0 – 5 equiv) of BzO^-.

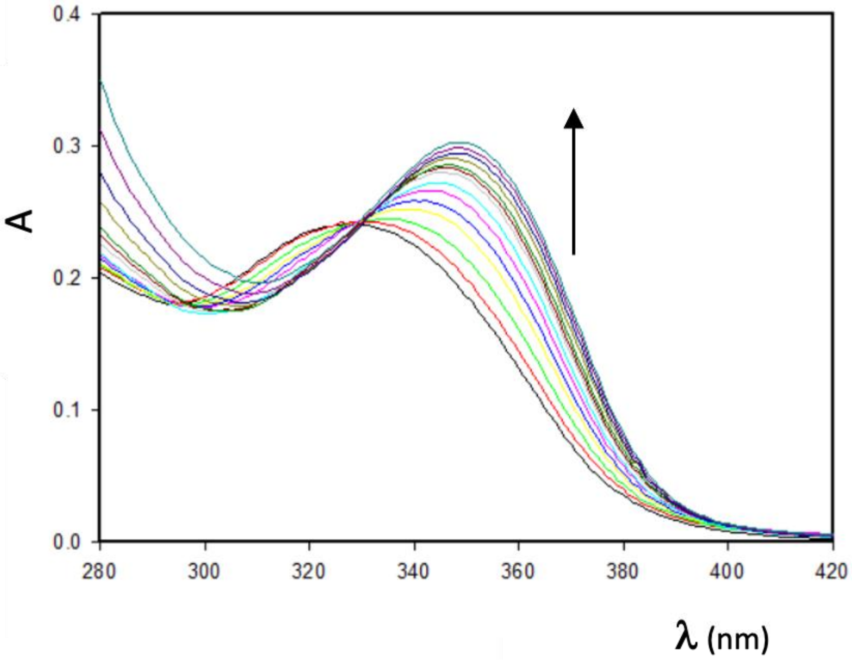

Figure 32. Absorption spectra in CH_3CN/DMSO solution (9:1 v/v) of **L4** (10 µM) upon addition of increasing amounts (0 – 5 equiv) of KET as its sodium salt.

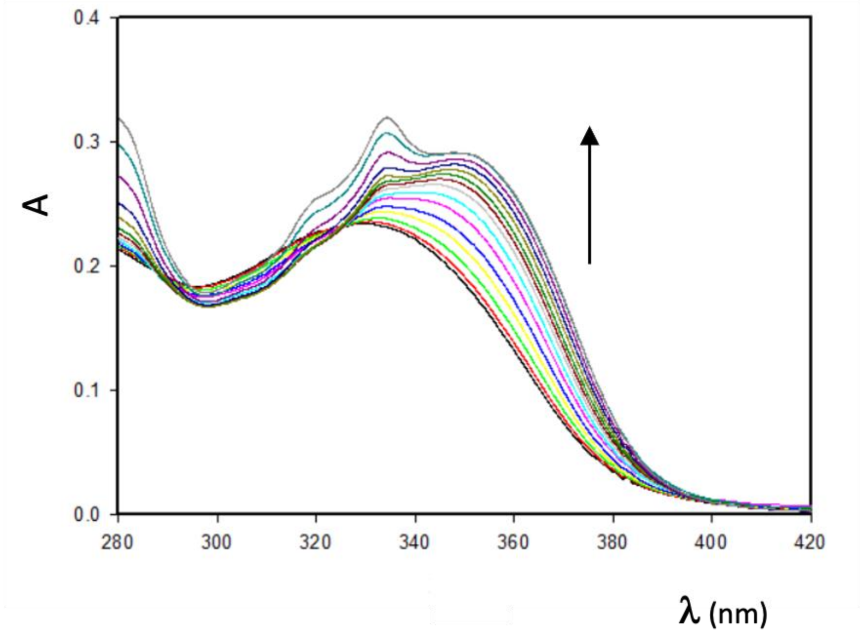

Figure 33. Absorption spectra in CH_3CN/DMSO solution (9:1 v/v) of **L4** (10 µM) upon addition of increasing amounts (0 – 5 equiv) of NPX as its sodium salt.

Interestingly, the changes observed in the fluorescence emission are much more relevant. In particular, the macrocycles **L1** and **L2** show a strong quenching (63% and 71% of the initial value, respectively) upon the addition of KET^{-}, while their emission remains almost constant upon the addition of NPX^{-} and BzO^{-}, as shown in Figure 34 in the case of **L1** and Figure 35 in the case of **L2**, respectively.

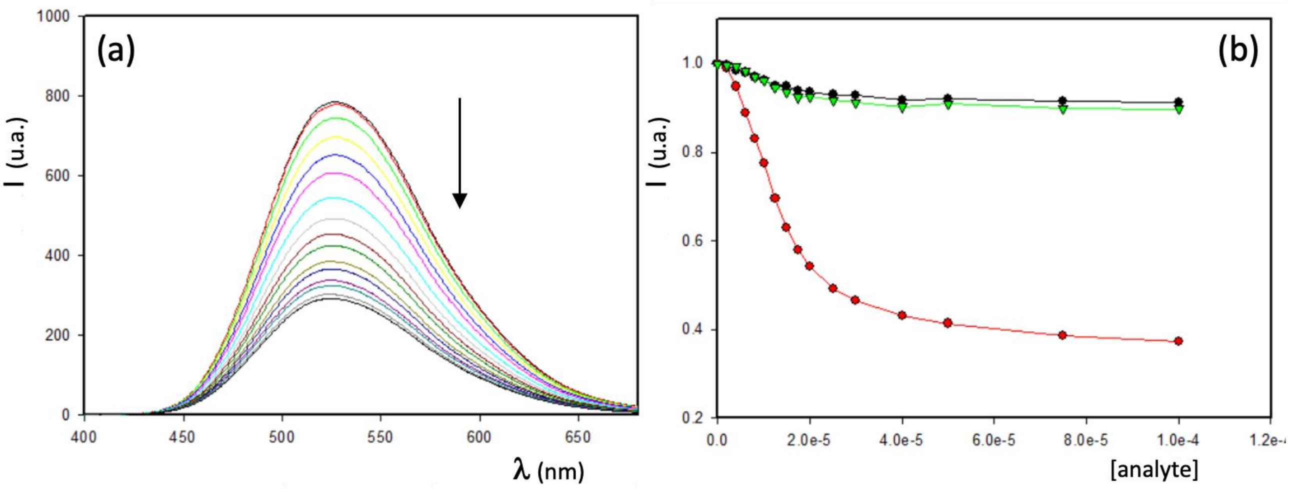

Figure 34. (a) Fluorescence spectra (λ_{exc} = 350 nm) in CH_3CN/DMSO solution (9:1 v/v) of **L1** (10 μM) upon addition of increasing amount of the sodium salt of KET^{-}; (b) normalized fluorescence intensity (λ_{exc} = 350 nm; λ_{em} = 525 nm) of **L1** (10 μM) upon addition of increasing amount of KET (red circles), NPX (green triangles), and BzO (black circles) as their sodium salt.

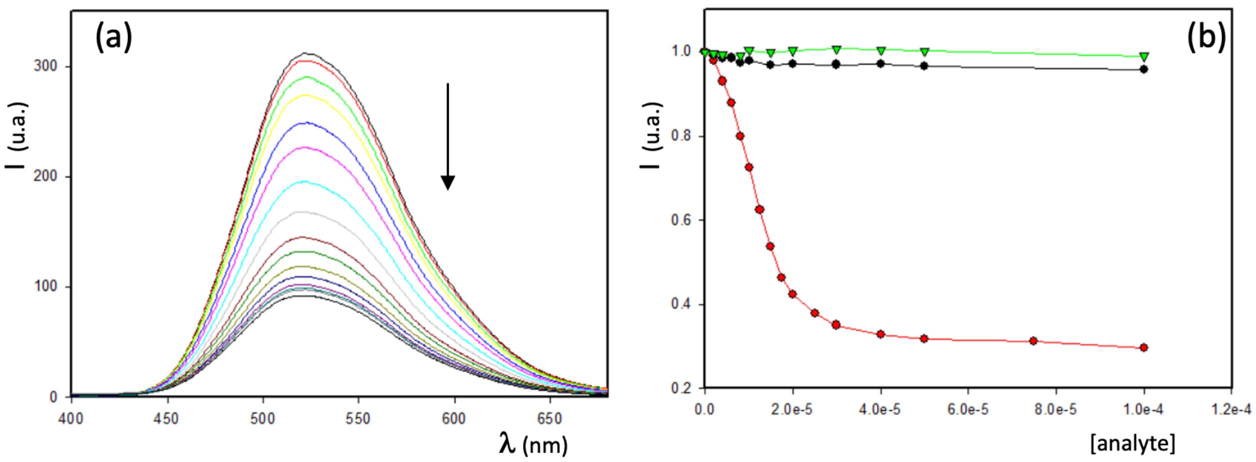

Figure 35. (a) Fluorescence spectra (λ_{exc} = 350 nm) in CH_3CN/DMSO solution (9:1 v/v) of **L2** (10 µM) upon addition of increasing amount of KET^-; (b) normalized fluorescence intensity (λ_{exc} = 350 nm; λ_{em} = 525 nm) of **L2** (10 µM) upon addition of increasing amount of KET (red circles), NPX (green triangles), and BzO (black circles) as their sodium salt.

From the observed quenching, we were able to determine the association constants[45] with KET^- of both **L1** (9.4×10^4 M^{-1}) and **L2** (8.3×10^4 M^{-1}). Together with the observed intensity decrease, the addition of KET^- led also to a change of the excited state decay, see Figure 36. In particular, two different lifetimes – both shorter than that measured in absence of the drug (4.5 and 9.0 ns for **L1**, Table 1; 2.8 and 6 ns for **L2**, Table 2) – could be observed in the presence of KET^-.

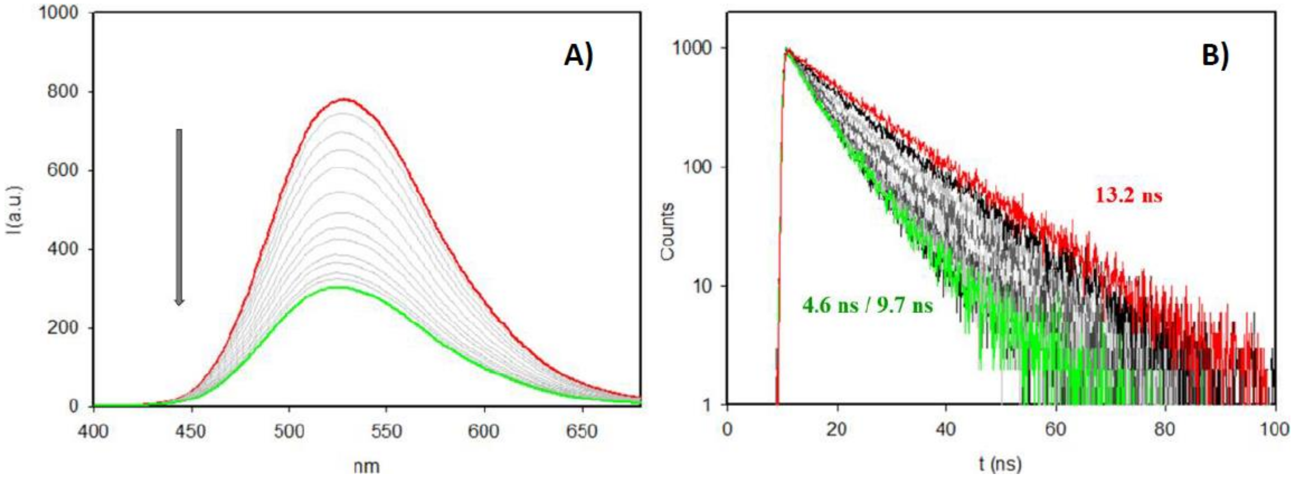

Figure 36. (a) Fluorescence quenching of **L1** upon addition of increasing amount of KET⁻; (b) fluorescence lifetimes of **L1** during the titration with KET⁻.

L1/KET⁻	**t1 [ns]**	**t2 [ns]**	**B1 [Hz]**	**B2 [Hz]**	**x^2**
0 eq	13.2	–	915	–	1.00
0.5 eq	4.0	12.6	180	795	1.00
1 eq	4.8	12.7	364	590	1.00
1.5 eq	4.5	11.6	457	477	0.99
2 eq	4.6	10.9	584	409	0.99
3 eq	4.6	10.0	652	380	1.00
4 eq	4.3	9.2	598	410	1.00
5 eq	3.75	8.2	442	496	1.00
7.5 eq	4.3	8.3	546	420	0.99
10 eq	4.6	9.7	728	215	0.99

Table 1. Fluorescence lifetimes of **L1** during the titration with KET⁻ and respective magnetic fields with each addition of the drug.

L2/KET^{-}	**t1 [ns]**	**t2 [ns]**	**B1 [Hz]**	**B2 [Hz]**	**x^{2}**
0 eq	**12.57**	–	1004	–	1.00
0.5 eq	3.95	12.51	410	578	0.98
1 eq	3.73	9.63	684	337	0.98
1.5 eq	3.92	9.15	779	247	1.00
2 eq	3.13	7.26	620	432	0.98
3 eq	3.43	7.20	665	358	0.98
4 eq	3.51	7.29	727	359	0.99
5 eq	3.30	6.71	619	383	0.99
7 eq	3.14	6.21	525	494	0.96
10 eq	**2.79**	**6.04**	486	527	0.99

Table 2. Fluorescence lifetimes of **L2** during the titration with KET^{-} and respective magnetic fields with each addition of the drug.

To gain additional insight into the possible interference by other analytes, we performed titration experiments with KET^{-} also in the presence of BzO^{-}, obtaining a shift in the titration curve (Figure 37). This shows that **L1** and **L2** form adducts with BzO^{-}, without appreciably perturbing the photophysical properties, indicating that they are not selective but sensitive to KET^{-}.

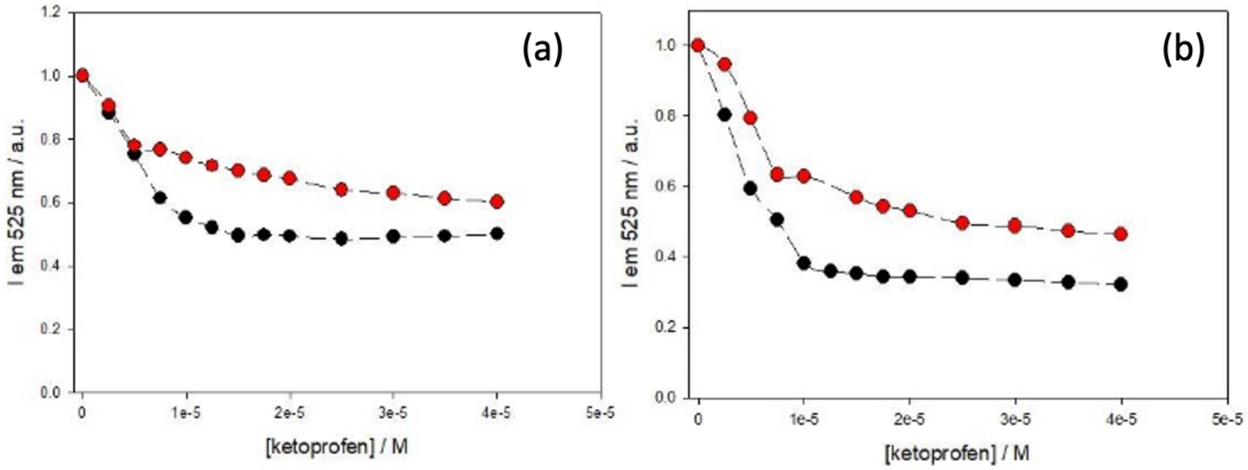

Figure 37. Trends of emission intensities (λ_{exc} = 350 nm; λ_{em} = 525 nm) in CH_3CN/DMSO solution (9:1 v/v) of 10 μM of (a) **L1** and (b) **L2** upon increasing amount of KET^- in absence (black) and in presence (red) of 10 μM of BzO^-. All the intensities were normalized on the emission of the probes before any addition of KET^-.

The two open ligands, **L3** and **L4**, on the contrary, while responding in a similar way to KET^-, with an intensity decrease of 56% and 68%, respectively, underwent a drop in the fluorescence intensity also upon the addition of BzO^- and NPX^- (see Figures 38-39). In all cases the observed quenching of the fluorescence of the dansyl unit is accompanied by a bi-exponential decay of the excited state. The lifetimes are again in all cases shorter than that of the free ligands. In the case of **L3** the two observed lifetimes are 12.6 and 4.1 ns after the formation of the adduct with KET^-, 11.8 and 4.0 ns after the addition of BzO^-, and 10.9 and 3.8 ns in case of NPX^-. Interestingly, in the case of KET^-, the highest pre-exponential term (the ratio is ca. 1.5) is associated with the shorter lifetime, while in the other two cases the opposite is true (the ratios being 4.5 and 7.5 for BzO^- and NPX^-, respectively), in agreement with the higher quenching observed with KET^- in case of **L4**.

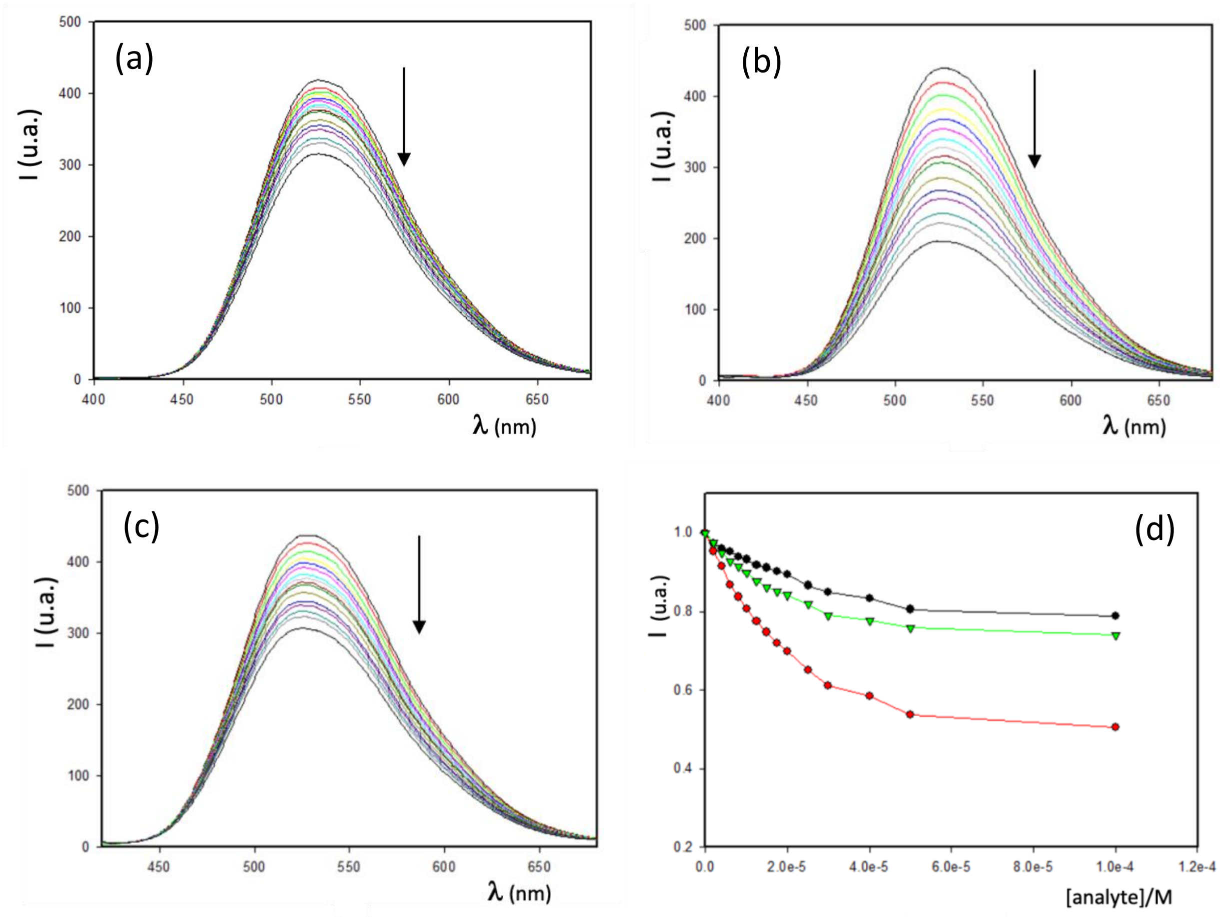

Figure 38. Fluorescence spectra (λ_{exc} = 350 nm) in CH_3CN/DMSO solution (9:1 v/v) of **L3** (10 µM) upon addition of increasing amount of BzO^- (a), KET^- (b) and NPX^- (c); (d) normalized fluorescence intensity (λ_{exc} = 350 nm; λ_{em} = 525 nm) of **L3** (10 µM) upon addition of increasing amount of KET (red circles), NPX (green triangles), and BzO (black circles) as their sodium salt.

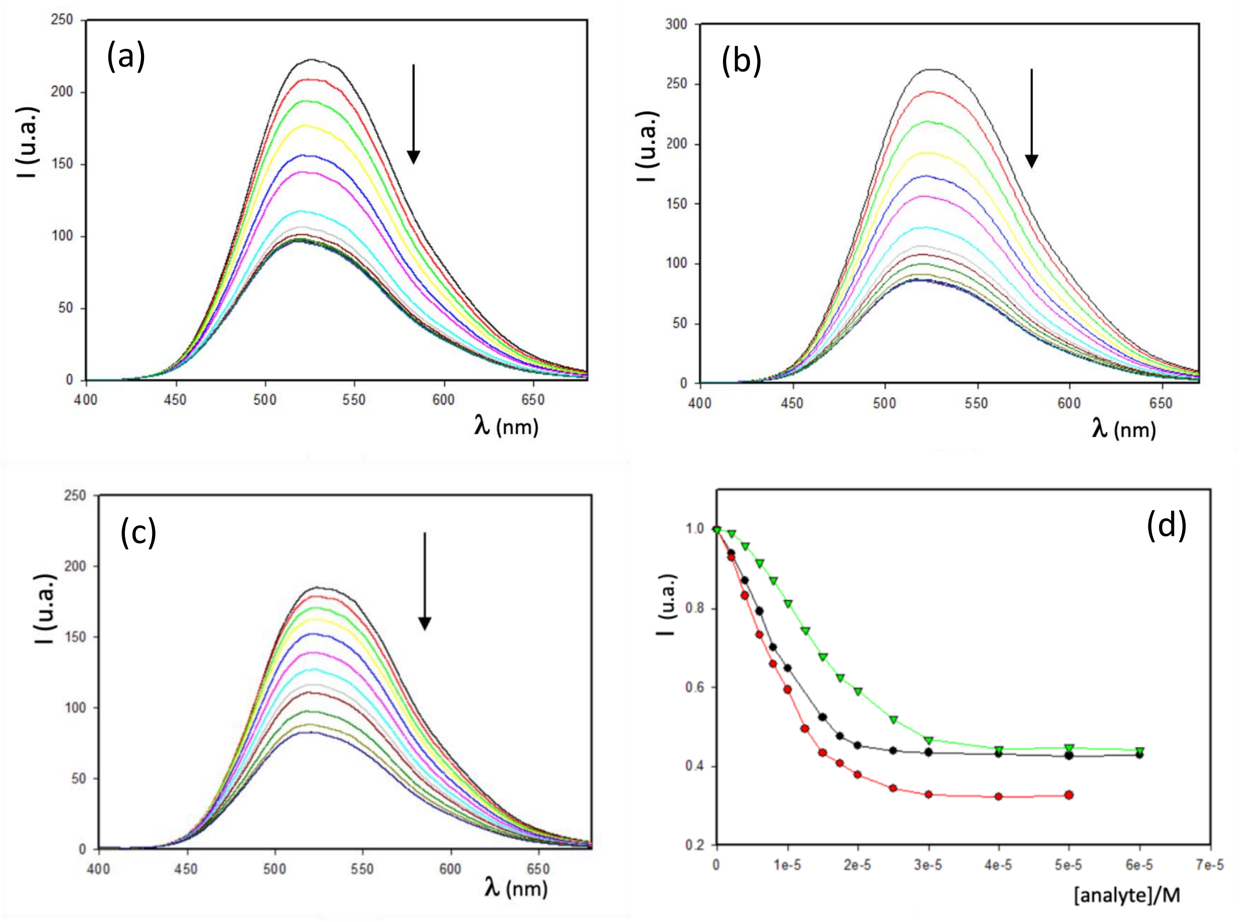

Figure 39. Fluorescence spectra (λ_{exc} = 350 nm) in CH_3CN/DMSO solution (9:1 v/v) of **L4** (10 µM) upon addition of increasing amount of BzO^- (a), KET^- (b) and NPX^- (c); (d) normalized fluorescence intensity (λ_{exc} = 350 nm; λ_{em} = 525 nm) of **L4** (10 µM) upon addition of increasing amount of KET (red circles), NPX (green triangles), and BzO (black circles) as their sodium salt.

The association constants between the ligands **L1**-**L4** and the different analytes are gathered in Table 3. In the case of **L1**-**L3**, in which the absorbance of the receptors does not change during the titration, the constants have been obtained fitting the fluorescence data, while in the case of **L4** the association processes have been obtained from the absorption spectra, since following changes in the fluorescence spectra in this case would have caused the need of suitable corrections[46], increasing the associated errors. Similar values respect to the first association constant could be however estimated also from the fluorescence data.

Ligand/Analyte	**Ka x 10^4 (M^{-1})**		
	KET^-	**NPX^-**	**BzO^-**
L1	9.4 ± 0.6%	n.d.	n.d.
L2	8.3 ± 1%	n.d.	n.d.
L3	7.8 ± 0.3%	8.6 ± 0.3%	2.7 ± 0.7%
L4	16 ± 2.5%	1.6 ± 0.6%	2.3 ± 2.1%

Table 3. Association constants ($\cdot 10^4$) in CH_3CN/DMSO solution (9:1 v/v) of **L1-L4** with KET, NPX and BzO as their sodium salts.

In general, as reported in Table 3, the affinity of **L3** and **L4** for KET^- is similar to the one of the macrocycles **L1** and **L2** and comparable to the one with NPX^-; a slightly lower values has been obtained for BzO^-. It should be underlined that also with these ligands the highest intensity decrease has been observed for KET^-.

Although none of the presented hosts binds KET^- selectively, their differential response can allow designing efficient arrays for the determination of polluted samples.

The ability of **L1** and **L2** to sensing KET as its sodium salt over the other guests was thus tested performing a strip test by soaking a paper in a well grinded suspension of the ligands in ethanol. Following complete drying, the paper showed, as expected, a blue-green fluorescence under illumination with 360 nm UV lamp. Deposition of guest ethanolic solutions was then performed (Figure 40), revealing that the fluorescence is quenched in the case of KET$^-$ and mixed guests, while NPX$^-$ and BzO$^-$ seemed to have no effect. Under these conditions, in order to appreciate the switching-OFF of the fluorescence on the paper strip, substrate concentrations as 10^{-3} M, corresponding to about 100 folds the concentration of the sensor, are needed.

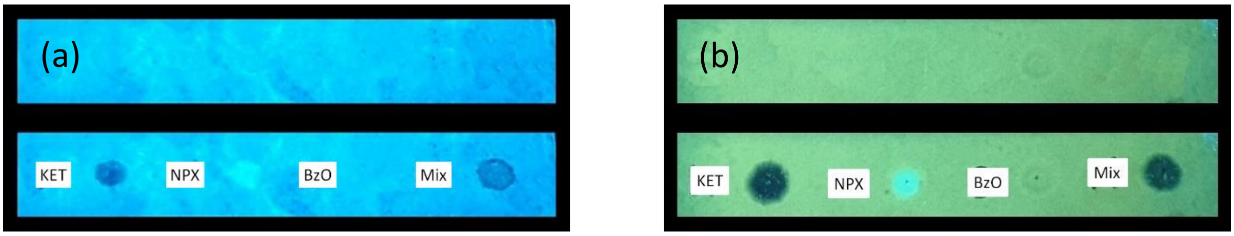

Figure 40. Strip tests of **L1** (a) and **L2** (b) with addition of NPX$^-$, KET$^-$, BzO$^-$ and three guests mixed (illumination at 360 nm).

2.1.4 Theoretical calculations

Calculations were carried out at the density functional theory (DFT)[47,48,49,50] level in order to investigate the structural and energetic features of the interactions between the dansylate squaramide-based ligands and the anionic forms of the investigated anti-inflammatory drugs. DFT calculations were proved to be particularly well-suited for probing intermolecular interactions involving hydrogen bonds (HB),[51,52] halogen bonds (XB),[53,54] and chalcogen bonds (ChB),[55,56,57] providing excellent results, comparable with those achieved by post-HF perturbative methods, at an affordable computational cost. Following the very encouraging computational results obtained for related systems featuring XH and XB interactions,[30,58,59] the mPW1PW functional[60] was used along with the Def2SVP basis sets[61] for all atomic species.

BzO^- and KET^- were chosen as model anions. For both the geometry was optimized providing a very good agreement between the available structural data and the optimized metric parameters.[62] A TD-DFT investigation revealed a very weak absorption peak at about 280 nm (monoelectronic transitions at 4.339 and 4.418 eV; $f = 0.006$ and 0.009, respectively) for the benzoate anion and a broad band in the region 250-350 nm for the KET^- anion, due to the contribution of monoelectronic transitions calculated at 287, 332, and 335 nm (4.325, 3.737, and 3.698 eV; $f = 0.164$, 0.038, and 0.047, respectively).

As model squaramide-based chemosensors, ligands **L2** and **L4** were chosen. The absorption spectrum simulated for **L2** based on TD-DFT calculations shows a weak visible absorption at 371 nm (3.34 eV; $f = 0.088$), due to the HOMO-LUMO monoelectronic excitation, and a series of absorptions at about 250 nm resulting in a structured peak, mainly contributed by the allowed singlet vertical transition from the ground state (GS) to the manifold of excited state (ES) ranging between ES #13 and ES #31. The most intense of these transitions is the GS → ES #27 vertical transition (4.98 eV; $f = 0.341$), due to a monoelectronic excitation localized on the squaramide core. Notably, TD-DFT data are in very good agreement with the experimental absorption spectrum recorded for **L2** (Figure 29), showing the main absorption maximum at 4.35 eV. The absorption spectrum simulated for **L4** based on TD-DFT calculations shows a main peak bathochromically shifted with respect to that calculated for **L2**, in agreement with UV-Vis spectroscopic measurements, and attributed to the singlet electronic vertical transition from the ground state (GS) to the excited state (ES) #11 (4.081 eV; $f = 0.504$). This transition is mainly contributed by two monoelectronic excitation localized on the indol-7-yl substituent (KS-MO 204 → 208) and the squaramide core (KS-MO 206 → 210).

As expected, the maps of the electrostatic potential calculated for BzO^-, KET^-, **L2**, and **L4** show the most negative potential on the carboxylate endings of the anions, and the most positive potentials on the squaramide NH groups of **L2** and **L4** (Figure 41), suggesting that the electrostatic interaction may drive the anions to interact with ligands by means of HB interactions, in agreement with ^{1}H-NMR experiments (see above).

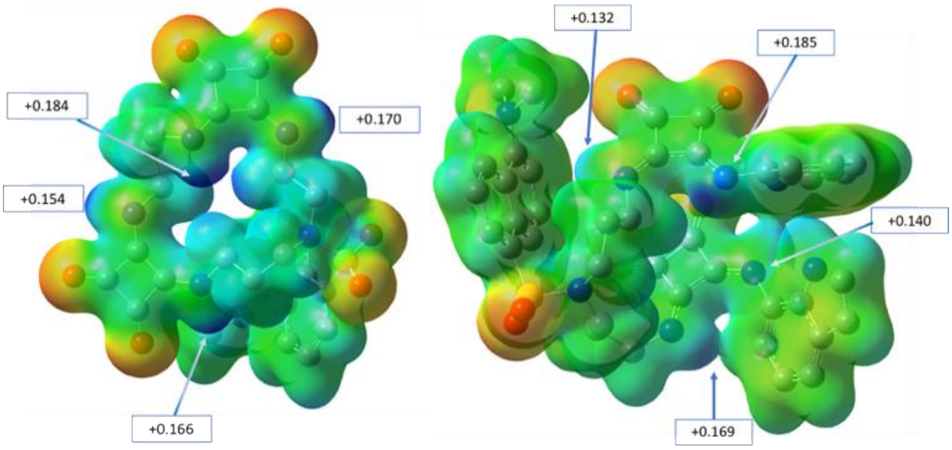

Figure 41. Molecular Electrostatic Potential (MEP) mapped on the electron densities (0.01 |e| Bohr^{-3}) for **L2** (left) and **L4** (right). Range –0.10 (red) – +0.18 (blue) a.u.

The 1:1 adducts between the ligands **L2** and **L4** and the anions BzO$^-$ and KET$^-$ were singly optimized to investigate the ligand-anion interactions. For each adduct several stable geometries were obtained, summarised in Table 4 (entries *a*-*j*) and Figure 42 for **L4**·KET$^-$ in its most stable optimized geometry.

Total electronic energies (*E*, Hartree), maximum absorption wavelength (λ_{max}, nm)[a] and relevant molar extinction coefficient (ε, 10^3 $M^{-1}\cdot cm^{-1}$),[a] adduct stabilization energies (ΔE, $kcal\cdot mol^{-1}$) and description of the type of HB in the adducts *a-j* between the ligands **L2**/**L4** and the anions BzO^-/KET^- optimized at DFT level.

Entry	**Adduct**	***E***	**λ_{max}[a,b]**	**ε**	**ΔE**	**Main interactions**
a	**L2**·BzO^-	–2721.4923	258	40	62.25	2 HB
b		–2721.5026	258	47	**68.68**	2 bifurc. HB
c	**L2**·KET^-	–3144.0988	256	53	60.38	2 HB
d		–3144.1090	256	56	**66.75**	2 bifurc. HB
e	**L4**·BzO^-	–3329.4688	318	33	58.39	2 HB
f		–3329.4986	324	52	77.06	2 bifurc. HB + 1 intramol. HB
g		–3329.4996	323	47	**77.75**	2 bifurc. HB + 2 ind.[c] HB
h	**L4**·KET^-	–3752.0799	309	24	59.43	2 HB
i		–3752.1047	324	52	**74.96**	2 bifurc. HB + 1 intramol. HB[c]
j		–3752.1030	324	46	73.92	2 bifurc. HB + 2 ind.[c] HB

[a] λ_{max} and ε value obtained from the convolution of the electronic excitations assuming a half-band width of 0.333 eV. [b] λ_{max} = 249 and 304 nm for **L2** and **L4**, respectively. [c] HB involving the NH indole group.

Table 4. Summary of the stable geometries obtained for each 1:1 adduct between the ligands **L2** and **L4** and the anions BzO^- and KET^-.

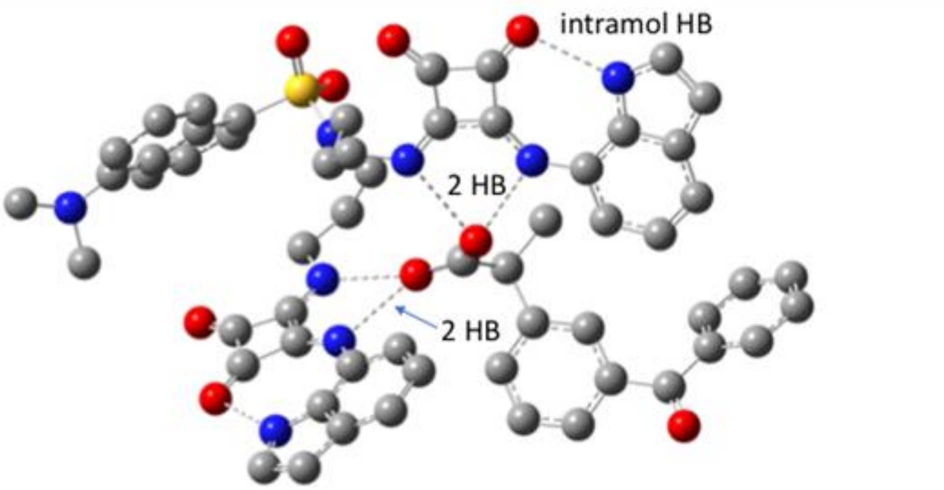

Figure 42. Optimized geometry of the most stable 1:1 adduct **L4**·KET⁻ (entry *i* in Table 4). The bifurcated hydrogen bonds as well as the intramolecular HB within **L4** were evidenced. Hydrogen atoms were omitted for clarity.

In general, the COO^- group of the anions can either form two HB interactions with the two NH of a single squaramide or bridge two squaramide systems by forming two bifurcated HBs. Depending on the final geometry, the indole N–H group can interact with a C=O of the bonded squaramide or even further strengthen the interaction with the anion with an additional intramolecular HB. Notably, the total electronic energies calculated for adducts of the same stoichiometry are marginally affected by the type and number of HBs formed. In general, the interaction of the anions with the ligand **L4** provides a larger stabilization than those formed by **L2**.

The absorption of the ligand in the adducts has been evaluated at DFT level (Table 4). In general, the interaction of **L2** and **L4** with both anions results in a bathochromic shift (by 20 nm in the gas phase) accompanied by an hyperchromic effect, both effect increasing with the number of HB interactions occurring between the ligand and the anion. Therefore, the red-shift of the ligand absorption band and the increase in the molar extinction coefficients observed because of the ligand-anion interaction represent possible parameters for evaluating the sensing ability of the tested ligands towards specific anions.

2.1.5 Conclusions

This study describes the behaviour of four fluorescent squaramide-based ligands providing a guideline for the realization of chemosensors suitable for the sensing of organic carboxylic anions, such as NSAID derivatives, that can be accounted in the emerging pollutants list. In particular, the thesis reports four ligands containing the N,N-bis(3-squarmidoylpropyl)dansylamide motif ($(SQ–CH_2–CH_2–CH_2)_2N–DNS$) as fluorescent receptive unit inserted in two macrocycles (**L1** and **L2**) and two open-chain systems (**L3** and **L4**).

As demonstrated by ^{1}H-NMR, UV-Vis and fluorescence studies, all ligands are able to interact with the selected guests (KET, NPX and BzO as sodium salts) in organic solvents. Notably, the macrocyclic systems **L1** and **L2** show a specificity in the fluorescence response to KET$^–$. In fact, while the open-chain ligands **L3** and **L4** undergo a quenching of the fluorescence upon addition of KET, NPX and BzO as their sodium salts, the macrocyclic systems **L1** and **L2** were quenched only by KET$^–$. This aspect underlines the role of the highly organised macrocyclic structure to improve the specificity and/or the selectivity of a chemosensor. The ability of **L1** and **L2** to discriminate between KET$^–$ and the other examined guests was confirmed also using a strip-test.

Theoretical calculations performed on ligands **L2** and **L4** at DFT level confirm that the stabilization of the adducts with KET$^–$ and BzO$^–$ is mediated by H-bond interactions between the squaramidic and/or indolic NH groups (donors) of the hosts and the carboxylate groups of the guests. However, the macrocyclic skeleton balances the more HB contacts of **L4** giving similar K_{ass} values.

Summarizing the results of these studies, it can be deduced that the pre-organization and the abundance of H-bond donors are the two main factors that should be considered in order to design receptors able to respond to a specific anion. Moreover, the possibility to realize chemosensors with different response can allow for the design of efficient arrays for the determination of polluted samples.

2.2 Results and Discussion of L6 and L7

2.2.1 Synthesis

The synthetic strategy adopted to obtain **L6** and **L7** ligands is outlined in Scheme 7.

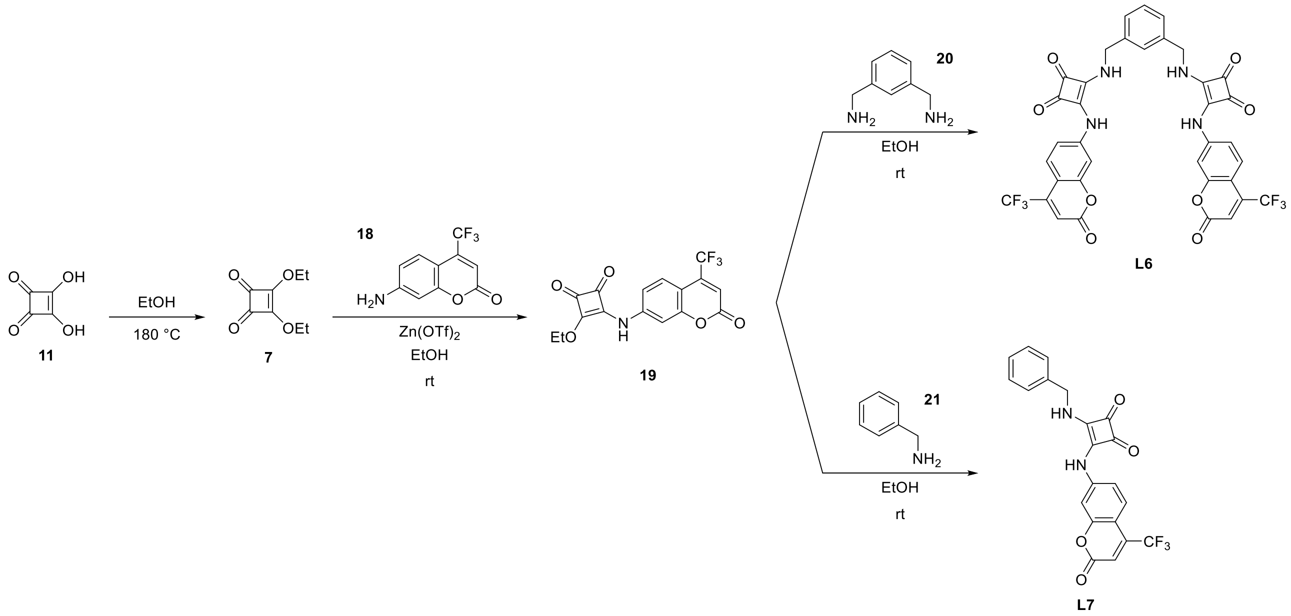

Scheme 7. Synthesis pathways to obtain ligands **L6** and **L7**.

The preparation of the ethyl squarate **7** starting from the initial squaric acid **11** is perfectly identical to that used in the chapter on dansyl-based ligands. 7-amino-4-(trifluoromethyl)coumarin **16** was chosen as the fluorescent coordinating unit, so that it was possible to follow the interaction between the ligand and the analyte through spectrophotometric techniques. This attachment phase is the limiting step of the entire synthetic pathway, due to the lower reactivity of this coumarin as an aromatic amine and, above all, to the fact that it is electron poor for the presence of the CF_3 group. In order to overcome this problem we proceeded, similarly to the synthesis of **L4**, by coupling diethylsquarate **7** with coumarin **16** in the presence of a catalytic quantity of zinc triflate (20% mol).[34] In this way the attachment of a single aromatic nucleophile on the hydrogen bond donor fraction is selectively obtained. A second advantage offered by this synthetic strategy lies in the limited solubility of **19** in ethanol at room temperature: once the bond has taken place, the product precipitates spontaneously and it is therefore possible to filter and separate it from the solvent. Eventually, by reacting the intermediate **16** with the diamine **20** (in a 2:1 ratio) and with the monoamine analogue **21** (in a 1:1 ratio) in warm ethanol, the ligands **L6** and **L7** are obtained. As in the case of the starting **16**, the two ligands also precipitate in the reaction mixture with a high purity and only filtration and washing with EtOH are necessary to eliminate the minimum impurities present.

2.2.2 Photophysical characterization

The absorption spectra in DMSO of **L6** and **L7** are very similar: they show an intense band ($\varepsilon = 45600$ $M^{-1} \cdot cm^{-1}$ and $\varepsilon = 25000$ $M^{-1} \cdot cm^{-1}$, respectively) centred at 400 nm where the coumarin chromophore absorbs, see Figure 43. As expected, the molar absorption coefficient of **L6** is almost double that of **L7** as these two sensors represent the double arm and single arm versions of the same sensor and they have been synthesized to study the possible cooperative effect of the double branching with respect to the single one. The absorption of the squaramides does not significantly perturb the absorption of the coumarin moiety. The band of lower intensity centred at 515 nm, on the other hand, is attributable to the deprotonation band of the squaramidic NH groups, which will be studied below to obtain information on the behaviour of the ligands in the coordination with the sodium salts of NSAIDs.

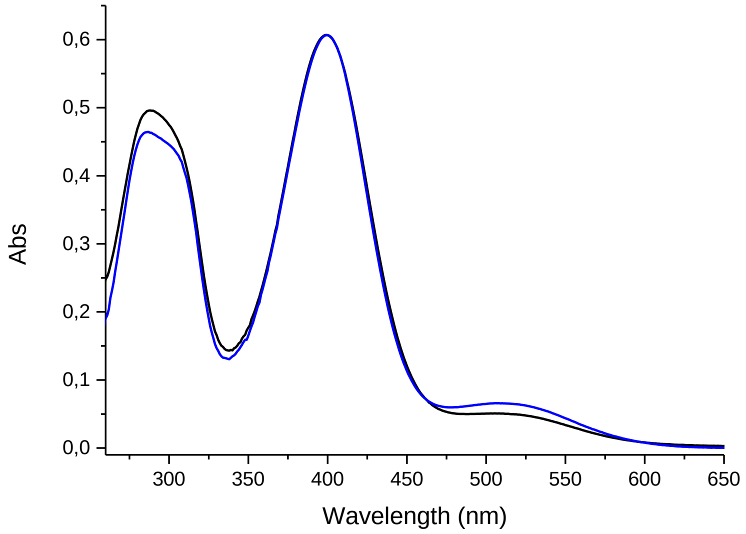

Figure 43. Absorption spectra in DMSO solution of the hosts **L6** (black) and **L7** (blue).

As far as the emission spectra are concerned, at room temperature in DMSO and CH_3CN/DMSO solution neither **L6** nor **L7** does not show any fluorescence emission, probably because coumarins are totally deactivated by the conjugation with squaramides and due to their electron-withdrawing conjugative effect.

The addition of IBU, DCL, KET and NPX as their sodium salts causes changes in the coumarin band and in the squaramidic NH groups band (Figure 44): the first decreases while the second one increases in intensity, both up to a maximum represented by the achievement of 2 equivalents of titrant.

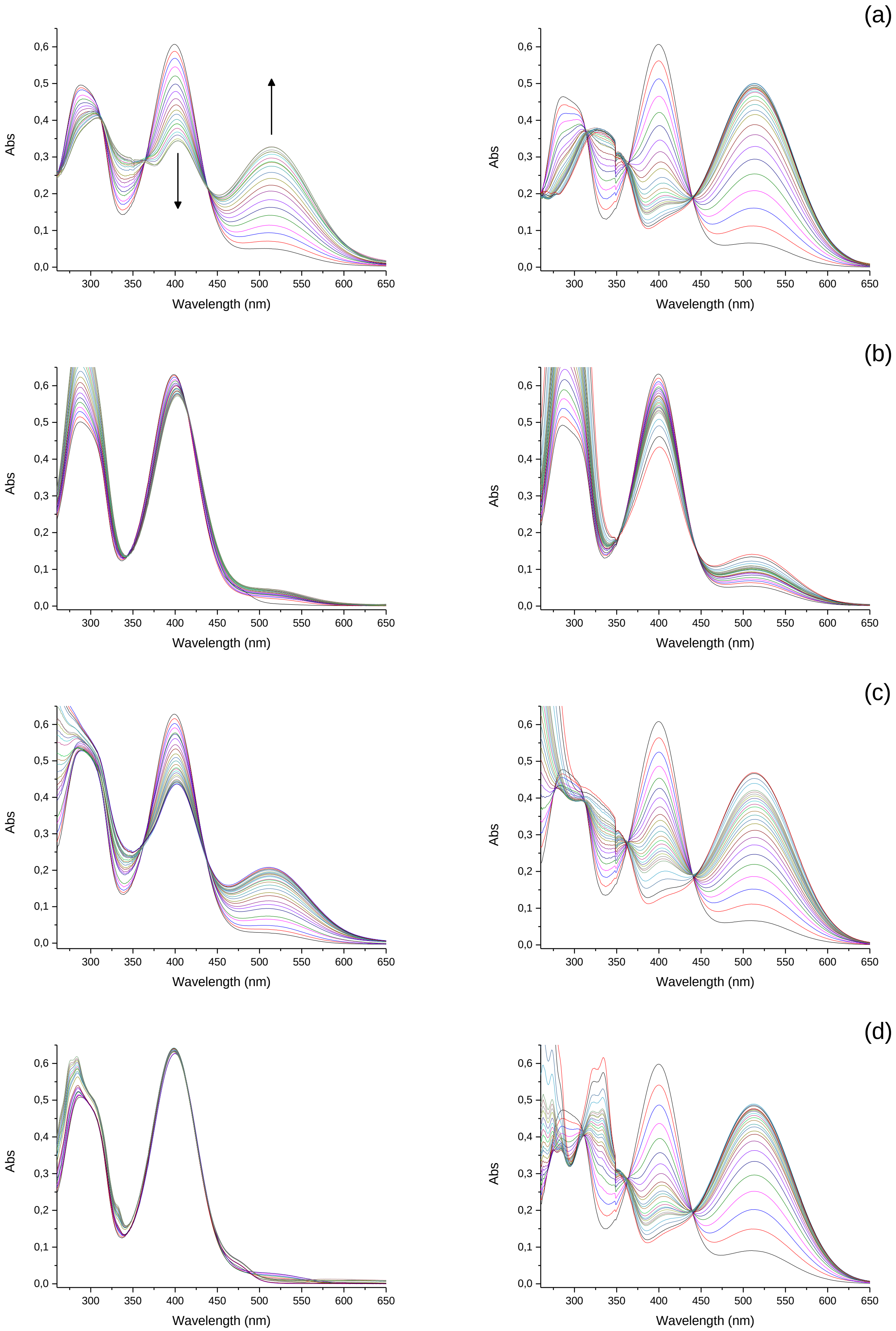

Figure 44. Absorption spectra in DMSO of **L6** (left) and **L7** (right) 1 µM upon addition of increasing amounts (0 – 2 eq) of IBU⁻ (a), DCL⁻ (b), KET⁻ (c) and NPX⁻ (d).

In each of the cases, with both ligands, there is a similar spectrophotometric behaviour, with differences in intensity and variation of the bands given by the topology of the anti-inflammatory drug and by the geometric complementarity with the chemosensors. Taking into account the potentially acidic nature of the squaramidic hydrogens, which is also increased by the working solvent in question (DMSO), it was necessary to confirm whether what emerges from the spectrophotometric titrations was really a host-guest coordination or simply an acid-base reaction between the ligands and the sodium salts of NSAIDs (basic molecules). In order to answer this question, titrations of **L6** and **L7** with NaOH in the same conditions were carried out.

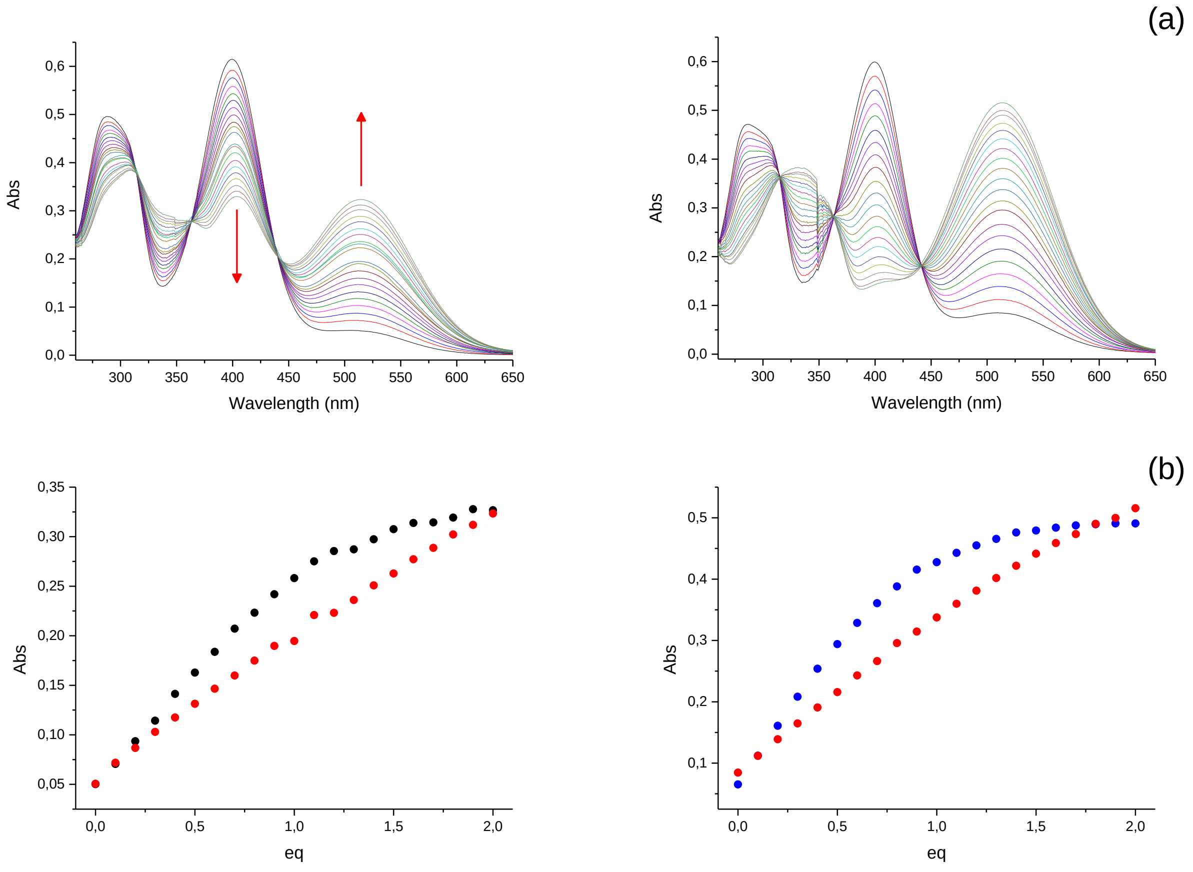

Figure 45. (a) Absorption spectra in DMSO of **L6** (left) and **L7** (right) 1 μM upon addition of increasing amounts (0 – 2 eq) of NaOH; (b) comparison of absorbance trends (λ_{abs} = 515 nm) of **L6** and **L7** upon addition of increasing amount of IBU^{-} (black/blue circles) and NaOH (red circles).

As can be seen from Figure 45, although the UV-Vis spectra seem to be perfectly identical as the previous ones, the absorbance trends show a different progress. With the sodium salt of the IBU (taken as a reference among the NSAIDs used) the trend increases linearly up to 1 equivalent and then changes with an asymptotic progress up to 2 equivalents, thus showing a constant absorption (typical situation of receptor saturation). Titling instead with NaOH the situation is totally different: the trend shows a perfectly linear progress up to 2 equivalents, suggesting that what happens is a separate and diverse process from the previous one.

It is possible to assert with good certainty that in the case of the sodium salts of the NSAIDs there is actually a real sensing with the formation of a supramolecular adduct, while in the case of the presence of a base the deprotonation of the squaramides take place. The similar increase in the deprotonation band in the case of the IBU^{-} as well as in the case of the NaOH probably lies in the fact that in the deprotonation there is still a sort of “coordination” with the base and an elongation in the distance between the H and the O as preliminary step of acid-base reaction.

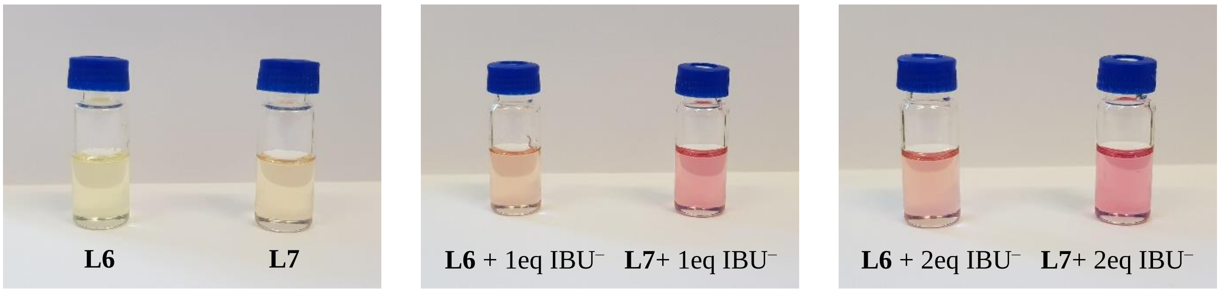

Figure 46. Identification of supramolecular complex formation by colour change.

2.2.3 ^{1}H-NMR studies

The coordination and the deprotonation processes are easily recognizable and distinguishable from each other and they have been studied and confirmed again with total security through NMR titrations. Host-guest interaction studies were conducted on **L6** and **L7** by means of ^{1}H-NMR titrations using DMSO-d_6/0.5% water as a solvent mixture; this little percentage of water has been added to decrease the acidity of the squaramides to avoid problems of acid-base nature. As in the case of dansyl-based ligands, the presence of squaramides results in a scarce solubility of **L6** and **L7** prevented to conduct ^{1}H-NMR studies in other solvents such as CD_3CN-d_3.

Below are reported only the titrations of **L6** and **L7** with IBU$^-$, Figure 47-48, as it is the structurally simpler NSAID among those analysed and which allows a clear following of the NMR signals of interest. The ^{1}H-NMR spectrum of the two ligands is almost similar as they represent the double arm and the single arm of the same sensor. All the signals have been attributed to the respective nuclei of H and during the formation of the supramolecular complex each peak, both of the host and of the guest, undergoes to an up-field shift, with the exception of H7 and H10. These two nuclei belong to the coumarin moiety which is not only responsible for the signal transduction (UV-Vis and colorimetric outputs), but it even actively participates in the coordination with IBU$^-$. Focusing in the aromatic area, indeed, when the guest is located inside the cavity defined by the two branches of **L6**, or simply coordinated by the single branch of **L7**, the two protons H7 and H10 are spatially close to the deshielded cones of the carbonyl group and of the aromatic ring of the drug, responsible for the anomalous down-field shift of the two protons under study.

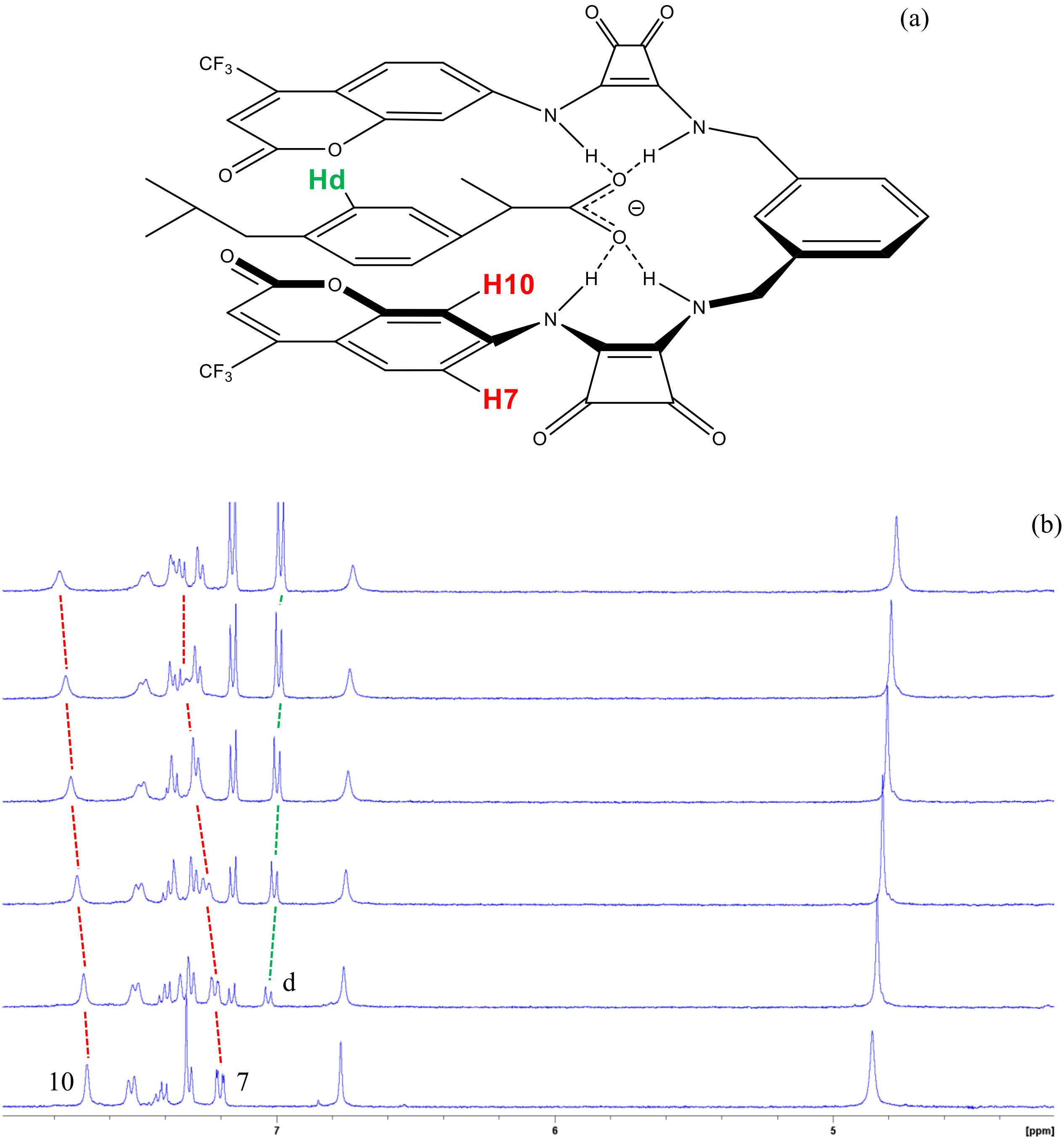

Figure 47. (a) Representation of the supramolecular adduct between **L6** and NaIBU; (b) stack plot of the ^{1}H-NMR titration of **L6** (4.26x10^{-3} M) in DMSO-d_6/0.5% water at 298 K in the presence of increasing molar ratios of NaIBU (0.035 M).

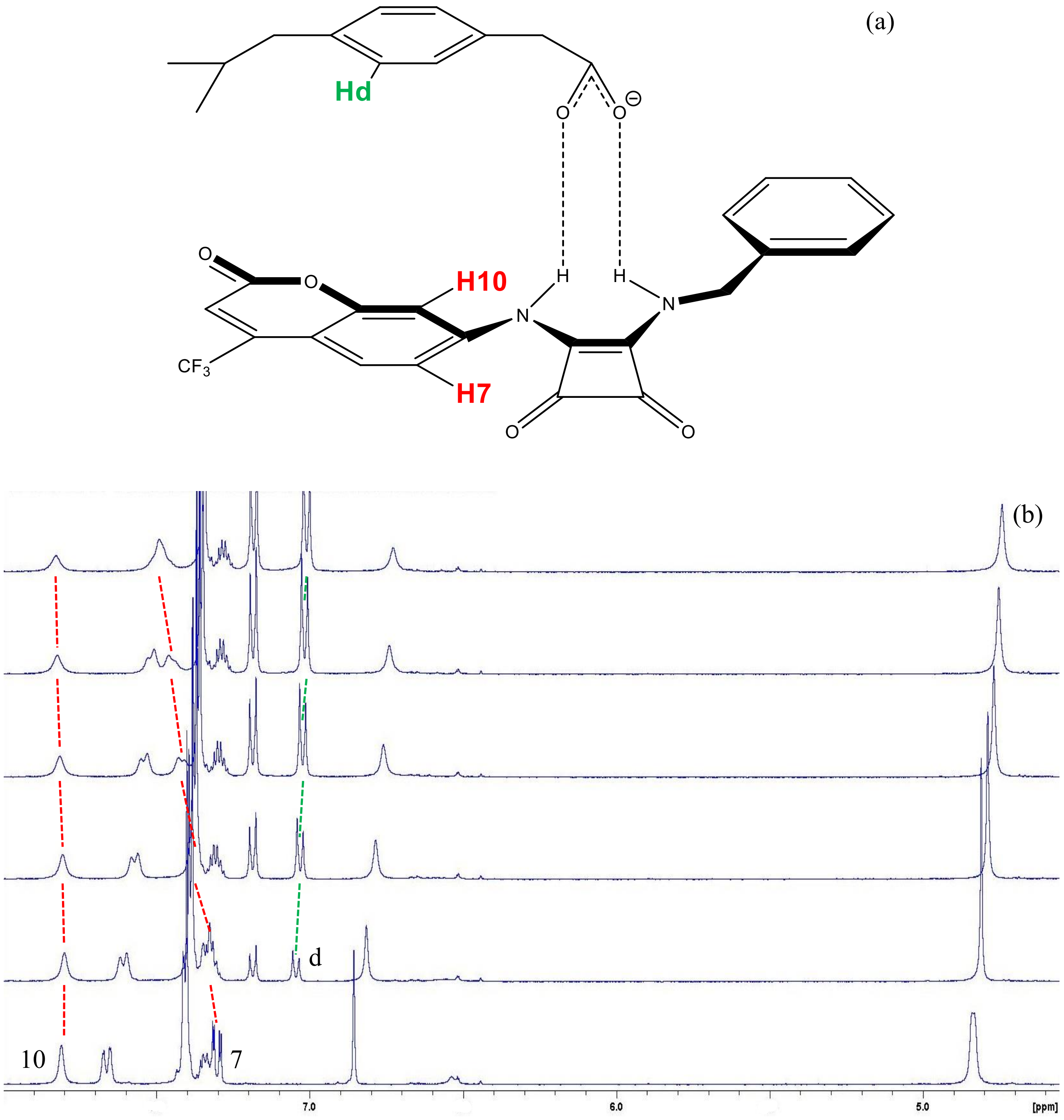

Figure 48. (a) Representation of the supramolecular adduct between **L7** and NaIBU; (b) stack plot of the ^{1}H-NMR titration of **L7** (7.36x10^{-3} M) in DMSO-d_6/0.5% water at 298 K in the presence of increasing molar ratios of NaIBU (0.052 M).

The subsequent comparison titrations with NaOH, Figure 49-50, undoubtedly demonstrated a different process, in agreement with UV-Vis titrations. During the addition of the base every single signal of the ligands undergoes to an up-field shift, including the nuclei H7 and H10. With the addition of the base, in fact, the deprotonation of the squaramidic NH takes place with the consequent appearance of a negative charge on the N atom and its dislocation in the four-member ring due to the mesomeric effect. The presence of this negative charge (and the shielding generated by the latter) in the proximity of the two nuclei under observation causes the concordant up-field shift with the other peaks, demonstrating the difference between a real sensing with a defined guest and a trivial acid-base reaction as in this case.

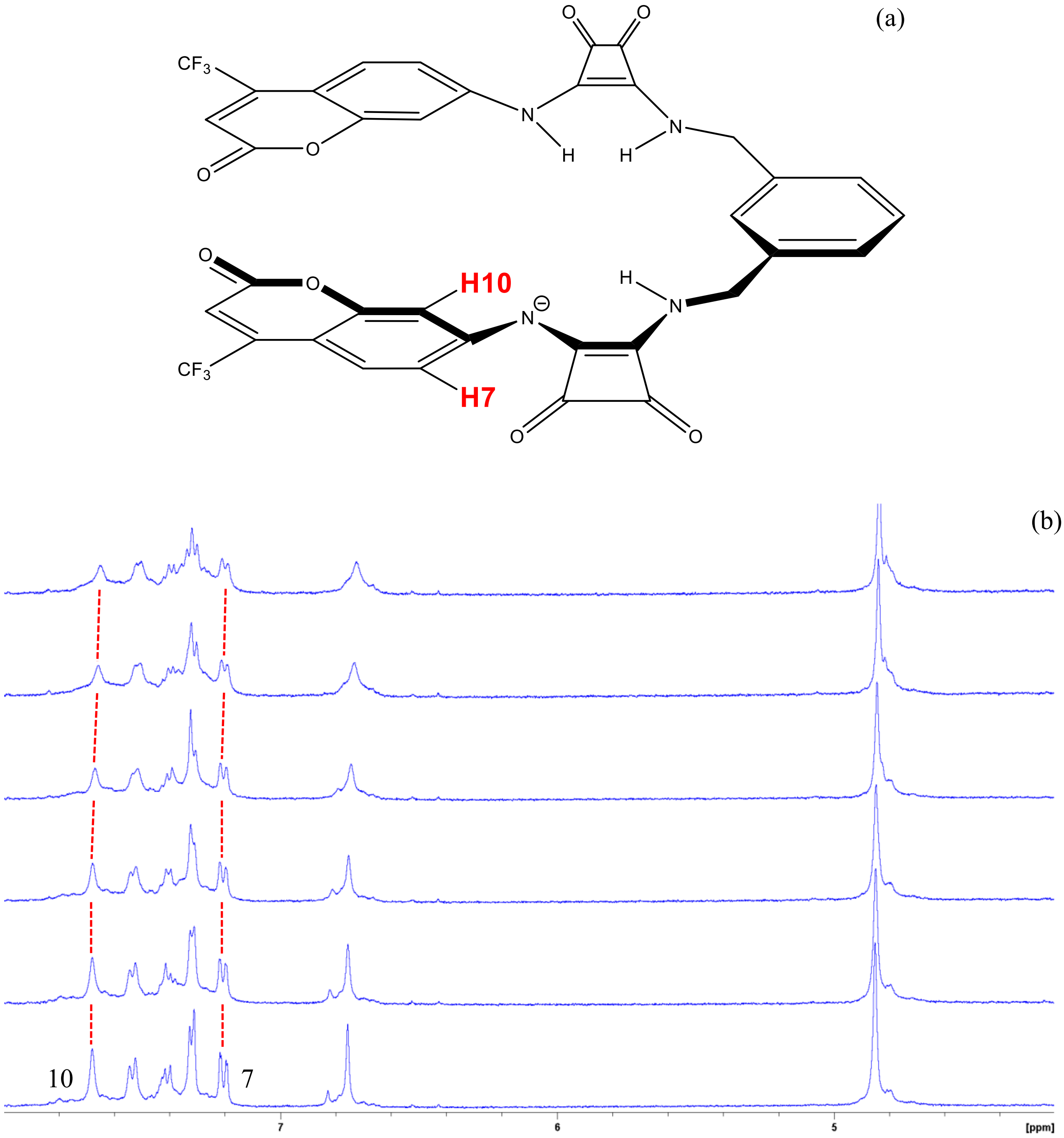

Figure 49. (a) Representation of the anionic form of **L6** after reaction with NaOH; (b) stack plot of the ^{1}H-NMR titration of **L6** (14.00×10^{-3} M) in DMSO-d_6/0.5% water at 298 K in the presence of increasing molar ratios of NaOH (0.08 M).

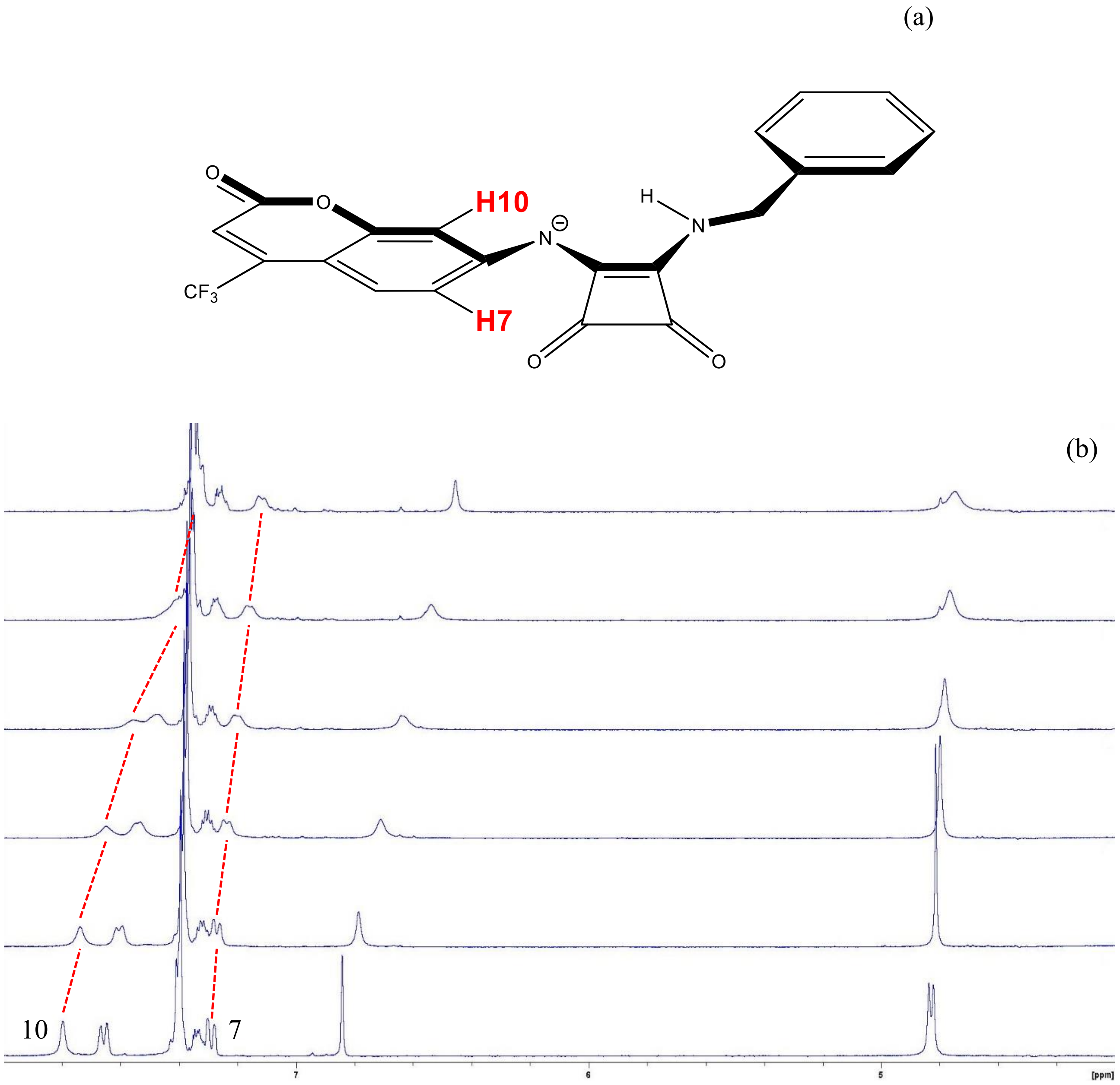

Figure 50. (a) Representation of the anionic form of **L7** after the reaction with NaOH; (b) stack plot of the ^{1}H-NMR titration of **L7** ($7.82\text{x}10^{-3}$ M) in DMSO-d_6/0.5% water at 298 K in the presence of increasing molar ratios of $TBNH_4OH$ (0.47 M).

2.2.4 Solid-state studies

The high insolubility of the ligands in the most common organic solvents, given by the presence of the squaramides, has been exploited to obtain crystals and have an idea of the three-dimensional conformation of the chemosensors. DMSO was chosen as crystallization solvent, capable of dissolving the ligant and representing the real working medium. The technique was a crystallization from hot DMSO, dissolving **L6** and **L7** in the minimum quantity of the solvent and subsequently subjecting them to a slow cooling down to room temperature. Only **L7** provided adequate crystals for X-ray analysis and the structure is shown in Figure 51.

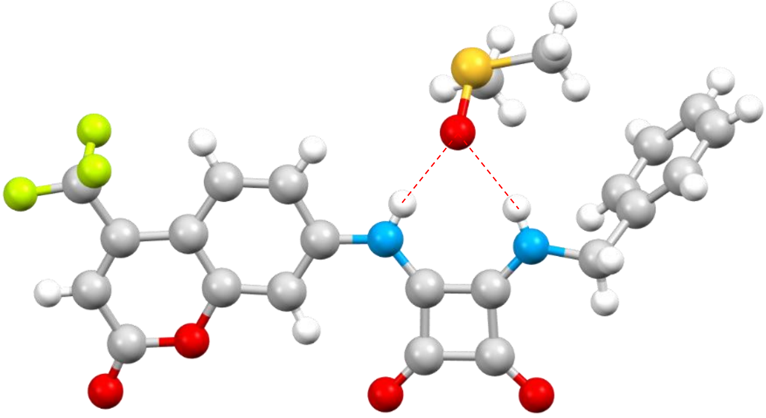

Figure 51. Structure of **L7** coordinated with DMSO obtained by X-ray crystallography.

As can be seen from the structure, all oxygens, including those of the coumarin moiety, face the same side. This may suggest that coumarin actually participates actively in the coordination through π–π interactions with the aromatic portion of the NSAIDs without involving the oxygen for polar interactions. The only exception to molecular planarity is given by the benzyl substituent which arises perpendicular to the branching. The relative ease of crystallization in this unconventional solvent (as it is not very volatile) is given by its coordination with the ligand. In fact, the DMSO is coordinated through the oxygen across two convergent hydrogen bonds given by the squaramidic NHs.

The greatest difficulty to obtain crystals with the ligant **L6** probably lies in the spatial arrangement of its ramifications. We were able to obtain a crystal structure of a further ligand of this family (not reported in this thesis) which could be taken as a model for the structure of **L6**. It is an analogue of it in which the two branches are connected by an ethylene chain. Similarly to **L7** it was crystallized from hot DMF, which coordinated between the two moieties of squaramide. As can be seen from the structure (Figure 52), the two branches are arranged specularly to each other, thus making it possible to form multiple intermolecular hydrogen bonds and a consequent helical stacking,[63] phenomenon that makes the molecule scarcely soluble and that does not create favorable conditions for an adequate crystallization.

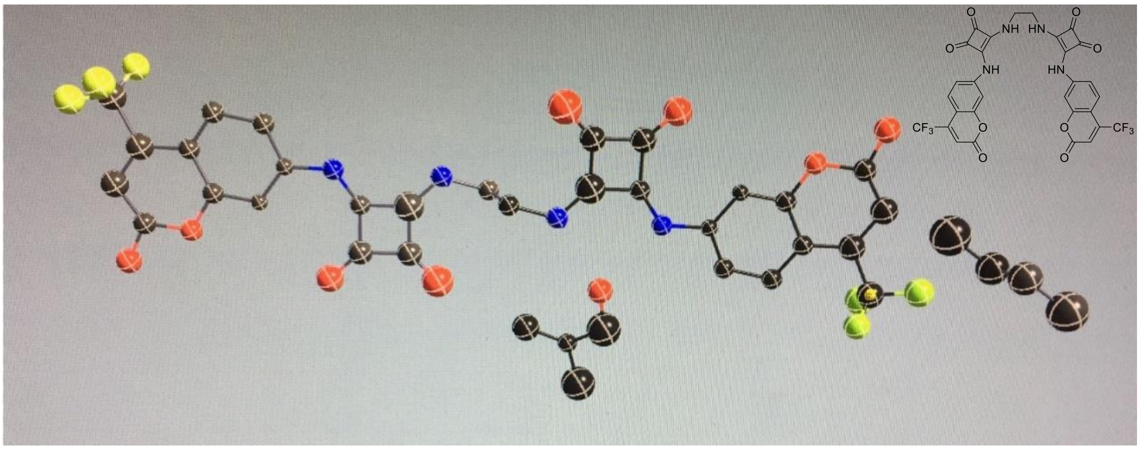

Figure 52. Structure of the **L6** analogue coordinated with DMF obtained by X-ray crystallography.

2.2.5 Conclusions

The ligands **L6** and **L7** can be obtained through and extremely simple and efficient synthesis and showed excellent ability to selectively bind NSAIDs with a clear spectrophotometric output. The formation of the supramolecular complex was studied by UV-Vis and NMR titrations and differentiated from the squaramides deprotonation process by analogous comparison titrations with NaOH under the same conditions. All UV-Vis titration curves were fitted by using the software HypSpec[64,65]. The results summarized in Table 5 show that the cooperative effect of the chelation given by the double arm of **L6** has not been achieved as the association constants are almost similar. The two ligands were not selective for the tested targets but they showed a high ability to discriminate and recognize the class of non-steroidal anti-inflammatory drugs with good sensitivity and short response time.

The table shows the association constants between the chemosensors and the guests. All the log *K* refer to a host-guest complexation ratio of 1:1.

L6		**L7**	
Reaction	**log *K***	**Reaction**	**log *K***
L6 + IBU^{-}	5.3(2)	**L7** + IBU^{-}	5.7(1)
L6 + DCL^{-}	5.8(3)	**L7** + DCL^{-}	3.2(2)
L6 + KET^{-}	5.1(2)	**L7** + KET^{-}	5.1(1)
L6 + NPX^{-}	–	**L7** + NPX^{-}	5.8(1)

All guests were added as sodium salts.

Table 5. Association constants in DMSO solution **L6** and **L7** with IBU, DCL, KET and NPX as their sodium salts.

2.3 Results and Discussion of L8

2.3.1 Synthesis

The receptor **L8** consisting of two “scorpiand” macrocyclic pyridinophane subunits connected by a luminescent biphenol spacer has been prepared for the first time. The synthetic strategy adopted to obtain it is outlined in Scheme 8.

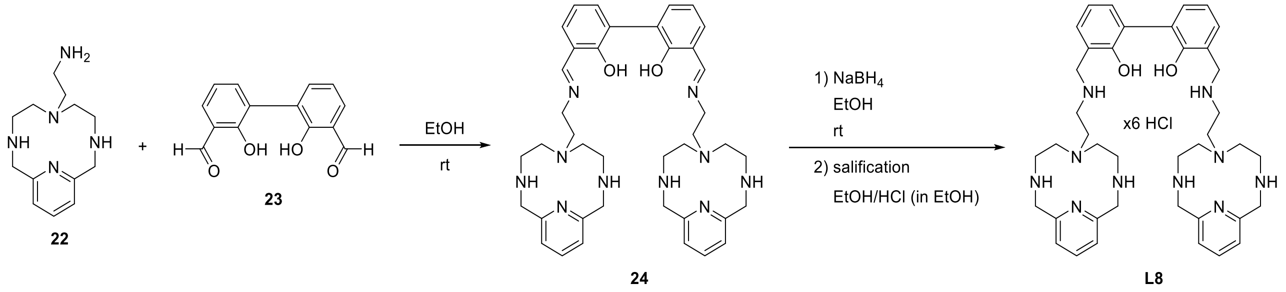

Scheme 8. Synthesis pathway to obtain ligand **L8**.

The synthesis of the ligand **L8** requires the preparation of the amine **22** and the functionalized biphenol **23** for a reductive amination. The polyazamacrocycle is synthesized through a modification of the Richman-Atkins procedure as reported in the previous chapters.[41] The bromine salt obtained is treated with a base and subsequently extracted to obtain the free amine for the attachment to the biphenol. In order to obtain the starting **23**, instead, it is necessary to start from [1,1’-biphenyl]-2,2’-diol and protect the OHs with diethylcarbamate (typical DMG group: direct metalation group). This compound is then treated with tetramethylethylenediamine (TMEDA), tert-butyllithium (t-BuLi) and dimethylformamide (DMF) for the directed ortho metalation[66] in order to insert the aldehyde group in ortho position with respect to the OH. The next step involves the formation of the imine **24**, represented without giving importance to the *cis/trans* isomerism of the double bonds as it is immediately reduced as it is. The compound thus obtained is purified by salification obtaining **L8** as hydrochloride, making it perfectly soluble in water.

2.3.2 Photophysical and Potentiometric characterization

The initial analyses carried out on **L8** were aimed to provide information on its spectrophotometric behaviour at different pH values, being perfectly water-soluble (Figure 53). In the UV-Vis range, **L8** has a band at 283 nm at acidic pH which decreases with increasing pH, simultaneously with the appearance of a second band at 312 nm. The latter increases in intensity from pH 3.5 onwards until it reaches its maximum at pH 5 and subsequently remains constant up to basic pH with just a slight bathochromic effect. A clear isosbestic point appears at 284 nm, wavelength that was used to excite the system in the fluorescence studies. There is a big Stokes shift of 124 nm between the excitation wavelength and the emission wavelength, which is found at 408 nm. The fluorescence trend is particularly interesting. The ligand is extremely fluorescent at acid pH, then the emission decreases to a sort of plateau of lesser intensity between pH 5 and 6.5. It is totally quenched at pH 8 and from pH 10 onwards it returns to having a light emission comparable to the initial one.

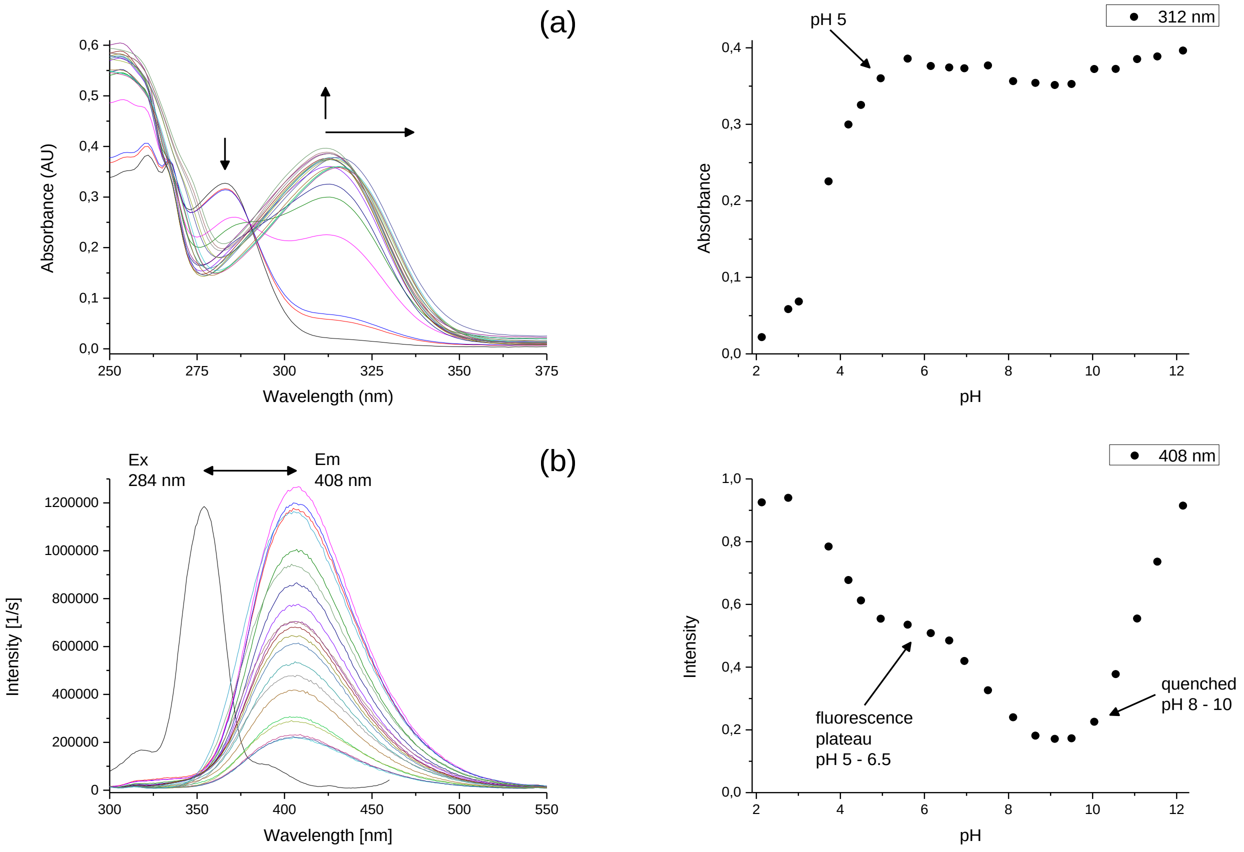

Figure 53. (a) UV-Vis pH titration of **L8** $5x10^{-5}$ M in $NaClO_4$ 0.15 M and its absorbance trend at 312 nm; (b) Fluo pH titration of **L8** $5x10^{-5}$ M in $NaClO_4$ 0.15 M and its normalized fluorescence trend at 408 nm (λ_{exc} = 284 nm).

In order to understand the behaviour of the receptor in solution, a potentiometric titration was performed to detect all the species present in in the whole pH range (see Figure 54). In this way it was possible to derive the actual structure of **L8** in solution: it is a zwitterionic species in which has an intramolecular phenol-phenolate hydrogen bond between the two aromatic rings of the biphenolic spacer and only one of the two benzyl amines protonated. The neutral form of **L8** is obtained in a single step in which the ligand takes two protons at the same time. All the protonation constants were calculated, evaluated and listed in Table 6, they are quite high except for the last one which represents the protonation of the second phenolate. To support the above information, the potentiometric titration was done in parallel with an NMR pH titration by plotting the chemical shift of each single peak at each pH value, obtaining a clear protonation scheme represented in Figure 55. In such a way, not only the structure of **L8** in the neutral form was established, but also those of all the remaining forms shown in Table 6, which will be used, together with molecular dynamics calculations, to explain the fluorescence mechanisms. The first proton to come out from the totally protonated molecule is related to the first deprotonation of the biphenol (obtaining the phenol-phenolate form), so that an extremely stable intramolecular hydrogen bond is formed. The next four deprotonations involve the polyazamacrocycles and only with the sixth deprotonation the first proton of the benzyl amines is lost. The seventh and eighth deprotonation occur simultaneously but it is plausible to think that the last proton lost by the molecule, thus transforming itself into its totally deprotonated form, is the H involved in the intramolecular hydrogen bridge between the two aromatic rings for stability reasons.

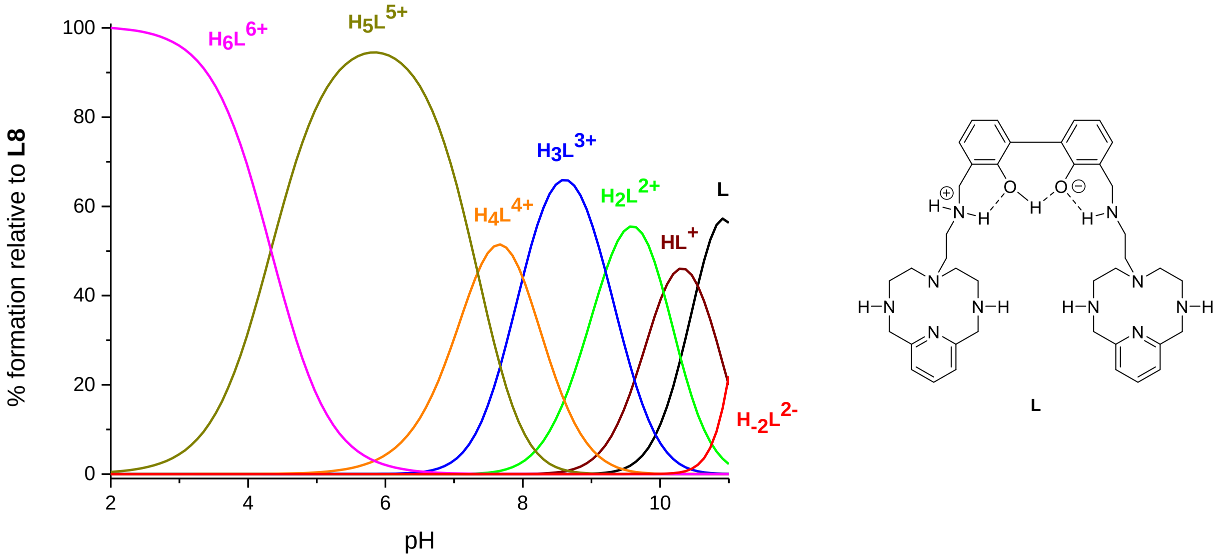

Figure 54. Distribution diagram of the species formed in solution for the system **L8** – [**L8**] = 1x10^{-3} M, NaClO$_4$ 0.15 M, 298.1 K – and the structure of **L8** in solution.

Reaction	**log *K***
$2H^+ + H_{-2}L^{2-} \leftrightarrows L$	22.40(9)
$H^+ + L \leftrightarrows HL^+$	10.55(4)
$H^+ + HL^+ \leftrightarrows H_2L^{2+}$	10.05(3)
$H^+ + H_2L^{2+} \leftrightarrows H_3L^{3+}$	9.20(2)
$H^+ + H_3L^{3+} \leftrightarrows H_4L^{4+}$	8.00(2)
$H^+ + H_4L^{4+} \leftrightarrows H_5L^{5+}$	7.34(2)
$H^+ + H_5L^{5+} \leftrightarrows H_6L^{6+}$	4.33(2)

Table 6. Protonation constant of **L8** determined at 298.1 K in 0.15 M NaClO$_4$.

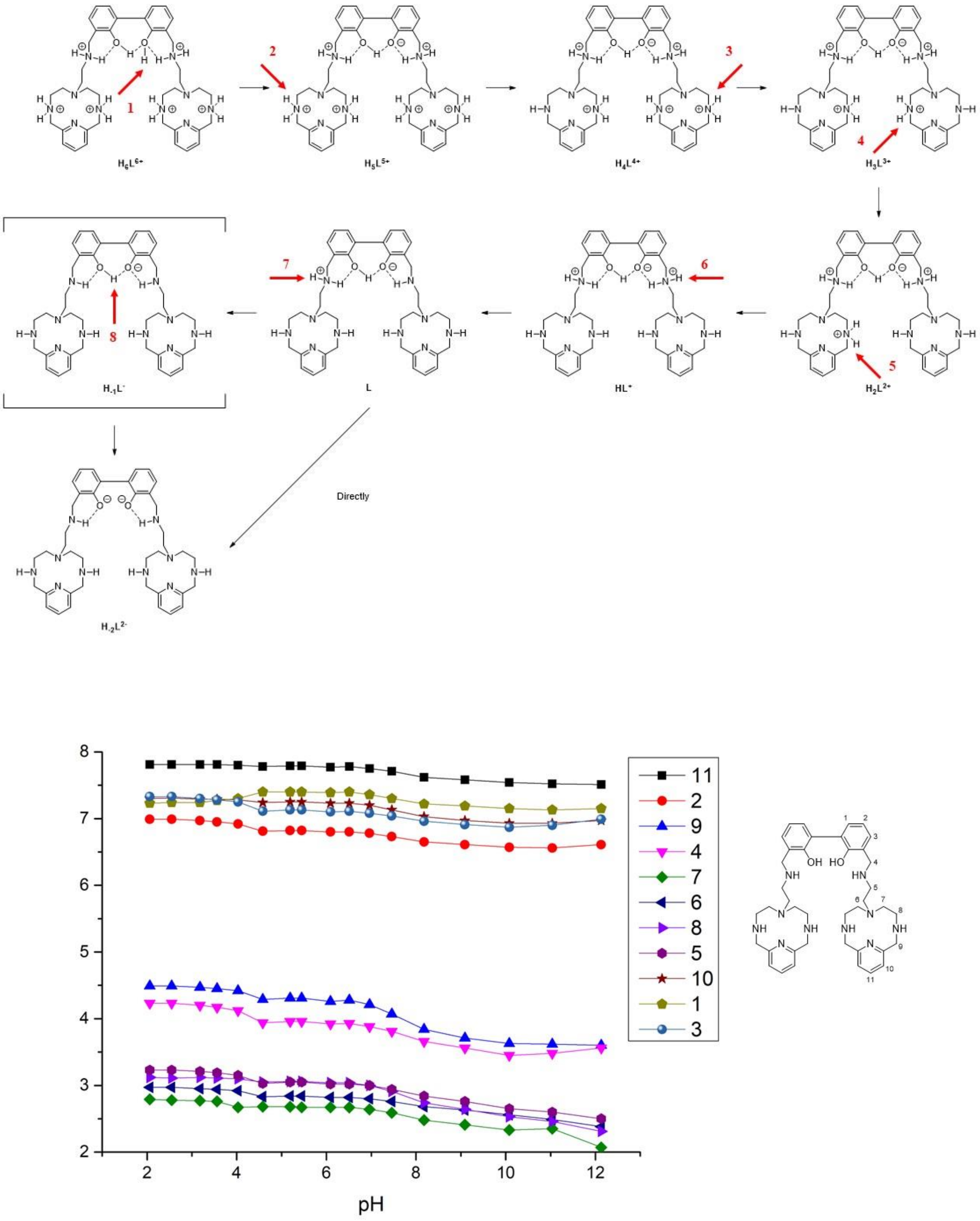

Figure 55. Protonation scheme and NMR pH titration plot of **L8**.

Only once the speciation of **L8** in solution at different pH values is known is it possible to explain the mechanisms of absorption and fluorescence. In order to do that, the distribution diagram of the potentiometric titration is overlapped with the trends of the UV-Vis and Fluo pH titrations (Figure

56). Two main pieces of information can be obtained. As for the absorbance trend, this responds just to the protonation of the biphenol, making it possible to recognize the phenol-phenol and phenol-phenolate forms. It is not possible to find the second deprotonation of the spacer but we know that occurs in the last step. Regarding the fluorescence trend, it is possible to confirm that the most emissive species is the *totally protonated* one, **H_6L^{6+}**, while the emission plateau is given by the species obtained from the first deprotonation of the ligand, **H_5L^{5+}**, and judging by its distribution, the stability of the species is confirmed. It was extremely important to understand that the totally quenched species were those *partially deprotonated* such as **H_3L^{3+}** and **H_2L^{2+}** and that, lastly, the fluorescence increases again returning to be almost maximum with the *totally deprotonated* species **$H_{-2}L^{2-}$**.

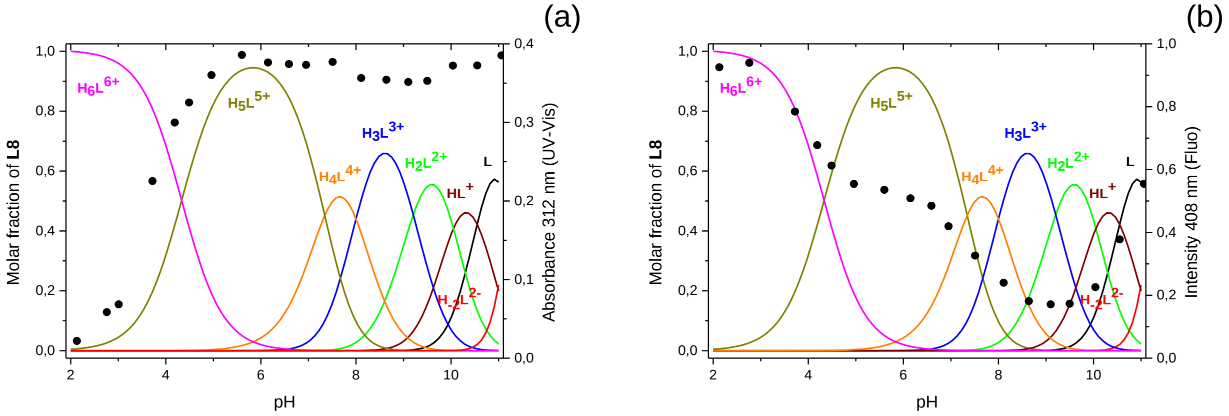

Figure 56. (a) Distribution diagram of the species formed in solution for the system **L8** – [**L8**] = $1x10^{-3}$ M, $NaClO_4$ 0.15 M, 298.1 K – overlaid with UV-Vis pH titration trend at 312 nm of **L8** – $5x10^{-5}$ M in $NaClO_4$ 0.15 M; (b) Distribution diagram of the species formed in solution for the system **L8** – [**L8**] = $1x10^{-3}$ M, $NaClO_4$ 0.15 M, 298.1 K – overlaid with Fluo pH titration trend at 408 nm of **L8** – $5x10^{-5}$ M in $NaClO_4$ 0.15 M – (λ_{exc} = 284 nm).

In order to have an idea of the spatial arrangement of the receptor in its various species and thus to be able to interpret and explain the variations in the fluorescence emission, molecular dynamics calculations were carried out (3 ns calculations, done using AMBER[67] and the GAFF force field – Figure 57). In the *totally protonated* form, $\mathbf{H_6L^{6+}}$, it adopts a closed conformation but with the polyazamacrocycles in opposite sides compared to the biphenol (see Figure 57 (a)), therefore relatively distant from each other. As has already been mentioned, this is a highly fluorescent species and the complete protonation of the ligand, which prevents the PET effect, certainly contributes to this. When it is *partially protonated* the polyazamacrocycles close in over the biphenol both on the same side (e.g. $\mathbf{H_2L^{2+}}$, Figure 57 (b)). Probably the partial protonation state together with the increase in the electronic density on the benzyl amine functions quenches the emission intensity due to a PET mechanism. Furthermore, it is not to be underestimated the increase in the rotational freedom degree of the PH–PH bond that can quench the fluorescence via TICT mechanism.[68] Among the plausible mechanisms of fluorescence quenching, the very close proximity of the two polyazamacrocycles should also be mentioned. That is because, interestingly, in the *totally deprotonated* ligand, $\mathbf{H_{-2}L^{2-}}$, it prefers a fully open, or spread-out, conformation and in this spatial arrangement the two pyridinophane polyamine moieties are placed at the maximum distance from each other (Figure 57 (c)). The latter represents the species in which the ligand returns to being highly fluorescent and is the second case in which the distance, and therefore the lack of interaction, of the two polyamine macrocycles involves an intense emission of light. Last, but not least, it should be remembered that the increase of the electronic density on the phenolic oxygen atoms, given by the deprotonation, enhances the fluorescence emission.[68]

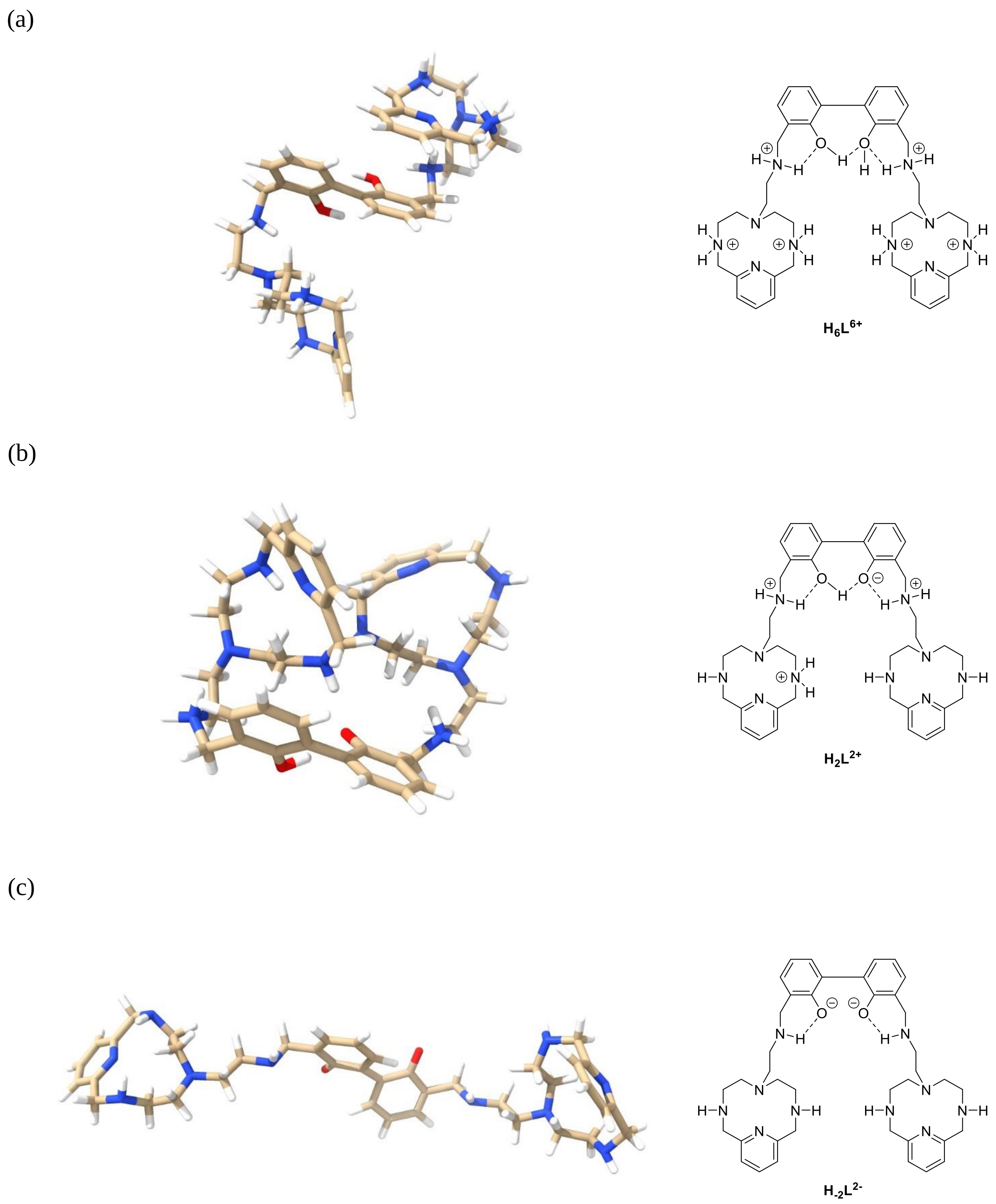

Figure 57. Conformers obtained by molecular dynamics calculations of the *totally protonated* (a), *partially protonated* (b) and *totally deprotonated* (c) species with related structures.

2.3.3 Coordination behaviour with Zn^{2+}

Due to the ability of polycyclic amines, as well as that of biphenol, to complex metal ions, a screening with several divalent cations of transition and post-transition metals for fluorescence variations was performed by adding one and then two equivalents of the guest (see Figure 58). The screening was carried out at pH 6, in order to work in a condition of stable and intermediate fluorescence intensity, using the emission plateau, and in which a single species was present in solution. What surprised was not the ability of Cu^{2+}, Hg^{2+} and Pb^{2+} to totally extinguish the emission of the fluorescence (as paramagnetic/heavy metals), as much as that of Zn^{2+} to quench it like the previous ones, despite it is a metal that is normally responsible for producing a CHEF effect.

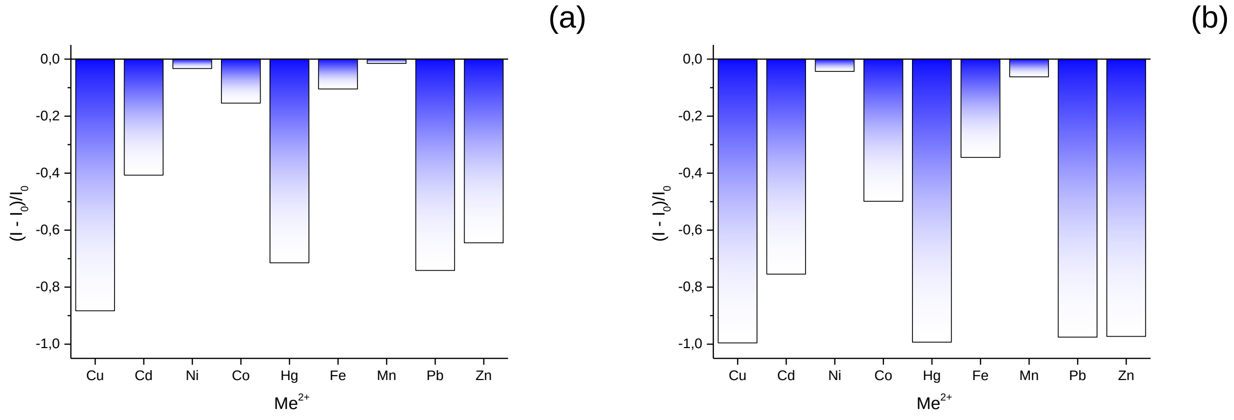

Figure 58. Screening of the emission intensity variation at 408 nm of **L8** $5x10^{-5}$ M by adding 1 equiv. (a) and 2 equiv. (b) of Me^{2+} ion in aqueous solution at pH = 6 (buffer = MES $5x10^{-3}$ M, λ_{exc} = 284 nm).

After this screening, the complexation with Zn^{2+} was studied by potentiometric analysis, both in 1:1 and 1:2 ratio with the ligand. As can be seen from the dispersion diagrams shown in Figure 59, mononuclear species are prevalent with 1 equivalent of Zn^{2+} while binuclear ones with 2 equivalents of Zn^{2+}. The study therefore focused on the latter as they have a preponderant presence of the species $\mathbf{Zn_2H_{-1}L^{3+}}$ which will be useful for understanding the coordination conformation. All the log β values were calculated and listed in Table 7. It is very interesting to see how to eliminate the H bond between the biphenol unit it is necessary not only to use 2 equivalents of Zn^{2+} and also to go to a pH around 8.5, proving the great stability of this intramolecular hydrogen bond.

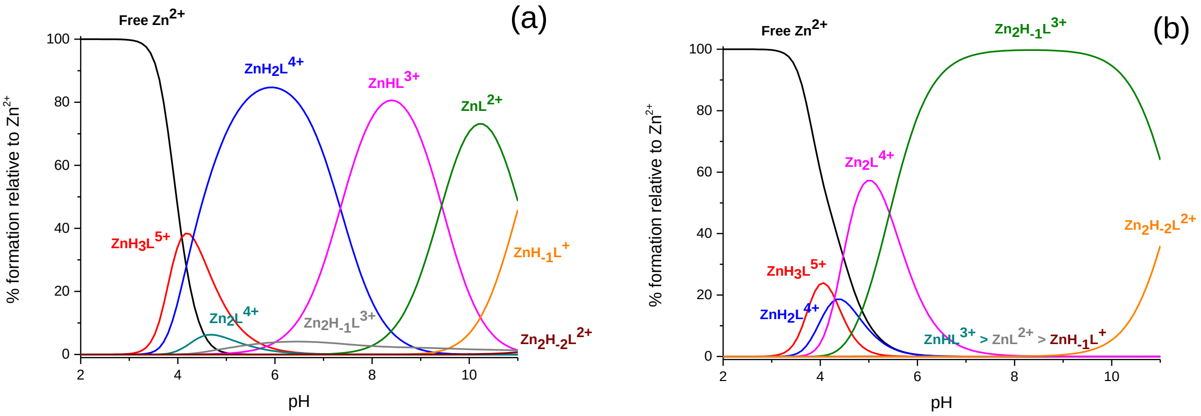

Figure 59. (a) Distribution diagram of the species formed in solution for the system **L8**/Zn^{2+} – [**L8**] = [Zn^{2+}] = $1x10^{-3}$ M, $NaClO_4$ 0.15 M, 298.1 K; (b) Distribution diagram of the species formed in solution for the system **L8**/Zn^{2+} – [**L8**] = $1x10^{-3}$, [Zn^{2+}] = $2x10^{-3}$ M, $NaClO_4$ 0.15 M, 298.1 K.

Reaction	**log *β***
$Zn^{2+} + H_{-2}L^{2-} + H^+ \leftrightarrows ZnH_{-1}L^+$	31.13(2)
$ZnH_{-1}L^+ + H^+ \leftrightarrows ZnL^{2+}$	11.03(3)
$ZnL^{2+} + H^+ \leftrightarrows ZnHL^{3+}$	9.43(9)
$ZnHL^{3+} + H^+ \leftrightarrows ZnH_2L^{4+}$	7.35(1)
$ZnH_2L^{4+} + H^+ \leftrightarrows ZnH_3L^{5+}$	4.31(2)
$2Zn^{2+} + H_{-2}L^{2-} \leftrightarrows Zn_2H_{-2}L^{2+}$	36.45(2)
$Zn_2H_{-2}L^{2+} + H^+ \leftrightarrows Zn_2H_{-1}L^{3+}$	11.25(3)
$Zn_2H_{-1}L^{3+} + H^+ \leftrightarrows Zn_2L^{4+}$	5.42(2)

Table 7. Logarithms of the equilibrium constants in the interaction of Zn^{2+} with **L8** at 298.1 K in 0.15 M $NaClO_4$.

At spectrophotometric level, the same pH titrations were carried out in presence of 2 equivalents of Zn^{2+} (Figure 60). As far as the UV-Vis is concerned, the situation does not change compared to what was observed in the absence of Zn^{2+}, the trend is only more marked. On the other hand, the fluorescence trend is interesting: the anomalous quenching given by Zn^{2+} occurs immediately following the first deprotonation of the biphenol, with the formation of the phenol-phenolate species after pH 3. This phenomenon causes an instant coordination of the Zn^{2+} making impossible to increase the fluorescence emission again.

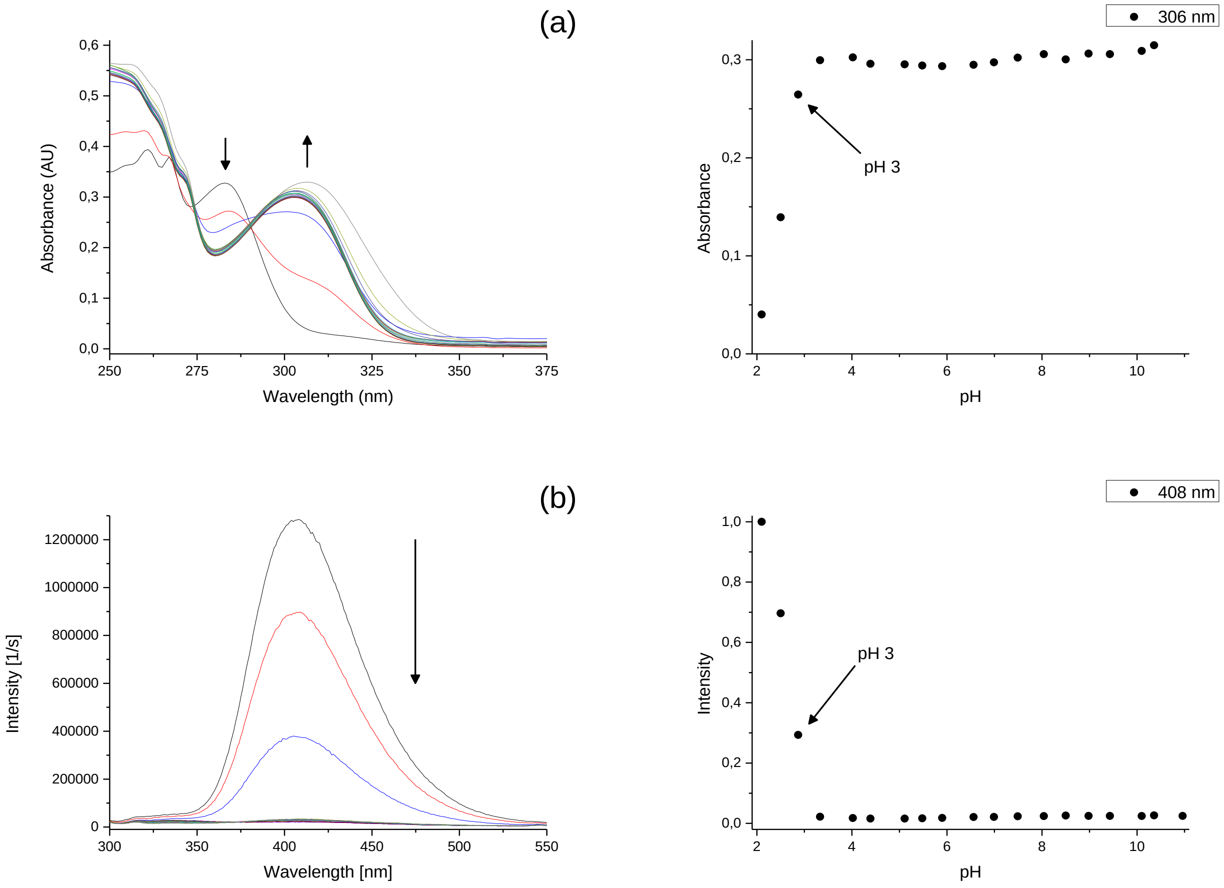

Figure 60. (a) UV-Vis pH titration of **L8** 5x10^{-5} M + 2 eq of Zn^{2+} in NaClO$_4$ 0.15 M and absorbance trend at 306 nm; (b) Fluo pH titration of **L8** 5x10^{-5} M + 2 eq of Zn^{2+} in NaClO$_4$ 0.15 M and fluorescence trend at 408 nm (λ_{exc} = 284 nm).

The previous trends were used with the purpose of overlapping them with the distribution diagrams of the species formed in solution for the system **L8**/Zn^{2+} (see Figure 61) and then find suitable strategies for the characterization of the dinuclear complexes. Among these, it was decided to titrate the ligand with Zn^{2+} at pH 6, taking advantage of the stable fluorescence given by the plateau with the presence of a single species in solution and to study the trend of its decrease as well as the trend of formation of the complexes. At the same time, a mono and bidimensional NMR characterization of the receptor metal-coordinated at pH 7.4 was carried out in order to interpret the geometry and three-dimensional conformation of the coordination with the guest. The use of this physiological pH would allows to understand the speciation of the ligand and to place us in a condition (with 2 equivalents of Zn^{2+}) in which there is only a single complex to study and interpret.

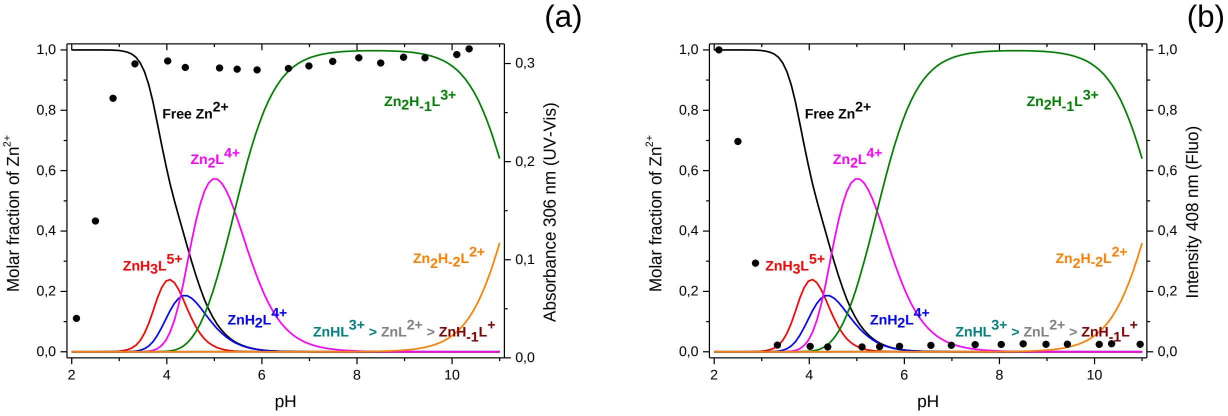

Figure 61. (a) Distribution diagram of the species formed in solution for the system **L8**/Zn^{2+} – [**L8**] = $1x10^{-3}$, [Zn^{2+}] = $2x10^{-3}$ M, $NaClO_4$ 0.15 M, 298.1 K – overlaid with UV-Vis pH titration trend at 306 nm of **L8** + 2 eq of Zn^{2+} – $5x10^{-5}$ M in $NaClO_4$ 0.15 M; (b) Distribution diagram of the species formed in solution for the system **L8**/Zn^{2+} – [**L8**] = $1x10^{-3}$, [Zn^{2+}] = $2x10^{-3}$ M, $NaClO_4$ 0.15 M, 298.1 K – overlaid with Fluo pH titration trend at 408 nm of **L8** + 2 eq of Zn^{2+} – $5x10^{-5}$ M in $NaClO_4$ 0.15 M – (λ_{exc} = 284 nm).

The fluorescence titration at pH 6 with increasing amounts of Zn^{2+} reported in Figure 62 shows how the light emission decreases linearly with the concentration of the added guest, up to completely extinguishing already with only 1 equivalent of the metal. The progress of the light emission trend from 1 to 2 equivalents is practically asymptotic and there is no possibility of re-ignition of the fluorescence. More information can be obtained from UV-Vis titration at pH 6 with increasing amounts of Zn^{2+}, see Figure 63. In fact, two different isosbestic points and two trends with different slopes are easily distinguishable, confirming the existence of two distinct species in solution:

plausibly $\mathbf{ZnH_2L^{4+}}$ for 1:1 ratio **L8**/Zn^{2+} and $\mathbf{Zn_2H_{-1}L^{3+}}$ for ratio 1:2 **L8**/Zn^{2+}. Since both complexes have no fluorescence at all, they may likely share the coordination conformation.

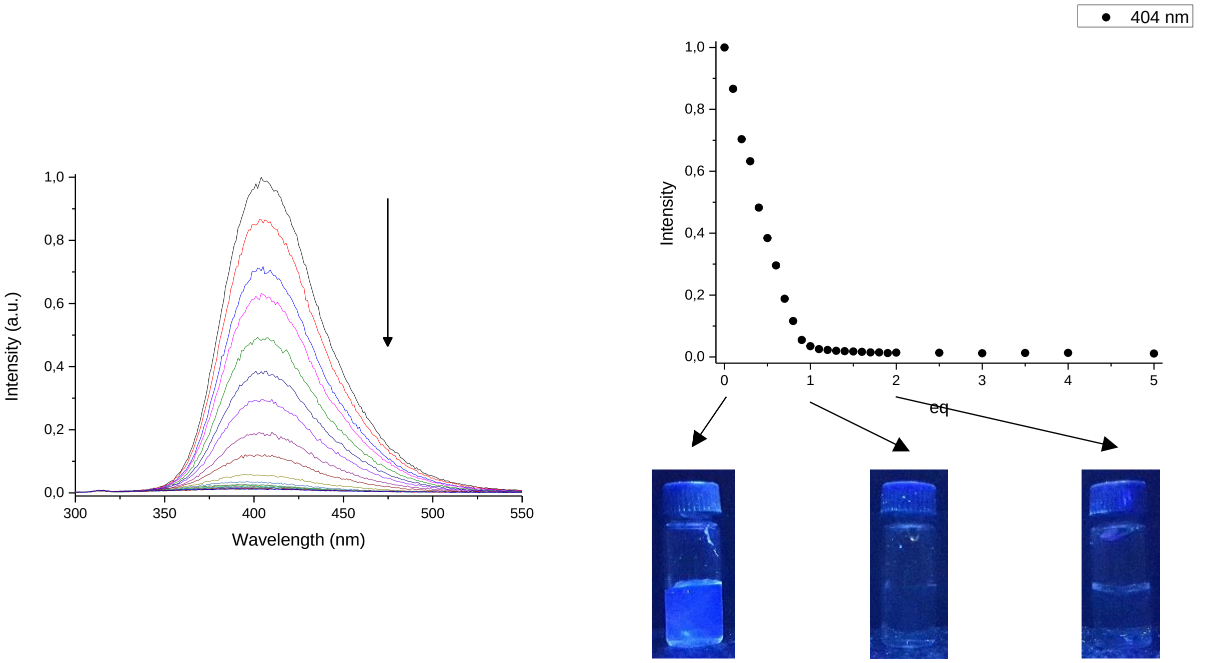

L8 **L8** + 1 eq Zn^{2+} **L8** + 2 eq Zn^{2+}

Figure 62. Fluo titration in aqueous solution at pH 6 (buffer = MES $5x10^{-3}$ M, λ_{exc} = 284 nm) of **L8** $5x10^{-5}$ M + increasing amount of Zn^{2+} and fluorescence trend at 404 nm.

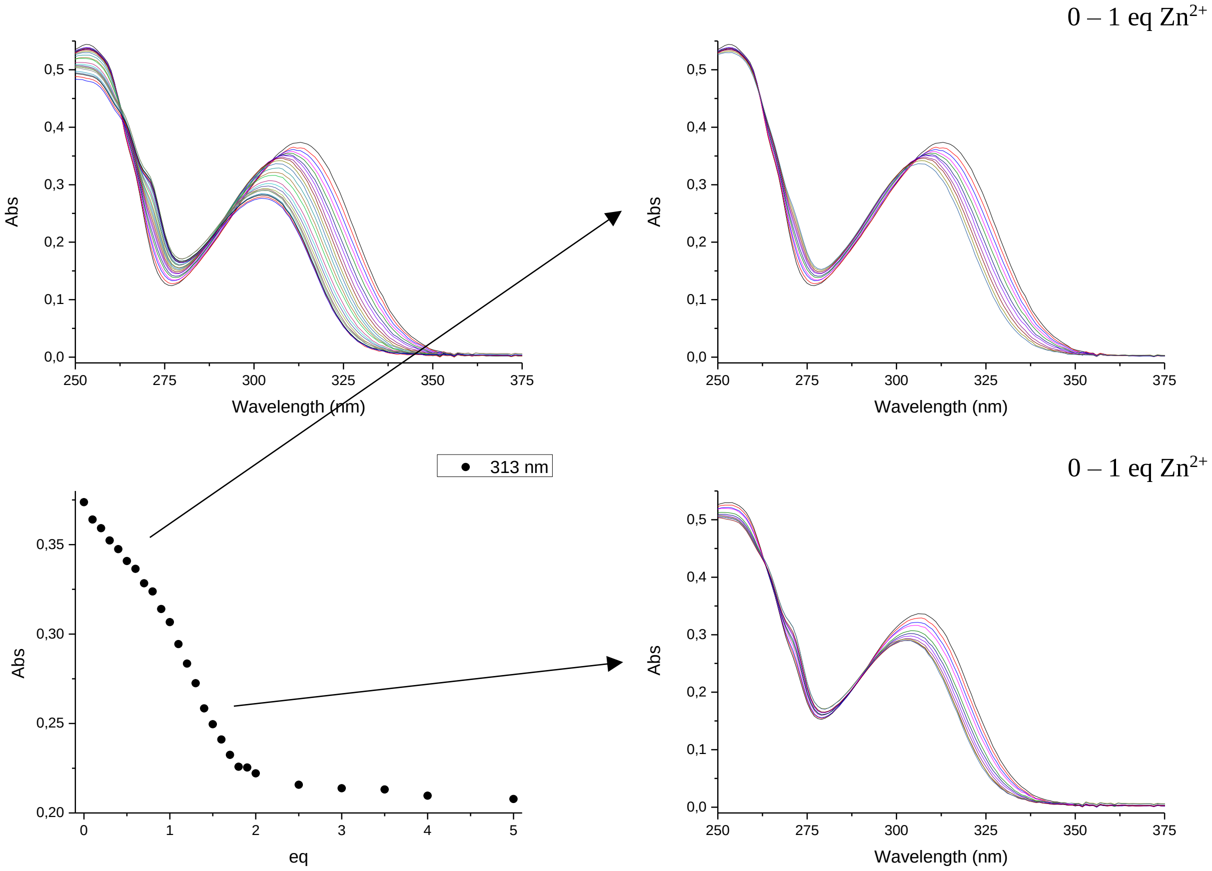

Figure 63. UV-Vis titration in aqueous solution at pH 6 (buffer = MES $5x10^{-3}$ M) of **L8** $5x10^{-5}$ M + increasing amount of Zn^{2+} and absorbance trend at 313 nm.

Mono and bidimensional NMR characterizations have been found to be fundamental for understanding the coordination mechanism. The one-dimensional NMR tests with Zn^{2+} were carried out as follows: a solution of the ligand at pH 7.4 was prepared and 1 equivalent and then 2 equivalents of metal were subsequently added. After each addition the pH was brought back to 7.4 with KOD. As can be seen from the ^{1}H-NMR reported in Figure 64, **L8** as itself is perfectly clean and understandable even at customized pH (probably the viewed species is **H_4L^{4+}**). As soon as the first equivalent of Zn^{2+} is added, and the pH is brought back to 7.4, the ^{1}H-NMR becomes incomprehensible, not amenable to analysis. The most logical explanation to that is the presence of a *mixture of mononuclear species* for the slowly interchange on the NMR time scale (probably in the forms **ZnH$_2$L^{4+}** and **ZnHL^{3+}**). With the addition of the second equivalent of the metal, for a total of 2 equivalents, the ^{1}H-NMR becomes clear and understandable again. What can be seen is the presence of *only 1 binuclear species* on the NMR time scale, the form under investigation **Zn$_2$H$_{-1}$L^{3+}**. It is possible to obtain a further information from this last test by focusing on the aromatic area. **L8** possesses 12 aromatic protons and in the species **L8** + 2 eq Zn^{2+} there are 6 signals that integrate each one for 2 protons. That suggests that an element of symmetry must be present in the coordination of this binuclear species.

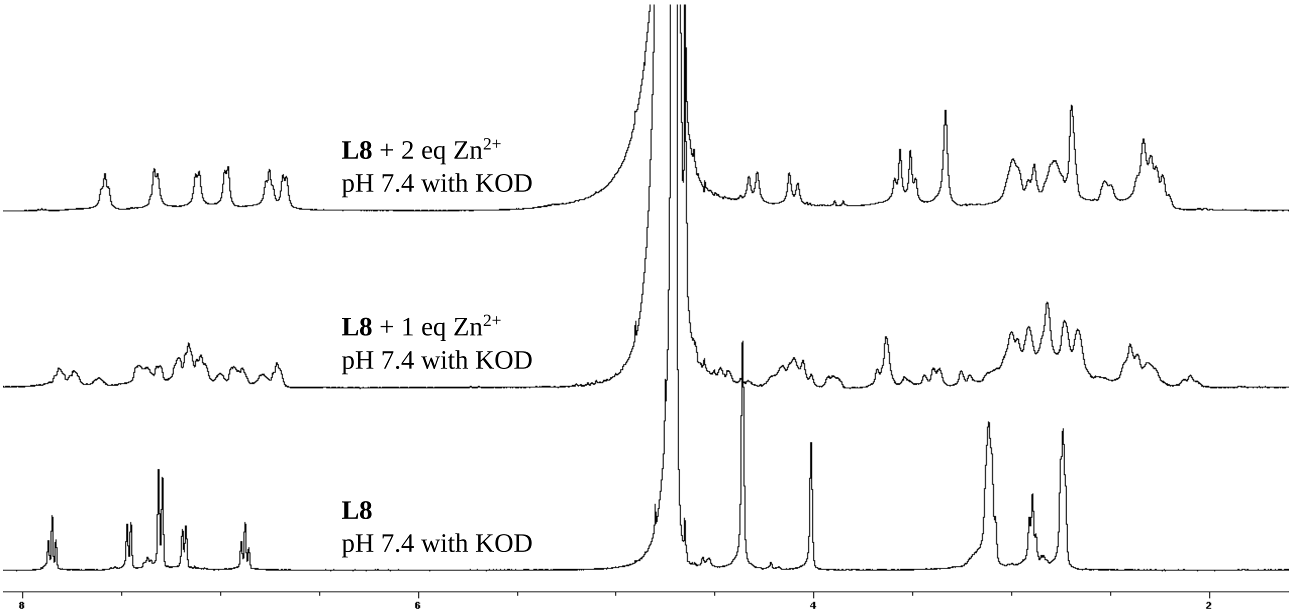

Figure 64. Monodimensional NMR tests with Zn^{2+} at fixed pH 7.4.

To obtain this symmetry and consequently the structure of the host-guest binuclear complex, a correlation spectroscopy (COSY, Figure 65) was performed. From the COSY of the complex with 2 equivalents of Zn^{2+} it is possible to see the coupling between the aromatic protons. Two signal patterns can be found, both formed by one triplet that couples with two doublets: one pattern is attributable to the pyridine moieties and the other to the biphenolic spacer. In order to assign the signals to a specific system, a second bidimensional analysis is required, i.e. the two-dimensional NOE Spectroscopy (NOESY, Figure 66) experiment. From the NOESY it is visible that two of the doublets that couple with the same triplet, therefore belonging to the same system, are spatially close. It is to be excluded that these are the two different biphenol doublets as, in any conformation, they would be too far apart to couple with each other. These are the protons **A** and **B** of the two pyridines that are arranged face to face losing their symmetry but preserving the symmetry of the biphenol and of the entire ligand, respecting all the behaviours observed previously.

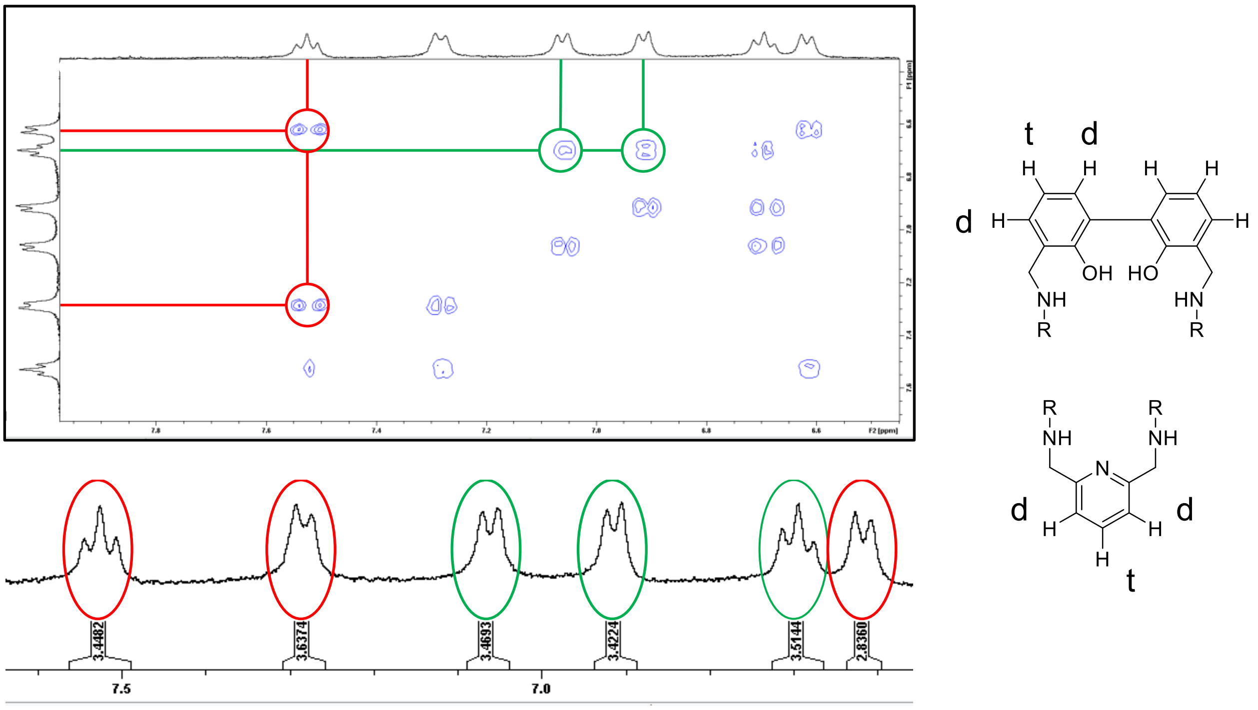

Figure 65. Bidimensional NMR – COSY – of **L8** with 2 equivalents of Zn^{2+} at fixed pH 7.4 and relative aromatic signal patterns.

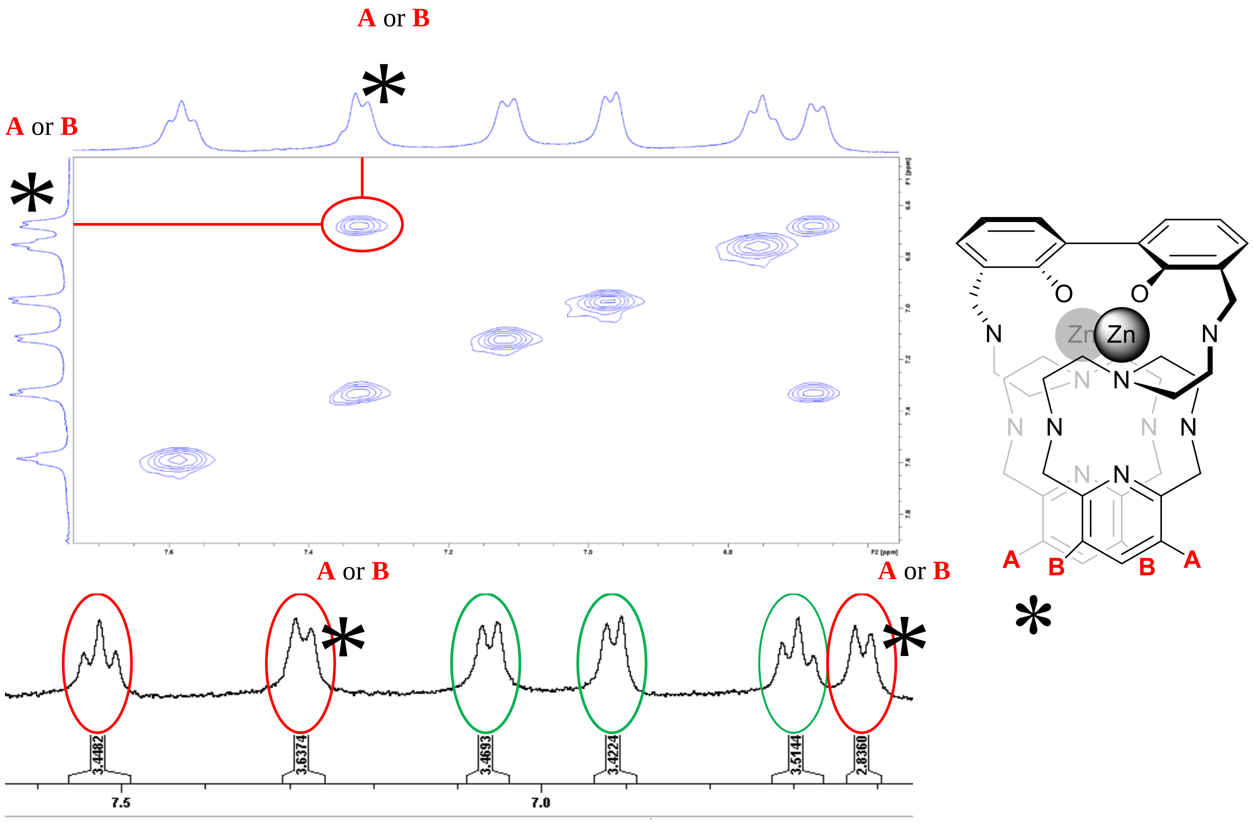

Figure 66. Bidimensional NMR – NOESY – of **L8** with 2 equivalents of Zn^{2+} (aromatic area) at fixed pH 7.4 and obtained coordination structure.

2.3.4 Solid-state studies

Given the great difficulty in obtaining crystals of **L8** as its hexachlorohydrate, the ligand was converted into the free amine by treatment with a concentrated base and subsequent extraction with organic solvent. The free salt receptor was thus dissolved in MeOH and subsequently an excess of $Zn(ClO_4)_2$ (about 10 equivalents) in solid form was added. The suspension was treated with a few drops of distilled water, sonication and moderate heat to obtain a clear solution. To promote the crystallization, $NaClO_4$ was added as a counter ion and the solution was finally concentrated very slowly, by evaporation of the solvent, at room temperature.

The crystals were not obtained as a single crystal but as highly geminated (Figure 67). In the solid state the structure is relatively different from that deduced from bidimensional NMR studies. The Zn^{2+} is hexacoordinated inside the macrocycle through the 4 N from which it is composed, the N of the branching and the phenolic O; the coordination ratio **L8**/Zn^{2+} is 1:2. The two phenols are not coplanar but staggered, the aliphatic chains and the OH group, although branching on the same side, are at a comparable height but at a greater distance from the face-to-face proximity deduced from the bidimensional NMR studies due to the Zn^{2+}coordination; for the same reason the two pyridines are on opposite sides. This crystalline structure, as well as this closer proximity between the pyridine and the biphenol, would justify the spatial interaction between the benzyl protons singlet **C** (integration = 4H) and one of the two pyridine benzyl protons series **D** and **E** (integration = 1H for each doublet, diastereotopic protons), see Figure 67.

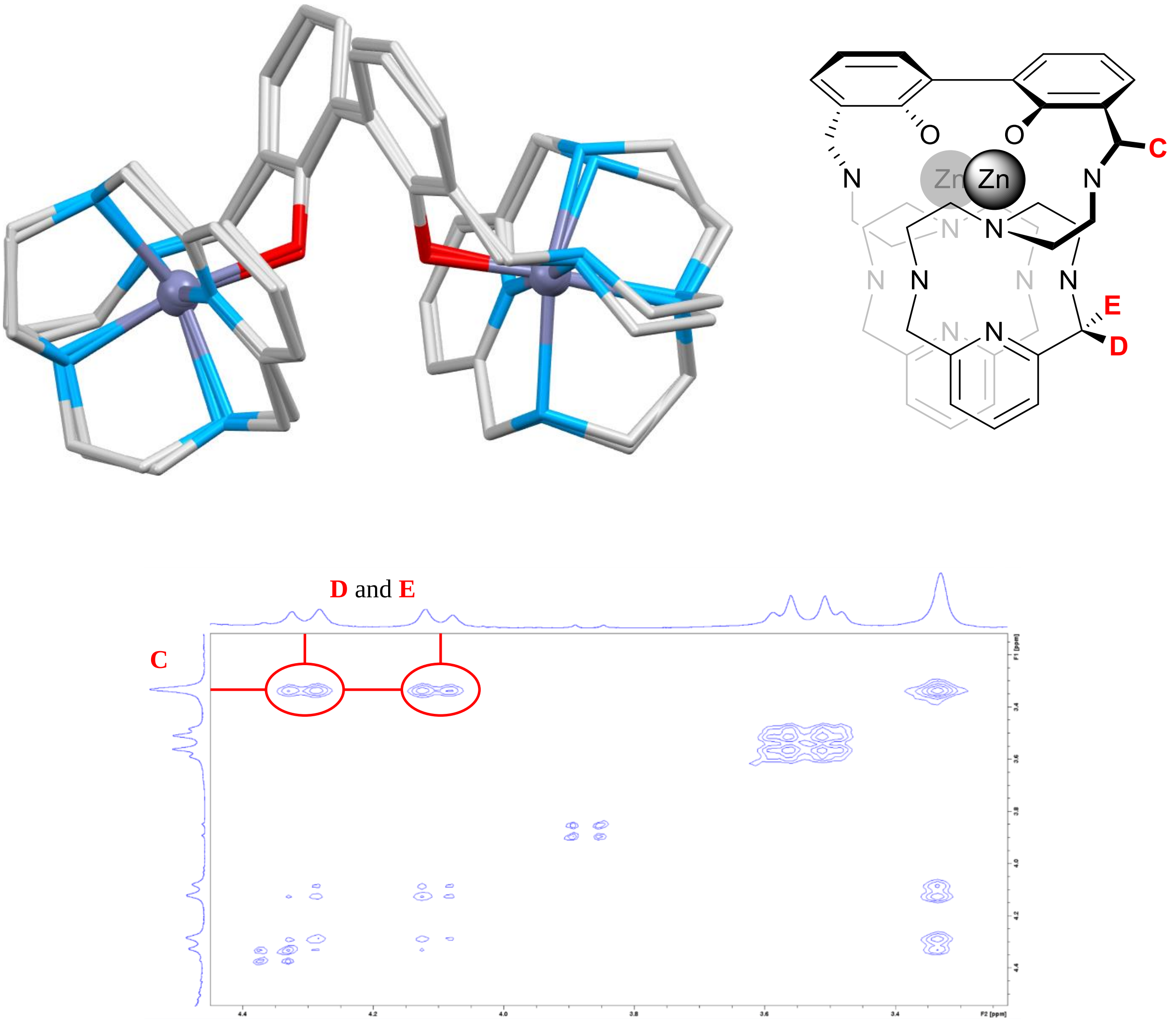

Figure 67. Structure of **L8** hexacoordinate with Zn^{2+}obtained by X-ray crystallography, coordination structure obtained from NMR studies and bidimensional NMR – NOESY – of **L8** with 2 equivalents of Zn^{2+} (aliphatic area) at fixed pH 7.4.

2.3.5 Conclusions

The receptor **L8** turned out to be highly coordinating towards Zn^{2+} showing a particular fluorescence behaviour, switching-OFF the emission of light in the presence of this metal. It has been demonstrated that the proximity of the two polyamine macrocycles is actually responsible for the fluorescence quenching. The non-fluorescent structure deduced by the NMR tests is the same obtained with molecular dynamics calculations in absence of Zn^{2+}. The role of the bound Zn^{2+} is therefore to bring the two polyazamacrocycles moieties face to face giving as result the non-fluorescent structure. It has also been demonstrated that, at pH 6, only 1 equivalent of Zn^{2+} is sufficient to have a total turn-OFF of the fluorescence, proving how the receptor-metal coordination is strong and that apparently only 1 equivalent is enough to move the two pyridinophane polyamine units facing each other. In the solid state the situation presents slight differences with respect to what has been observed in solution. The two polyazamacrocycles are further away from each other but always on the same level. Pyridine is located spatially closer to biphenol and we have reason to believe that the real cause of the quenching is the deactivation by the pyridine as it is almost π-stacked with the aromatic spacer. For obvious reasons the results in solution are slightly different from those in the solid state. The real condition of **L8** with 2 equivalents of Zn^{2+} in solution is certainly a state of close proximity between the two macrocycles, allowing mutual coupling, with simultaneous π-stacking between pyridine and biphenol.

2.3.6 Interaction with biological molecules

Due to the attendance of multiple hydrogen bond donors such as amines and hydroxyl, **L8** was tested not only with metals but also in the presence of biological molecules. Potentiometric, UV-Vis and fluorescence titrations were performed to analyse the interaction of **L8** with the selected targets: two amino acids, L-aspartic (Asp) and L-glutamic (Glu), and the corresponding dicarboxylic acid counterparts, succinic (Suc) and glutaric (Glt) acid. The reason for this choice lies in studying how the different length of the carbon chain (2 or 3 C atoms) and the presence, or absence, of a primary amine can influence the nature and the type of the interaction.

From the equilibrium constants shown in Table 8 and calculated for the **L8**+amino acid/dicarboxylic acid systems, by specifically comparing the Glu/Asp and the Suc/Glt pairs, it is possible to appreciate a little discrimination in the recognition of L-aspartic acid on L-glutamic acid and of succinic acid on glutaric acid, respectively. In the first case, this selectivity for Asp towards Glu can be found at basic pH, where the calculation of the equilibrium constants is possible only for the Asp and all the species have a low protonation degree. In the second case, this selectivity occurs at acid pH, where all the species have a high protonation degree and the Glt constants are always higher than those of the Suc. All this is shown in the distribution diagrams relating to the potentiometric titrations of **L8** with the four different biological molecules (see Figure 68). In fact, it is possible to observe how in the specific case of L-aspartic acid there is a higher concentration of complex species at basic pH compared to its dicarboxylic counterpart succinic acid. On the other hand, while the lengthening of one carbon atom in the chain of the amino acid target – obtaining the L-glutamic acid – does not favour its complexation (or rather it makes it less effective), in the case of the dicarboxylic equivalent glutaric acid there is a high interaction at acidic pH.

	Asp	**Glu**	**Suc**	**Glt**
Reaction[a]			**log *β***	
$L + X + 2H \leftrightarrows H_2XL$	26.66(1)			
$L + X + 3H \leftrightarrows H_3XL$	37.02(1)		36.00(3)	36.39(3)
$L + X + 4H \leftrightarrows H_4XL$	47.32(1)		46.04(2)	46.46(2)
$L + X + 5H \leftrightarrows H_5XL$	56.79(1)	55.39(3)	55.29(2)	55.97(2)
$L + X + 6H \leftrightarrows H_6XL$	65.80(1)	64.79(1)	63.11(4)	64.02(2)
$L + X + 7H \leftrightarrows H_7XL$	73.67(1)	72.81(2)	70.59(2)	71.65(2)
$L + X + 8H \leftrightarrows H_8XL$	80.83(1)	80.29(2)	76.13(1)	77.27(2)
$L + X + 9H \leftrightarrows H_9XL$	84.87(1)	84.97(2)	80.42(2)	81.60(2)
$L + X + 10H \leftrightarrows H_{10}XL$		88.47(3)		85.62(2)

[a] Charges omitted

Table 8. Logarithms of the cumulative equilibrium constants in the interaction of L-aspartic, L-glutamic, succinic and glutaric acid with **L8** at 298.1 K in 0.15 M $NaClO_4$.

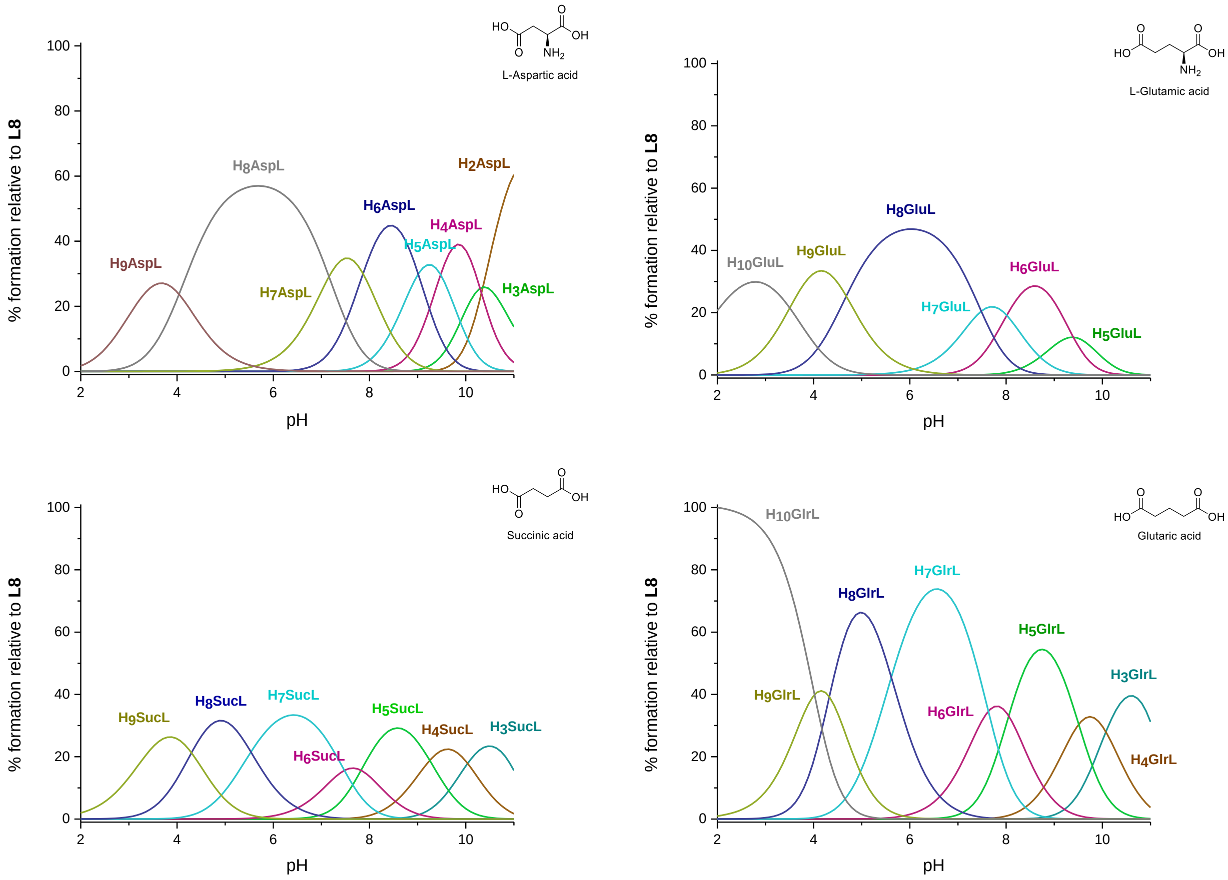

Figure 68. Distribution diagram of the species formed in solution for the system **L8**/Asp, **L8**/Glu, **L8**/Suc and **L8**/Glr. [**L8**] = [Asp] = [Glu] = [Suc] = [Glr] = 1x10^{-3} M, $NaClO_4$ 0.15 M, 298.1 K.

Similarly to the study of coordination with Zn^{2+} we relied on molecular dynamics calculations to search for data in favour of the reported evidence. Unlike the previous case, we found some differences: the DFT calculations report a theoretical greater affinity of **L8** for L-glutamic acid compared to L-aspartic acid. This difference had never been found until now as DFT calculations have always shown to be consistent with the scientific evidence. We then thought of a possible misinterpretation of the equilibrium constants and of the distribution diagrams. In effect in the present case these diagrams do not furnish much help to our purpose since they are rather intricate owing to the concomitant formation of many species none of which are clearly prevalent. Therefore, in order to obtain a graphic representation that allow a simple visual analysis of the speciation and the selectivity we resorted to the *cumulative species distribution diagram*.[69] While Figure 68 represents the concentration curves for the individual species, Figure 69 reports the overall amounts of the organic molecules bound to **L8**. Percentages are calculated with respect to the analytical concentration of **L8**. A clearer picture is obtained by adopting the representation of the *cumulative species distribution diagram* shown in Figure 69. Since thermodynamic selectivity is the preferential binding of one species over another under equivalent conditions, we can neglect the formation of individual species and instead consider the overall amounts of organic molecules bound to **L8** as a function of pH. In this way the intricate species distribution diagram shown in Figure 68 can be transformed into the simple one shown in Figure 69, which clearly establishes the complicated pattern of selectivity occurring in the system. As is possible to see, as regards the two amino acids Asp and Glu, a marked difference in the percentage distribution can be noted from pH 8 upwards, which becomes quantitative at pH 11. The species $\mathbf{LAspH_x}$ has indeed a percentage distribution equal to 70% while $\mathbf{LGluH_x}$ is only 5%. Dicarboxylic acids, on the other hand, behave in the opposite way: selectivity is found at acid pH where the $\mathbf{LGlrH_x}$ species is 90% and $\mathbf{LSucH_x}$ at 5%. Their difference in percentage distribution is always quite distinct throughout the pH range but becomes quantitative from pH 6 to pH 2.

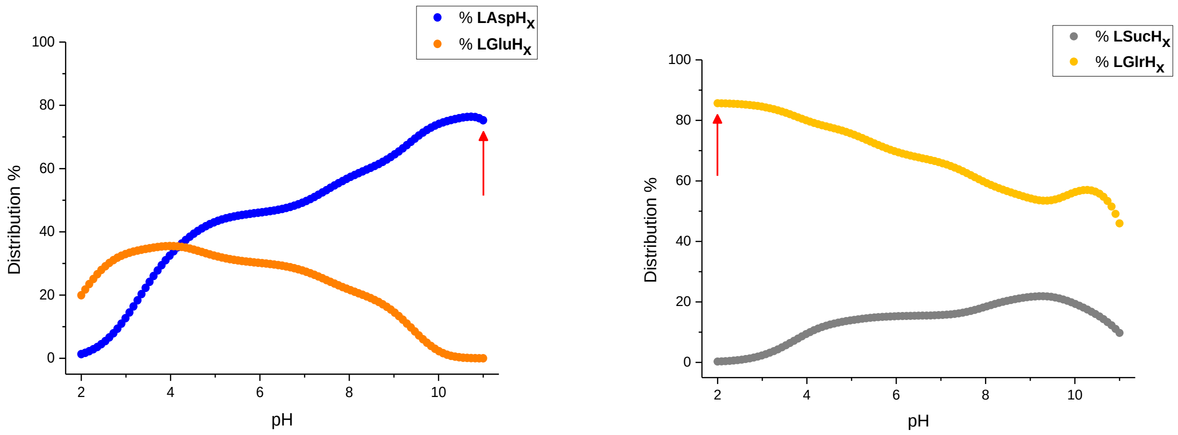

$$\text{Distribution \% of } \mathbf{LXH_n} = \frac{\Sigma[\mathbf{LXH_n}] * 100}{[\mathbf{L8}]}$$

$$\Sigma[\mathbf{LXH_n}] = [\mathbf{LXH_1}] + [\mathbf{LXH_2}] + [\mathbf{LXH_3}] + \cdots$$

Figure 69. *Cumulative species distribution diagram*, in order to see the most present species in solution.

The same data processing can be transferred to the cumulative equilibrium constants thus obtaining the *cumulative equilibrium constants diagram* (Figure 70).[69] If the cumulative equilibrium constants are known and the total analytical concentrations of the independent reactants **L8**, Asp, Glu, Suc and Glt are fixed, the concentration of all species present in solution can be calculated by solving the set of mass balance equations, which furnishes the free reagent concentrations [$\mathbf{LXH_n}$], [$\mathbf{XH_n}$] and [$\mathbf{LH_n}$]. In the *log K_{app} (apparent constant) diagram* the higher is the value, the greater is the selectivity. The trends follow the *distribution % curves*: the log K_{app} of Asp is about 4 at pH 11 while that of Glu is close to 0 at the same pH; on the contrary at pH 2 the Suc and the Glr have a log K_{app} around 4.5 and 1 respectively. The differences of 4 and 3.5 orders of magnitude, confirms that this ligand can selectively recognize L-aspartic acid and glutaric acid at basic and acidic pH respectively.

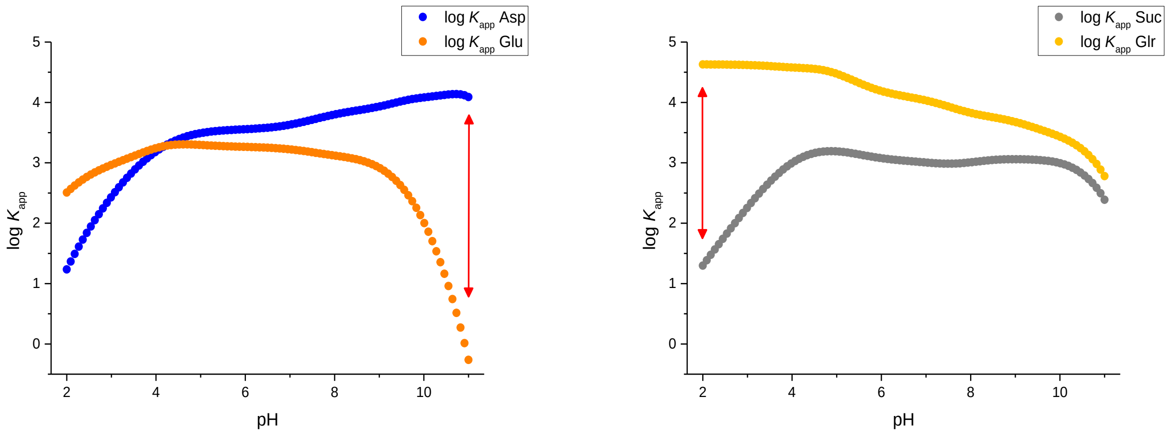

$$\log K_{\mathrm{app}} = \log_{10}(K_{\mathrm{app}})$$

$$K_{\mathrm{app}} = \frac{\Sigma[\mathbf{LXH_n}]}{\Sigma[\mathbf{XH_n}] * \Sigma[\mathbf{LH_n}]}$$

$$\Sigma[\mathbf{LXH_n}] = [\mathbf{LXH_1}] + [\mathbf{LXH_2}] + [\mathbf{LXH_3}] + \cdots$$

$$\Sigma[\mathbf{XH_n}] = [\mathbf{XH_1}] + [\mathbf{XH_2}] + [\mathbf{XH_3}] + \cdots$$

$$\Sigma[\mathbf{LH_n}] = [\mathbf{LH_1}] + [\mathbf{LH_2}] + [\mathbf{LH_3}] + \cdots$$

Figure 70. *Logarithm of apparent constants* diagram in order to see the selectivity of the ligand for one of the two species by referring to the log K_{app}.

The same data processing system followed for **L8**/Zn^{2+} has been transposed to the interaction with the two biomolecules. Given the discriminating power of **L8** against L-aspartic acid and glutaric acid, at their respective pHs, these two targets were selected for the spectroscopic measurements. Through UV-Vis and Fluo pH-metric titrations we searched for possible variations in the optical behaviour of the ligand in presence of one equivalent of Asp and Glr in the previous ionic strength. The trends of the pH titrations in the UV-Visible and fluorescence data (superimposed with the respective potentiometric distribution diagrams, Figure 71-72) do not show appreciable variations in the presence of the two biomolecules compared to that of **L8** alone.

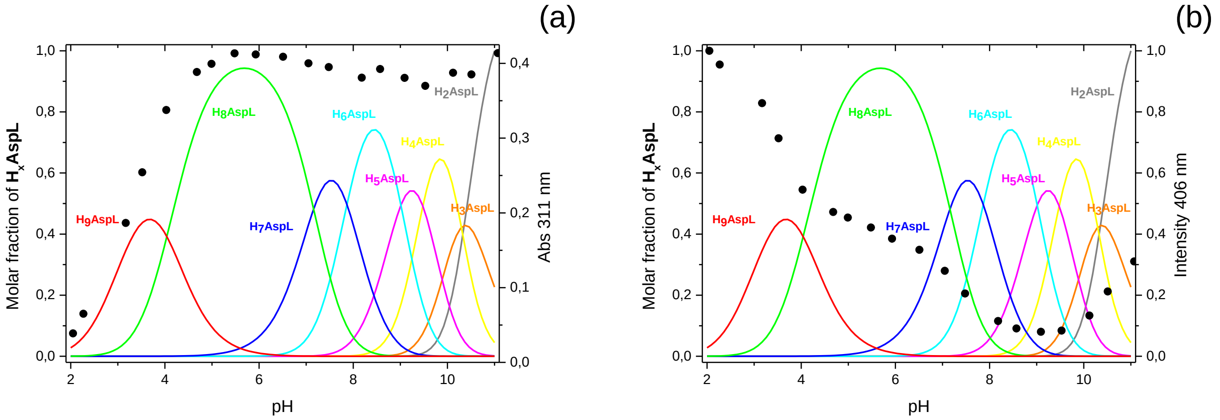

Figure 71. (a) Distribution diagram of the species formed in solution for the system **L8**/Asp – [**L8**] = [Asp] = 1x10^{-3} M, $NaClO_4$ 0.15 M, 298.1 K – overlaid with UV-Vis pH titration trend at 311 nm of **L8** + 1 eq of Asp – 5x10^{-5} M in $NaClO_4$ 0.15 M; (b) Distribution diagram of the species formed in solution for the system **L8**/Asp – [**L8**] = [Asp] = 1x10^{-3} M, $NaClO_4$ 0.15 M, 298.1 K – overlaid with Fluo pH titration trend at 406 nm of **L8** + 1 eq of Asp – 5x10^{-5} M in $NaClO_4$ 0.15 M – (λ_{exc} = 284 nm).

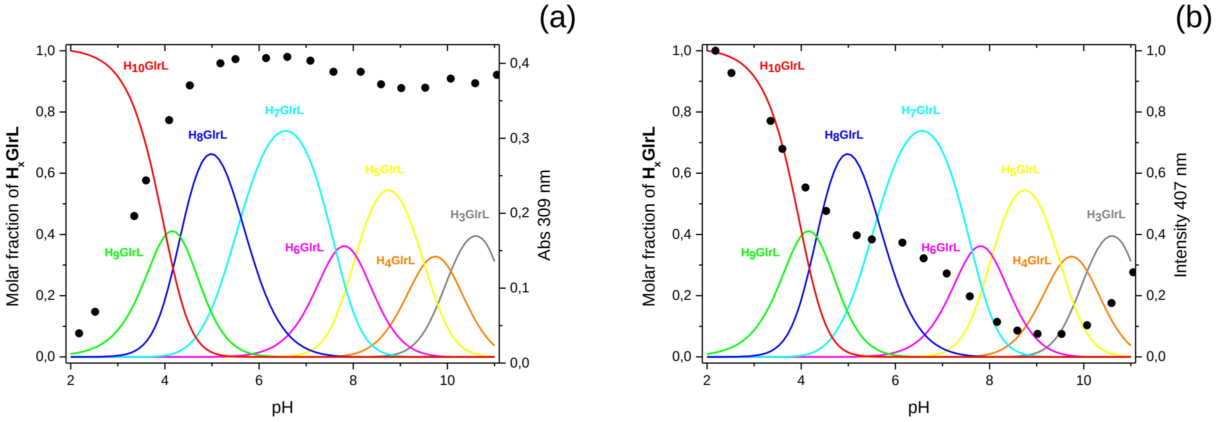

Figure 72. (a) Distribution diagram of the species formed in solution for the system **L8**/Glr – [**L8**] = [Glr] = 1x10^{-3} M, $NaClO_4$ 0.15 M, 298.1 K – overlaid with UV-Vis pH titration trend at 309 nm of **L8** + 1 eq of Glr – 5x10^{-5} M in $NaClO_4$ 0.15 M; (b) Distribution diagram of the species formed in solution for the system **L8**/ Glr – [**L8**] = [Glr] = 1x10^{-3} M, $NaClO_4$ 0.15 M, 298.1 K – overlaid with

Fluo pH titration trend at 407 nm of **L8** + 1 eq of Glr – 5x10^{-5} M in $NaClO_4$ 0.15 M – (λ_{exc} = 284 nm).

Having focused this work on the peculiar emission of **L8**, we performed a last mathematical operation to compare the receptor's own fluorescence with that in the presence of one equivalent of Asp and Glr. The fluorescence trends of **L8**, **L8** + 1 eq of Asp and **L8** + 1 eq of Glr were normalized to the starting point of each titration – pH approximately 2 – and superimposed on a single worksheet in a 3Ys plot. As already stated, also from this 3Y graph reported in Figure 73 it can be seen how the emission trends follow the same progression of the own fluorescence of **L8** alone. As a comment is it possible to see that the emission of **L8** + 1 eq or Asp is perfectly superimposable with that of **L8** + 1 eq of Glr and that the two curves are only shifted downwards by the same amount compared with the fluorescence of **L8**. The starting emission value was made equal for the three analyses, but it is curious how the presence of the two biomolecules makes the low fluorescence of **L8** between pH 8 and 10 even lower. Another difference concerns the reacquisition of the emission: while **L8** alone in its *totally deprotonated form* (pH > 11) returns to being as fluorescent as at pH 2 – *totally protonated species* – the presence of the two biological molecules allows only a half restoration of the emission.

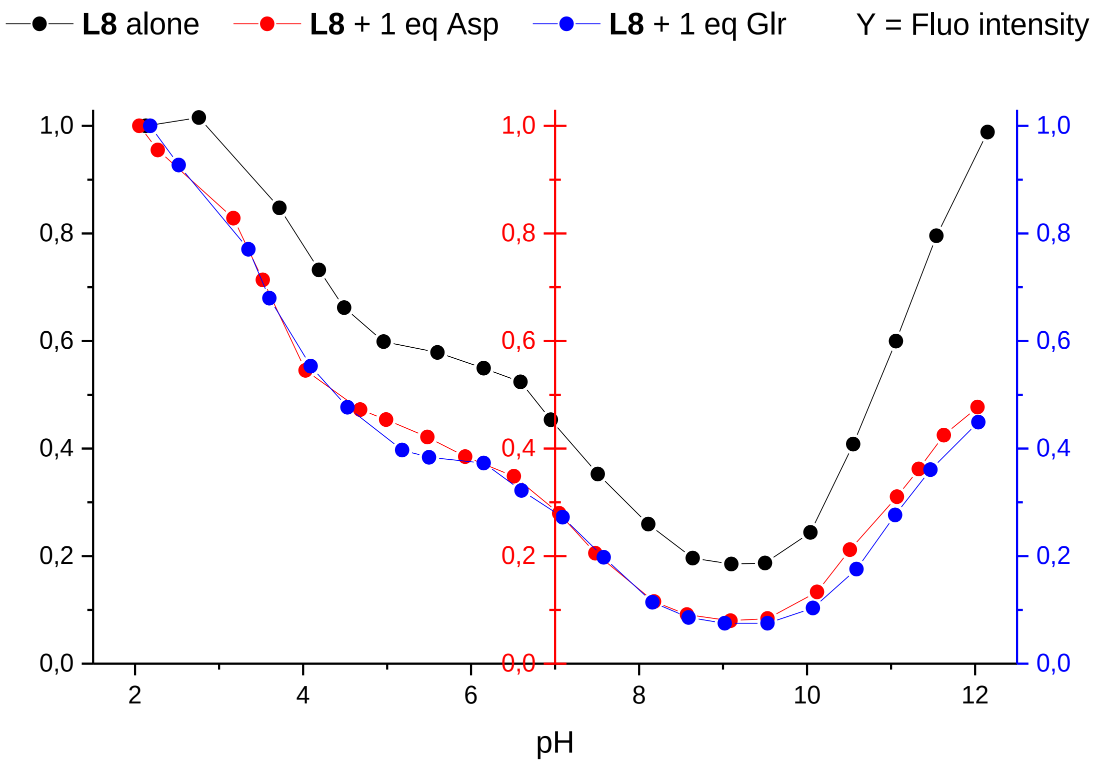

Figure 73. Overlay of fluorescence pH-metric titrations trends of **L8** alone (408 nm, black circles), **L8** + 1 eq of Asp (406 nm, red circles) and **L8** + 1 eq of Glr (407 nm, blue circles) normalized to each starting titration point – pH approximately 2 – λ_{exc} = 284 nm.

2.3.7 Conclusions

With this short study we have demonstrated many things. **L8** has been shown to be selective for two different molecules at opposite pH values: the amino acid L-aspartic at basic pH and the dicarboxylic acid glutaric at acidic pH. It is evident how the length of the carbon chain (Asp 4 C and Glr 5 C) and the presence (Asp) or absence (Glr) of a primary amine can influence the coordination to the same molecule under the same experimental conditions. We have also seen how molecular dynamics calculations and therefore experimental expectations may not match with the scientific evidence. The way in which hydration energies were contemplated in the calculations could also be a reason for the mismatching with the experiments.

We have successfully employed a simple mathematical procedure for the evaluation of simultaneous equilibria and thermodynamic selectivity as a research tool. Such graphical representation of equilibrium data allows a simple visual analysis of speciation and selectivity, even in complex systems, both qualitatively and quantitatively. Surely, it is very important to use equilibrium constants determined under the same experimental conditions to obtain a correct representation of the real system.

Last but not least, we have verified how a given receptor selectivity determined by means of a specific experimental technique may not lead to appreciable variations in its functioning with the use of other techniques in the same experimental conditions.

2.4 Results and Discussion of L9

2.4.1 Synthesis

The scorpiand-type polyamine chemosensor **L9**,[39,43(c)] bearing a fluorescent acridine moiety as signalling unit, has been designed and synthesized following the synthetic strategy outlined in Scheme 9.

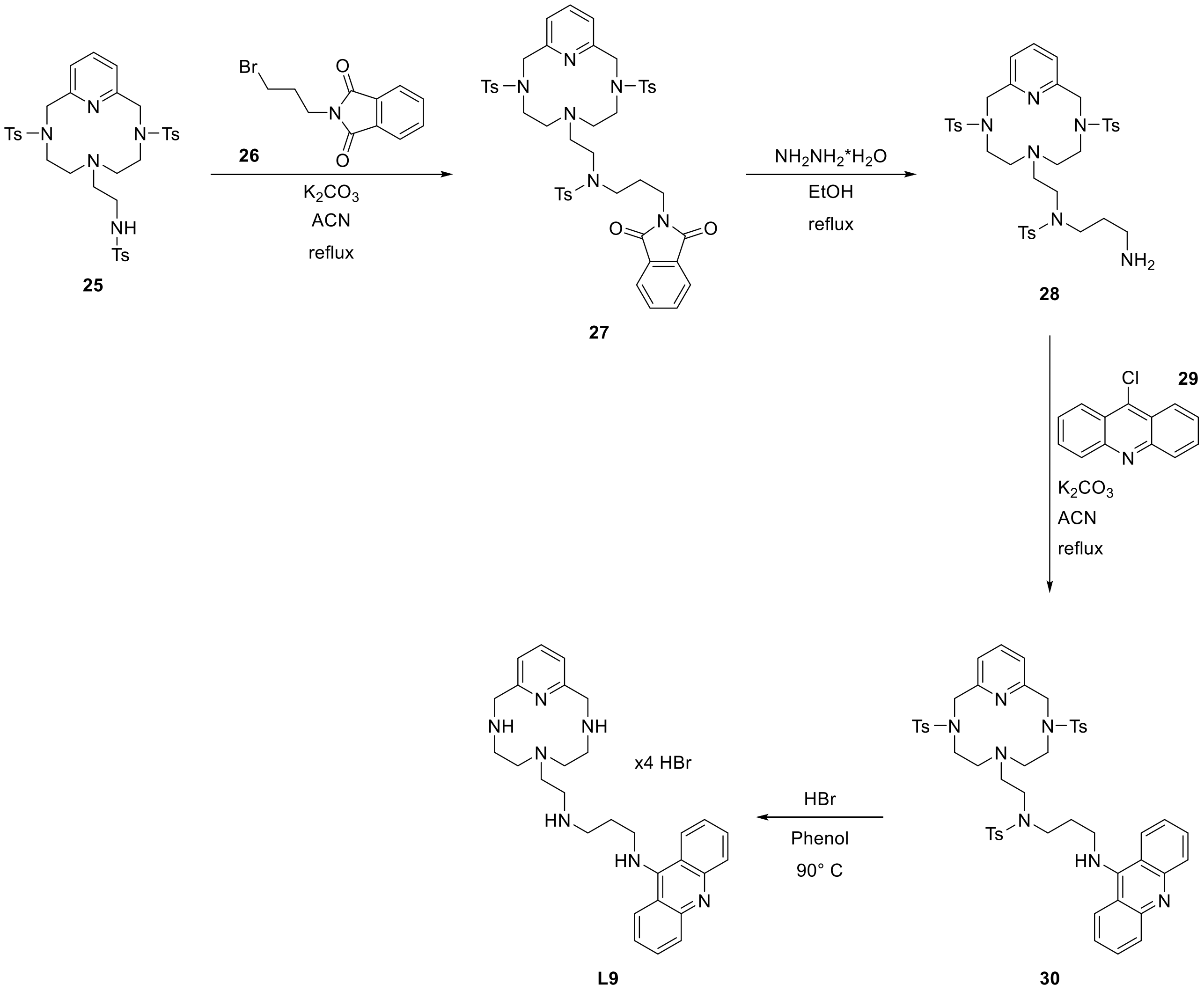

Scheme 9. Synthesis pathway to obtain ligand **L9**.

The synthesis process started from the already tosylated pyridinophane polyamine **25** (synthesized by the group of Professor Enrique García-España at the University of Valencia). that was elongated through addition of the N-alkylphthalimide bromide derivative **26** The product **27** was used in the next step without further purification as any phthalimide obtaining the deprotected intermediate **28**. The functionalization of compound **28** through attachment of the 9-chloroacridine **29** to obtain the compound **30** is the real limiting step of the entire synthetic process, in fact the reaction takes 72 hours to occur; **30** is isolated by flash-chromatography and the yield of the reaction has been optimized to a maximum of 28%. The last reaction step involves the deprotection from tosyl groups using HBr in glacial acetic acid and phenol as scavenger at 90° C. The ligand **L9** spontaneously precipitates by cooling from the reaction mixture as pure tetrabromide salt and further compound was even obtained through precipitation by means of concentration from the mother liquors of the previous filtration in an extremely pure form.

2.4.2 Photophysical and Potentiometric characterization

The initial analyses carried out on the sensor were aimed to provide information on its spectrophotometric behaviour at different pH values, being perfectly water-soluble. Starting from pH 2 the sensor shows three absorption bands between 375 and 450 nm which remain almost constant up to pH 9, further increasing the pH, the bands decrease in intensity. Two isosbestic points at 408 and 440 nm were detected. The emission intensity is very low from pH 2 to pH 9, then it increases becoming very high at pH 12. All data are represented in Figure 74.

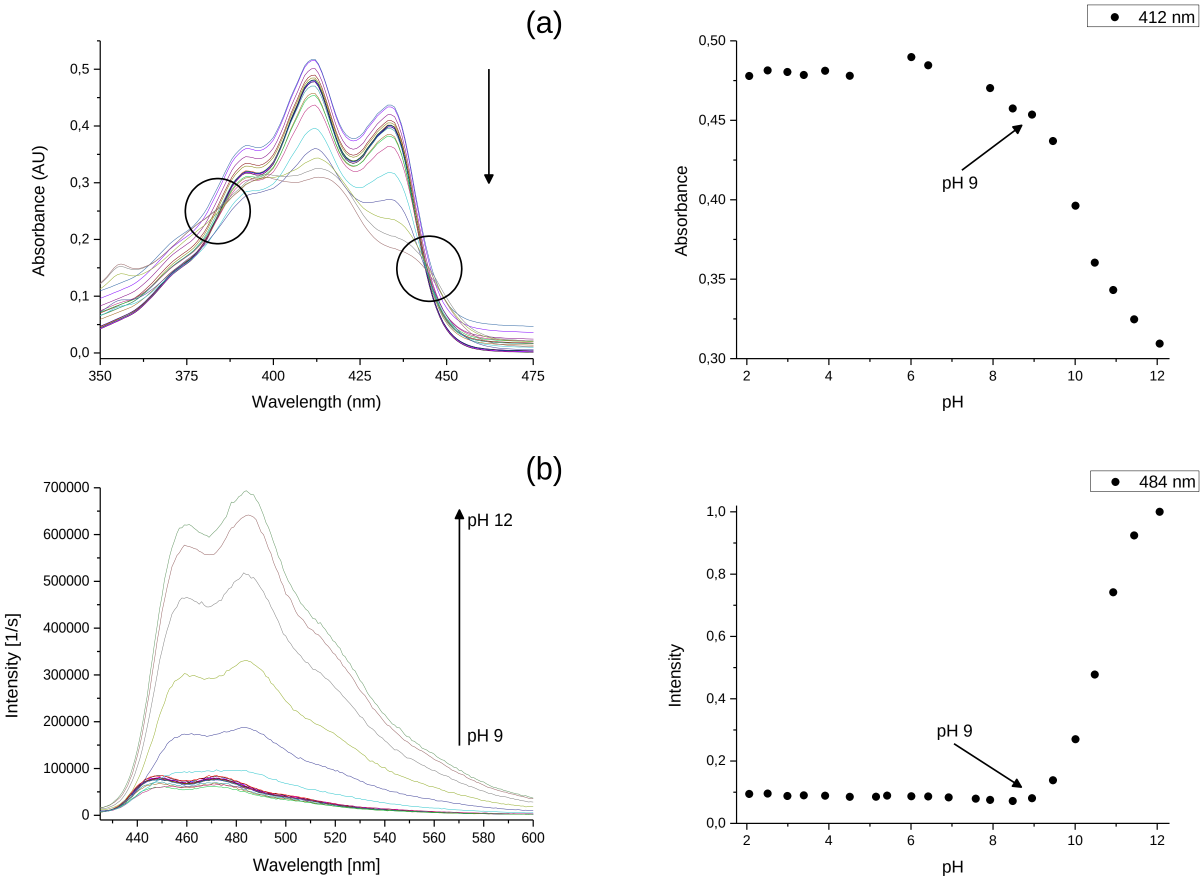

Figure 74. (a) UV-Vis pH titration of **L9** 5x10^{-5} M in $NaClO_4$ 0.15 M and its absorbance trend at 412 nm; (b) Fluo pH titration of **L9** 5x10^{-5} M in $NaClO_4$ 0.15 M and its normalized fluorescence trend at 484 nm (λ_{exc} = 408 nm).

The increase of the fluorescence can be connected with the total deprotonation of the compound and in particular with the deprotonation of the acridine (the phenomenon is attributed to a PET process from the lone pair of the amine to excite the aromatic unit). In order to confirm this deduction, we resorted to a potentiometric titration of **L9**, see Figure 75. The ligand begins to deprotonate from pH 7, the constants listed in Table 9 are related to the protonation of the secondary amines and of the acridine nitrogen. The NH in benzyl position is not subject to protonation/deprotonation as the lone pair is delocalized in the aromatic ring. The totally deprotonated species begins to form after pH 9 and from pH 10 onwards it becomes the only form present in solution.

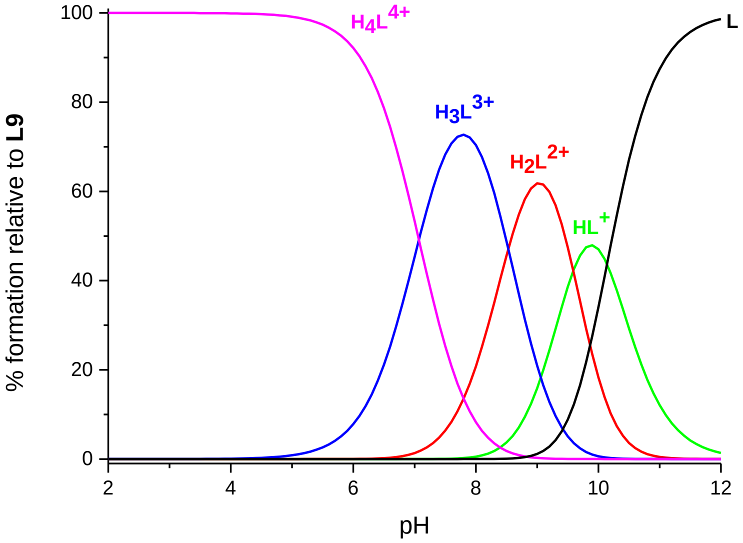

Figure 75. Distribution diagram of the species formed in solution for the system **L9** – [**L9**] = 1x10^{-3} M, $NaClO_4$ 0.15 M, 298.1 K.

Reaction	**log *K***
$H^+ + L \leftrightarrows HL^+$	10.14(2)
$H^+ + HL^+ \leftrightarrows H_2L^{2+}$	9.58(2)
$H^+ + H_2L^{2+} \leftrightarrows H_3L^{3+}$	8.52(2)
$H^+ + H_3L^{3+} \leftrightarrows H_4L^{4+}$	7.07(3)

Table 9. Protonation constant of **L9** determined at 298.1 K in 0.15 M $NaClO_4$.

Again, we superimposed the absorbance and fluorescence trends with the distribution diagrams to understand how the speciation affected the absorption and the emission. As can be seen from the graph (a) reported in Figure 76, the absorbance responds to the deprotonation of the fluorophore nitrogen with the production of the totally deprotonated species **L**. Likewise, the fluorescence (b) perfectly follows the evolution of the species **L**, confirming that the protonation/deprotonation state of the acridine actually drives the intensity of the fluorescence emission.

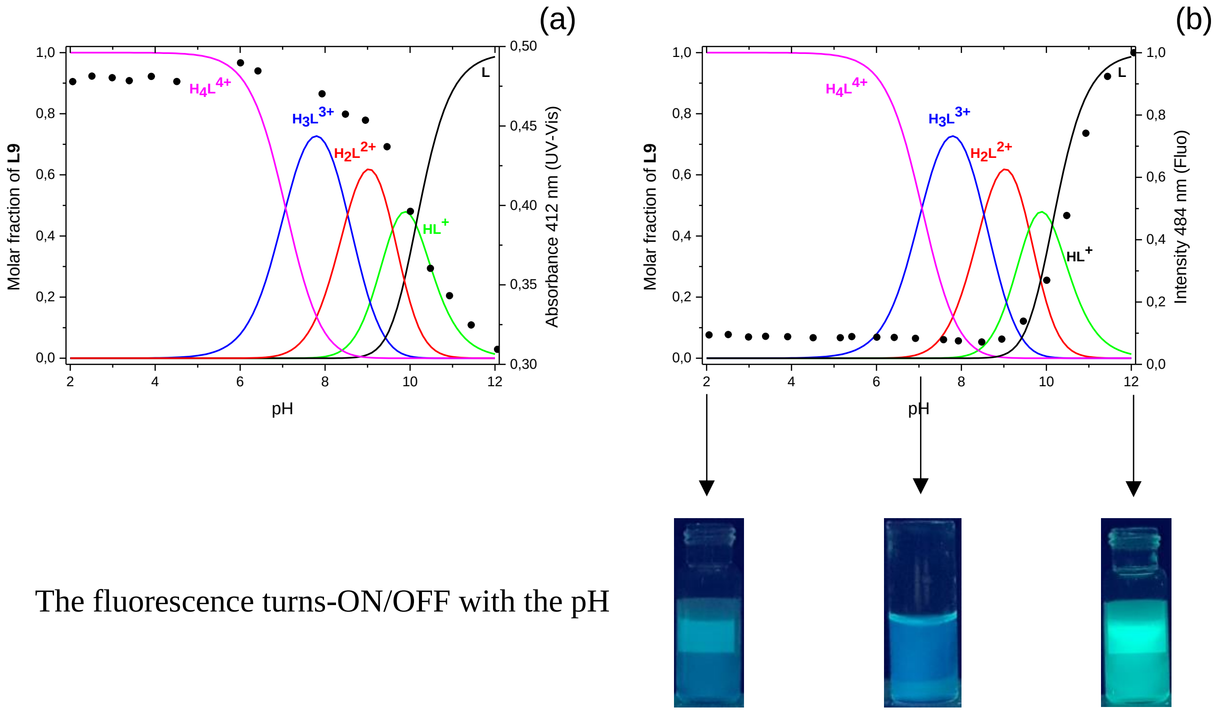

The fluorescence turns-ON/OFF with the pH

Figure 76. (a) Distribution diagram of the species formed in solution for the system **L9** – [**L9**] = 1x10^{-3} M, $NaClO_4$ 0.15 M, 298.1 K – overlaid with UV-Vis pH titration trend at 412 nm of **L9** – 5x10^{-5} M in $NaClO_4$ 0.15 M; (b) Distribution diagram of the species formed in solution for the system **L9** – [**L9**] = 1x10^{-3} M, $NaClO_4$ 0.15 M, 298.1 K – overlaid with Fluo pH titration trend at 484 nm of **L9** – 5x10^{-5} M in $NaClO_4$ 0.15 M – (λ_{exc} = 408 nm).

2.4.3 Interaction with nucleotides

The purpose of the ligand **L9** design is to selectively recognize nucleotides, essential biomolecules within all life-forms, in aqueous media. The interaction of this chemosensor with nucleotide anions has been studied experimentally by UV-Vis and steady-state fluorescence measurements at pH 7, to work at physiological pH and in which there is a fluorescence that gives the possibility to appreciate increases and decreases in its intensity. Interestingly, the results revealed that this receptor can selectively recognize GTP vs. ATP, UTP and GMP, with a distinctive fluorescent response in the visible spectra, which allows for naked-eye estimation (Figure 77-80). Specifically, with ATP and UTP a turn-ON of the ligand fluorescence is obtained with an increase in the emission intensity of 35% and 30% respectively. The selective and discriminating interaction with GTP can be found in a high fluorescence turn-OFF equal to –60%. On the other hand, the interaction between **L9** and GMP does not involve appreciable variations in emission intensity.

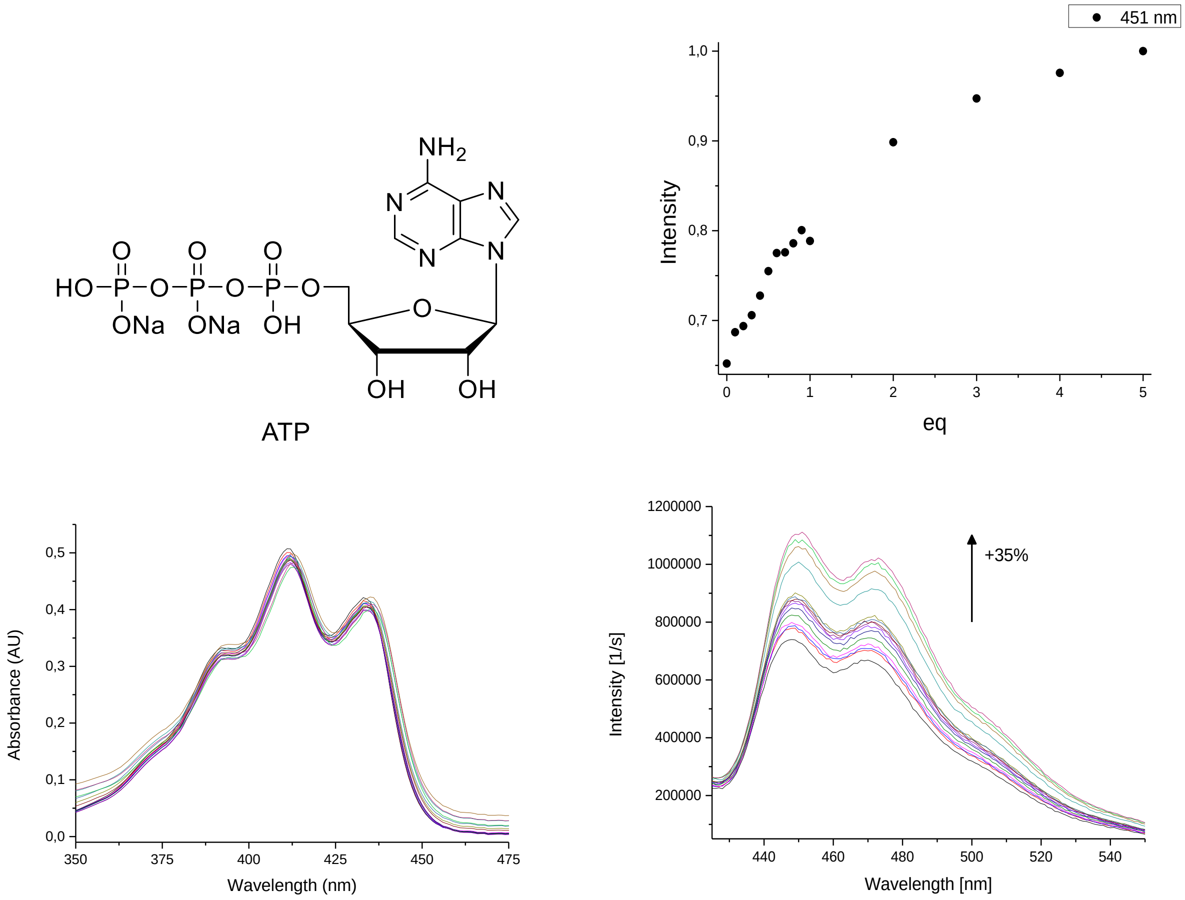

Figure 77. (a) UV-Vis titration of **L9** $5x10^{-5}$ M in $NaClO_4$ 0.15 M at pH = 7 (buffer: sodium cacodylate trihydrate 0.05 M) with ATP $1x10^{-2}$ M; (b) Fluo titration of **L9** $5x10^{-5}$ M in $NaClO_4$ 0.15 M at pH = 7 (buffer: sodium cacodylate trihydrate 0.05 M) with ATP $1x10^{-2}$ M and its normalized fluorescence trend at 451 nm (λ_{exc} = 408 nm).

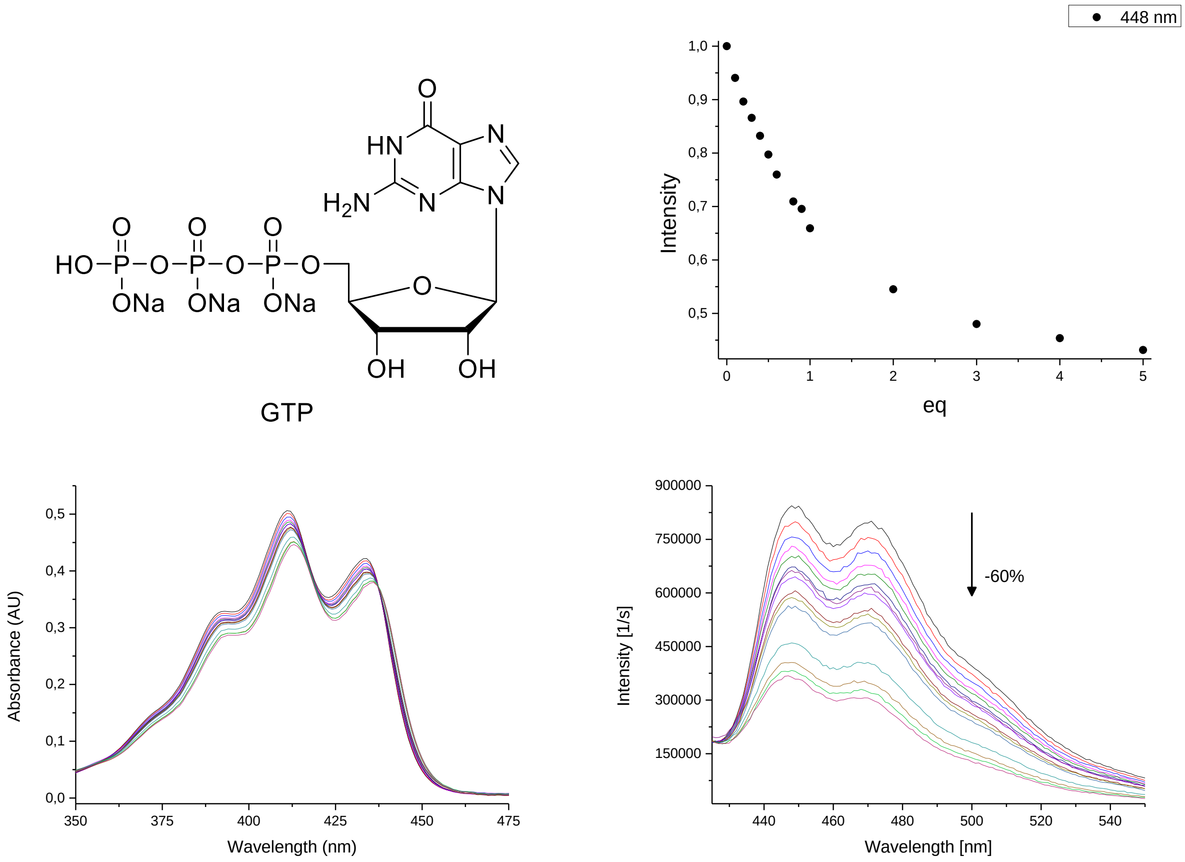

Figure 78. (a) UV-Vis titration of **L9** 5x10^{-5} M in NaClO$_4$ 0.15 M at pH = 7 (buffer: sodium cacodylate trihydrate 0.05 M) with GTP 1x10^{-2} M; (b) Fluo titration of **L9** 5x10^{-5} M in NaClO$_4$ 0.15 M at pH = 7 (buffer: sodium cacodylate trihydrate 0.05 M) with GTP 1x10^{-2} M and its normalized fluorescence trend at 448 nm (λ_{exc} = 408 nm).

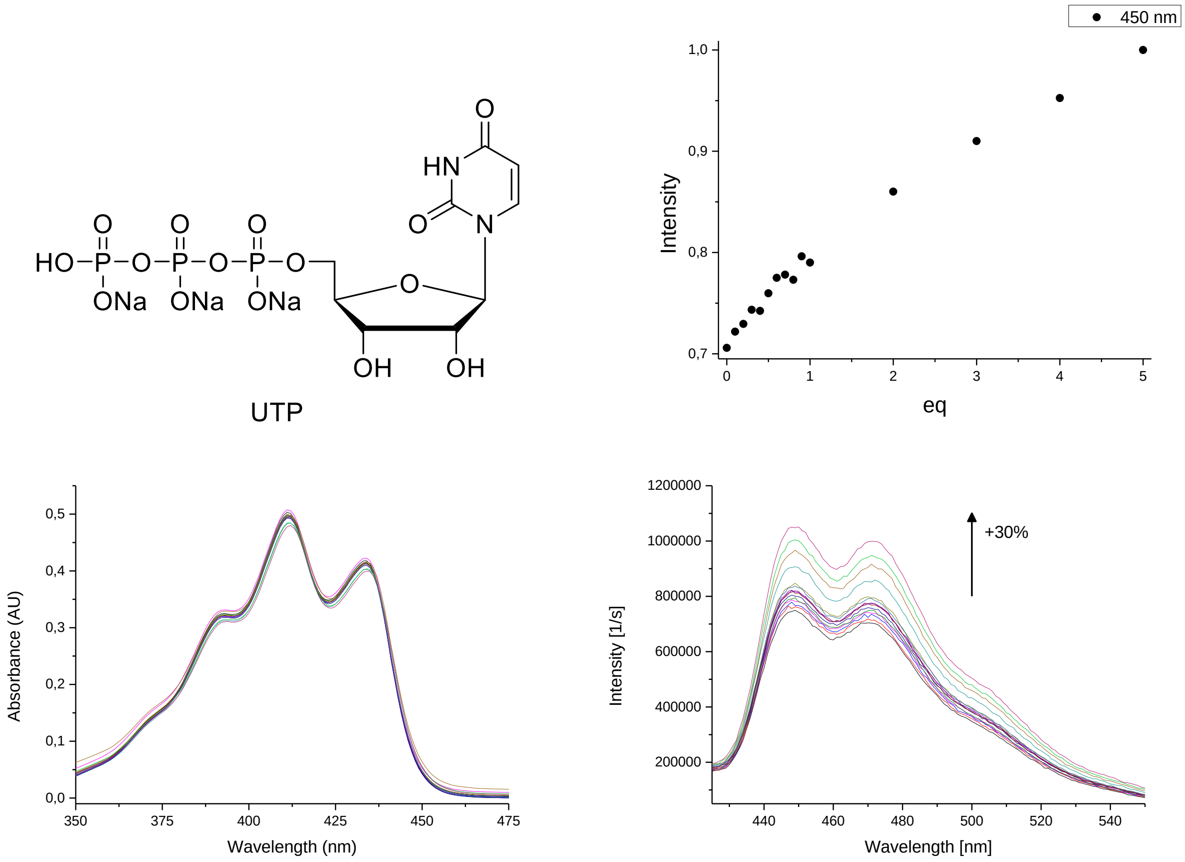

Figure 79. (a) UV-Vis titration of **L9** 5x10^{-5} M in NaClO$_4$ 0.15 M at pH = 7 (buffer: sodium cacodylate trihydrate 0.05 M) with UTP 1x10^{-2} M; (b) Fluo titration of **L9** 5x10^{-5} M in NaClO$_4$ 0.15 M at pH = 7 (buffer: sodium cacodylate trihydrate 0.05 M) with UTP 1x10^{-2} M and its normalized fluorescence trend at 450 nm (λ_{exc} = 408 nm).

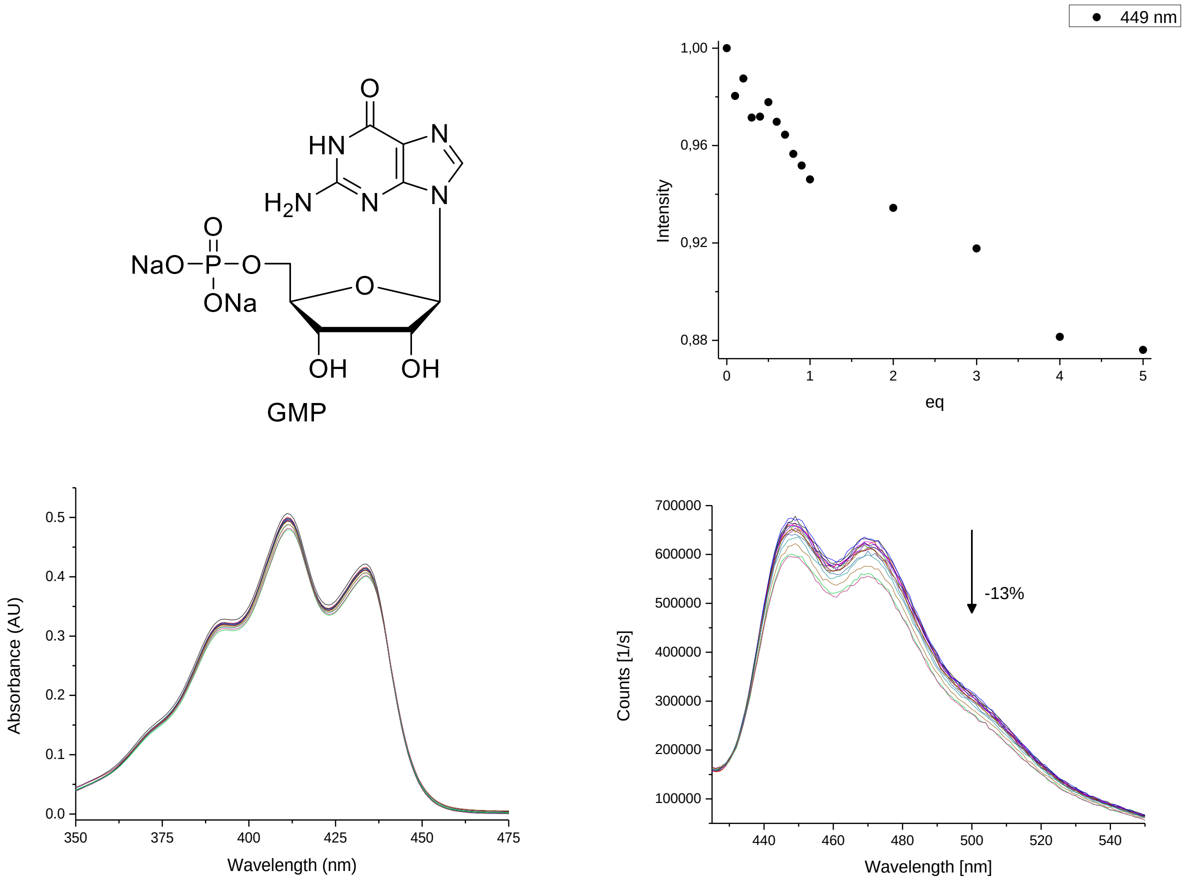

Figure 80. (a) UV-Vis titration of **L9** 5x10^{-5} M in $NaClO_4$ 0.15 M at pH = 7 (buffer: sodium cacodylate trihydrate 0.05 M) with GMP 1x10^{-2} M; (b) Fluo titration of **L9** 5x10^{-5} M in $NaClO_4$ 0.15 M at pH = 7 (buffer: sodium cacodylate trihydrate 0.05 M) with GMP 1x10^{-2} M and its normalized fluorescence trend at 449 nm (λ_{exc} = 408 nm).

The association constants between **L9** and the studied targets were calculated from both UV-Vis and Fluo titrations. The results obtained, shown in Tables 10 and 11, are comparable to each other and the highest constant in either case is that relating to the selective interaction with GTP.

		UV-Vis		
	ATP	**GTP**	**UTP**	**GMP**
Reaction[a]			**log *β***	
L + X ⇆ XL	4.02(1)	**4.33(2)**	3.65(5)	3.80(2)
[a]Charges omitted				

Table 10. Logarithms of the equilibrium constants in the interaction of ATP, GTP, UTP and GMP with **L9** at 298.1 K in 0.15 M $NaClO_4$, obtained from UV-Vis titrations.

		Fluo		
	ATP	**GTP**	**UTP**	**GMP**
Reaction[a]			**log *β***	
L + X ⇆ XL	3.97(6)	**4.34(2)**	3.31(1)	3.54(2)
[a]Charges omitted				

Table 11. Logarithms of the equilibrium contants in the interaction of ATP, GTP, UTP and GMP with **L9** at 298.1 K in 0.15 M $NaClO_4$, obtained from Fluo titrations.

2.4.4 Conclusions

To rationalize the nature of these interactions and explain the differences in selectivity a set of molecular dynamics calculations have also been performed, using Amber 2019[67] and GAFF potentials at 300 K, Figure 81. It seems that the selective recognition of **L9** for the GTP vs ATP is due to the higher ability of the guanine to form π-stacking complexes with the acridine present in the pendant arm, while the hydrogen bond network can only be established with adenine as nucleotide and not with guanine. As can be seen, the increase and decrease in fluorescence are easily found visually, compared to the fluorescence of **L9** at physiological pH.

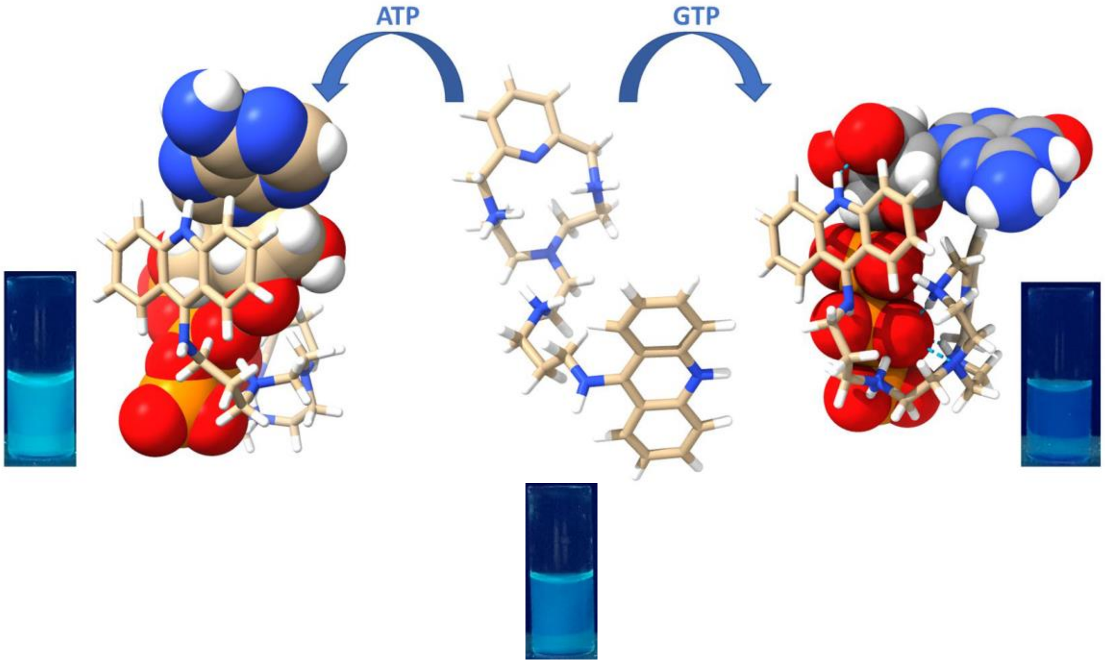

Figure 81. Molecular dynamics calculations of the interaction between **L9** and ATP vs GTP + corresponding visual fluorescence induced by exposure to ultraviolet light in vials.

Chapter 3 – Experimental section

3.1 General overview of the Scientific Methods & Instruments

3.1.1 Synthesis and Characterization of the Ligands

All reactions involving moisture-sensitive reagents were carried out under a nitrogen atmosphere using standard vacuum line techniques and glassware that was flame-dried before use. All other solvents and reagents were used as supplied (analytical or HPLC grade) without prior purification. All chemicals were purchased from Aldrich, Fluka and Lancaster in the highest quality commercially available. All the solvents were dried prior to use.

3.1.2 NMR Spectroscopy

^{1}H-NMR (600 MHz, 400 MHz and 300 MHz) and ^{13}C-NMR (151 MHz, 100 MHz) spectra were determined on a 600 MHz Bruker and on a 400 MHz Bruker Avance instrument both equipped with a variable temperature controller. The temperature of the NMR probe was calibrated using 1,2-ethandiol as calibration sample. NMR spectra were recorded at 298 K, chemical shifts (δ scale) for ^{1}H-NMR and ^{13}C-NMR were reported in parts per million (ppm values), referenced relative to residual proton in the deuterated solvent, with coupling constants (J values) reported in Hertz (Hz). ^{1}H-^{1}H and ^{1}H-^{13}C correlation experiments were performed using standard Bruker pulse sequence to study the ligands and the host-guest complexes and to assign the signals. The following abbreviations were used for spin multiplicity: s = singlet, d = doublet, t = triplet, q = quartet, quint = quintet, m = multiplet, dd = doublet of doublets, td = triplet of doublets, br s = broad signal. Proton NMR titrations were performed by adding aliquots of a putative guest at known concentration in a solution of the receptor at a specific concentration in a determined deuterated solvent.

3.1.3 Elemental Analysis

Elemental analyses were performed with a Thermo Finnigan Flash 1112 EA CHN analyser.

3.1.4 Density Functional Theory (DFT) calculations

Chapter 2.1. Calculations were carried out at the density functional theory (DFT)[50] level with the commercial suite Gaussian 16,[70] with the hybrid mPW1PW functional,[71] including a modified Perdew and Wang (PW) exchange functional coupled with the PW correlation functional.[72] Schäfer, Horn, and Ahlrichs split-valence plus polarization[73] all-electron basis sets were used in the Weigend formulation Def2SVP.[74] The geometry of all compounds was optimized. The nature of the minima of each structure was verified by harmonic frequency calculations. TD-DFT calculations were carried out at the optimized geometries. GaussView 6.0.16[75] was used to draw Kohn-Sham (KS) molecular orbital (MO) compositions, to generate molecular electrostatic potential maps, to analyse natural charge distributions, and to prepare TD-simulated spectra and calculate molar extinction coefficients from oscillator strengths.

Chapter 2.3 and 2.4. Calculations were carried out at the density functional theory (DFT) level with the commercial suite AMBER[67] and the GAFF force field (3 ns calculations).

3.1.5 UV-Visible and Fluorescence Spectroscopy

UV-Vis absorption spectra were recorded at 298.1 K on a Varian Cary-100 spectrophotometer equipped with a temperature control unit. Fluorescence emission spectra were recorded at 298.1 K on a Varian Cary Eclipse spectrofluorimeter and the spectra are uncorrected. Emission quantum yields were calculated using 2,2′-biphenol in acetonitrile as standard ($\phi^{\cdot}$em = 0.29).[64] The HypSpec computer program (Hyperquad package) was used to process the spectrophotometric data.[64] The pH-metric UV-Vis and fluorescence titration were carried out adjusting the pH by adding of NaOH or $HClO_4$ and values were corrected considering the autoprotolysis product of the solvent mixture ($pK_w = 14.62$).[76] At least three sets of spectrophotometric titration curves for each guest/L system were performed. All sets of curves were treated either as single sets or as separate entities, for each system; no significant variations were found in the values of the determined constants.

3.1.6 Electromotive Force (emf) measurements

The potentiometric titrations were carried out with a potentiometric titrator 905 Titrando from Metrohm at 298.1 ± 0.1 K in 0.15 M $NaClO_4$. The experimental procedure used (burette, potentiometer, cell, stirrer, microcomputer, etc.) has been fully described in literature.[77] The acquisition of the emf data was performed with the computer program tiamo[78]. The reference electrode was an Ag/AgCl electrode in sat. KCl soln. The glass electrode was calibrated as a hydrogen-ion-concentration probe by titration of previously standardized amounts of HCl with CO_2-free NaOH solns. and determining the equivalent point by Gran's method[79], which gives the standard potential, $E^{0'}$, and the ion product of water ($pK_w = 13.73(1)$). The concentrations of the different analytes employed were determined gravimetrically by standard methods. The computer program Hyperquad[64], was used to calculate the protonation and stability constants. At least three titration curves were performed for each system (ca. 100 exper. points). The pH range investigated was 2.0 – 11.0, and the concentration of the analytes and the receptors was around $1x10^{-3}$ M.

3.2 Synthesis of the Ligands

3.2.1 Synthesis and Characterization of L1, L2 and L3

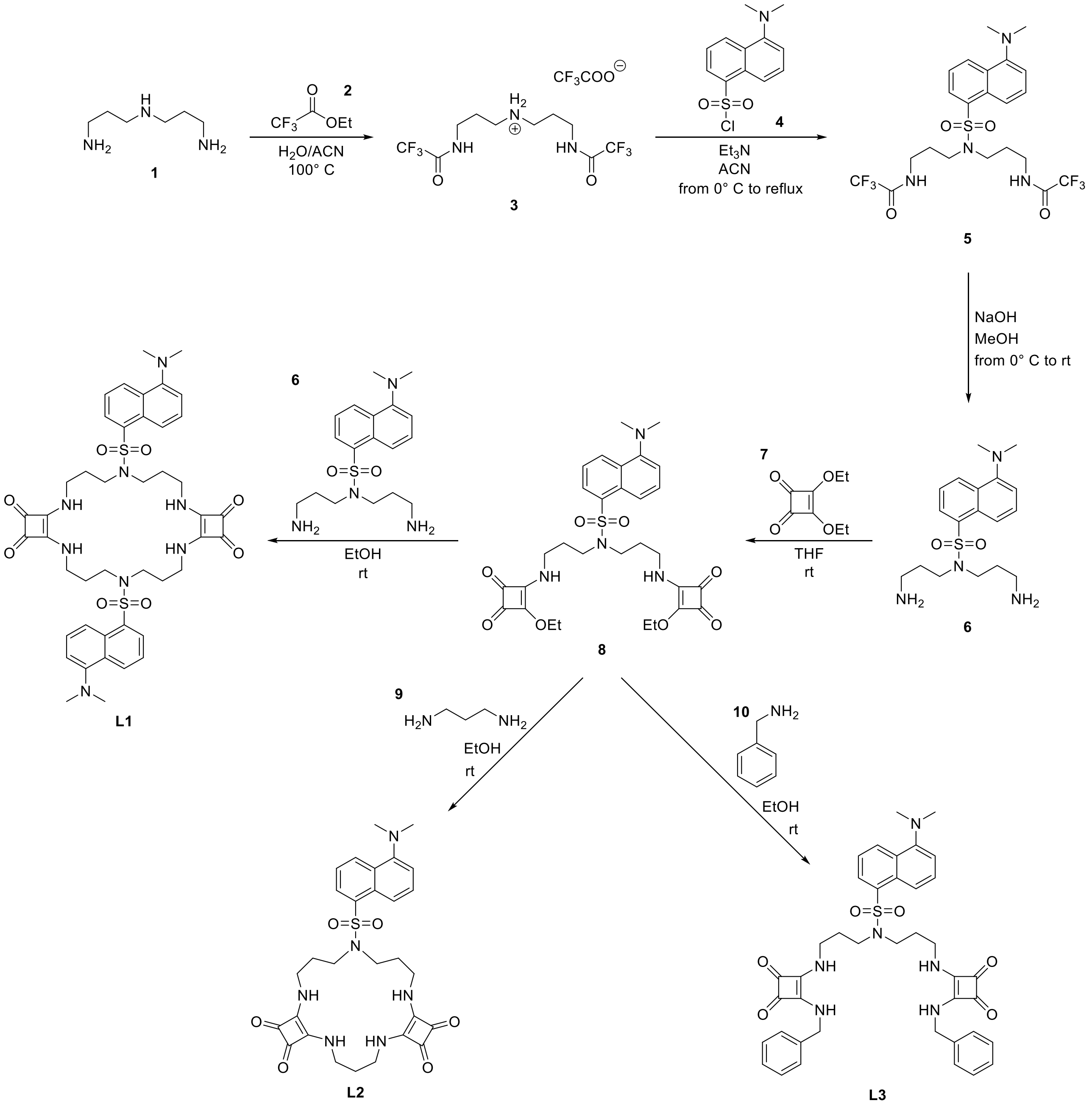

Synthesis of bis(3-(2,2,2-trifluoroacetamido)propyl)ammonium 2,2,2-trifluoroacetate (3)[44]

A solution of ethyl 2,2,2-trifluoroacetate (**2**) (18 g, 127 mmol) was added dropwise to a stirred solution of **1** (5 g, 38.1 mmol) in a mixture of acetonitrile (35 mL)/water (0.8 mL) and refluxed overnight. The product was crystallized from the hot solution and an ice bath was used to increase the crystallization rate. The precipitate that formed was filtered and washed with diethyl ether to obtain **3** as a white solid (14 g, 84%).

^{1}H-NMR (400 MHz, D_2O): δ (ppm) = 1.86 (quint, 4H, *J* = 7.3 Hz), 2.96 (t, 4H, *J* = 7.8 Hz), 3.31 (t, 4H, *J* = 6.8 Hz).

Synthesis of N,N-bis(3-trifluoroacetylamino)propyl)-5-(dimethylamino)naphthalene-1-sulfonamide (5)

A solution of 5-(dimethylamino)naphthalene-1-sulfonyl chloride (**4**) (dansyl chloride, 3.56 g, 12 mmol) in acetonitrile (200 mL) was added dropwise, in a nitrogen atmosphere, to a stirred solution of N,N-bis(3-trifluoroacetylamino)propyl)amine (**3**) (5 g, 11 mmol) in triethylamine (5 mL, 35 mmol) and refluxed overnight. The resulting mixture was filtered to remove the insoluble salts, concentrated under reduced pressure to 50 mL and poured in 200 mL of cold water. The resulting suspension was extracted with ethyl acetate (3x50 mL), the combined organic extracts were dried with anhydrous Na_2SO_4 and evaporated under reduced pressure affording 6 g of a grey/greenish solid which was purified by crystallization from hot ethanol to obtain **5** as white/green needle-like crystals (3.46 g. 54%).

^{1}H-NMR (400 MHz, $CDCl_3$): δ (ppm) = 1.84 (quint, 4H, *J* = 6.4 Hz), 2.90 (s, 6H), 3.38 (t, 4H, *J* = 6.4 Hz), 3.45 (q, 4H, *J* = 6.5 Hz), 7.03 (br s, 2H), 7.22 (d, 1H, *J* = 7.6 Hz), 7.55 (dd, 1H, J_1=8.5 J_2=7.5 Hz), 7.60 (dd, 1H, J_1 = 8.6 J_2 = 7.6 Hz), 8.04 (dd, 1H, J_1 = 7.3 J_2 = 1.3 Hz), 8.23 (d, 1H, *J* = 8.8 Hz), 8.59 (d, 1H, *J* = 8.6 Hz).

Synthesis of N,N-bis(3-aminopropyl)-5-(dimethylamino)naphthalene-1-sulfonamide (6)

120 mL of 0.2 M sodium hydroxide in methanol was dropwise added to a stirred solution of **5** (3.46 g, 6.22 mmol) in 500 mL of methanol at 0° C under nitrogen atmosphere. When the addition was complete, the cooling bath was removed and the mixture was stirred overnight at room temperature. The solvent was evaporated under reduced pressure obtaining an oily residue that was suspended in 100 mL of water and extracted with chloroform (4x150 mL). The combined organic extracts were dried with anhydrous Na_2SO_4 and evaporated under reduced pressure to obtain **6** as a yellow/orange oil (2.46 g, 100%).

^{1}H-NMR (400 MHz, $CDCl_3$): δ (ppm) = 1.58 (br s, 4H), 1.64 (quint, 4H, J = 7.0 Hz), 2.62 (t, 4H, J = 6.7), 2.87 (s, 6H), 3.37 (t, 4H, J = 7.3 Hz), 7.17 (d, 1H, J = 7.6), 7.51 (dd, 1H, J_1 = 8.6 J_2 = 7.6 Hz), 7.55 (dd, 1H, J_1 = 8.6 J_2 = 7.6 Hz), 8.15 (dd, 1H, J_1 = 7.3 J_2 = 1.3 Hz), 8.27 (d, 1H, J = 8.8 Hz), 8.52 (d, 1H, J = 8.3 Hz).

Synthesis of 1,2-diethoxy-3,4-dioxocyclobut-1-ene (7)

10 g of 3,4-dihydroxycyclobut-3-ene-1,2-dione (**11**) (squaric acid, 88 mmol) were added to 250 mL of ethanol at room temperature and then the reaction mixture was refluxed overnight. The ethanol was removed under reduced pressure and the aqueous residue was dissolved in ethyl ether. The organic layer was washed three times with saturated $NaHCO_3$ and subsequently dried with Na_2SO_4. The mixture was dried under reduced pressure, then dichloromethane is added and dried again. The product was vacuum dried yielding **7** as a light orange/pink oil (11 g, 74%).

^{1}H-NMR (400 MHz, $CDCl_3$): δ (ppm) = 1.48 (t, 6H, J = 7.2), 4.74 (q, 4H, J = 7.2).

Synthesis of N,N-bis(3-(2-ethoxy-3,4-dioxocyclobut-1-en-1-yl)aminopropyl)-5-(dimethylamino)naphthalene-1-sulfonamide (8)

Over a period of 3 h a solution of 1,2-diethoxy-3,4-dioxocyclobut-1-ene (**7**) (1.26 g, 7.42 mmol) in tetrahydrofuran (60 mL) was added to a stirred solution of **6** (1.23 g, 3.37 mmol) in tetrahydrofuran (200 mL) under nitrogen atmosphere. The mixture was stirred at room temperature for 72 h, then the solvent was evaporated under reduced pressure affording a yellow/orange oil. The crude product was purified by chromatography (silica, ethyl acetate/hexane 8:2) to obtain the **8** as a yellow/orange oil (1.2 g, 58%).

^{1}H-NMR (400 MHz, $CDCl_3$): δ (ppm) = 1.42 (t, 6H, *J* = 6.9 Hz), 1.83-2.01 (m, 4H), 2.88 (s, 6H), 3.31-3.74 (m, 8H), 4.73 (q, 4H, *J* = 7.0 Hz), 7.19 (d, 1H, *J* = 7.6 Hz), 7.43 (br s, 2H), 7.48-7.62 (m, 2H), 8.06 (d, 1H, *J* = 7.1), 8.24 (t, 1H, *J* = 9.1 Hz), 8.54 (d, 1H, *J* = 7.8 Hz).

Synthesis of 6,19-bis(5-(dimethylamino)naphthalen-1-yl-sulphonyl)-12,13,25,26-tetraoxo-2,6,10,15,19,23-hexaazatricyclo[22.2.0.0(11,14)]hexaicosa-1(24),11(14)-diene (L1)

Over a period of 6 h a solution of **6** (0.18 g, 0.490 mmol) in ethanol (100 mL) was added dropwise to a stirred solution of **8** (0.30 g, 0.490 mmol) in ethanol (100 mL). The reaction mixture was stirred at room temperature for 72 h. The yellow precipitate that formed was filtered, washed with ethanol and re-crystallized from hot DMF affording pure **L1** as pale-yellow solid (0.227 g, 64%).

^{1}H-NMR (400 MHz, DMSO-d_6): δ (ppm) = 1.65 (br s, 8H), 2.83 (s, 12H), 3.26 (t, 8H, *J* = 8.3 Hz), 3.36 (br s, 8H), 7.24 (d, 2H, *J* = 7.6 Hz), 7.56-7.66 (m, 4H), 8.09 (d, 2H, *J* = 7.1 Hz), 8.17 (d, 2H, *J* = 8.8 Hz), 8.48 (d, 2H, *J* = 8.6 Hz).

^{13}C-NMR (100 MHz, DMSO-d_6): δ (ppm) = 30.2, 41.3, 44.5, 45.5, 115.7, 119.2, 124.1, 128.6, 129.3, 129.7, 129.8, 130.4, 135.2, 151.9, 168.1, 182.9.

Elemental analysis for $C_{44}H_{52}N_8O_8S_2$: calcd C 59.71, H 5.92, N 12.66, S 7.24; found C 59.6, H 6.0, N 12.5, S 7.4.

(ESI): *m/z* calcd. for $C_{44}H_{52}N_8O_8S_2$: 884.33; found: 885.2 $[M+H]^+$.

Synthesis of 6-(5-(dimethylamino)naphthalen-1-yl-sulphonyl)-12,13,21,21-tetraoxo-2,6,10,15,19-pentaazatricyclo[18.2.0.0(11,14)]doicosa-1(20),11(14)-diene (L2)

A solution of 1,3-propylendiamine (**9**) (4 mg, 0.490 mmol) in ethanol (100 mL) was added dropwise to a stirred solution of **7** (0.30 g, 0.490 mmol) in ethanol (100 mL). The reaction mixture was stirred at room temperature for 72 h. The yellow precipitate that formed was filtered, washed with ethanol and re-crystallized from hot DMF affording pure **L2** as pale-yellow solid (0.228 g, 78%).

^{1}H-NMR (400 MHz, DMSO-d_6): δ (ppm) = 1.64 (br s, 4H), 1.85 (br s, 2H), 2.85 (s, 6H), 3.28 (t, 4H, J = 7.3 Hz), 3.35-3.46 (m, 4H), 3.47-3.73 (br s, 4H), 7.28 (d, 1H, J = 7.3 Hz), 7.63 (dd, 1H, J_1 = 8.5 Hz J_2 = 7.7 Hz), 7.66 (dd, 1H, J_1 = 8.5 Hz J_2 = 7.5 Hz), 8.14 (d, 1H, J = 7.1 Hz), 8.21 (d, 1H, J = 8.8 Hz), 8.52 (d, 1H, J = 8.3 Hz).

^{13}C-NMR (100 MHz, DMSO-d_6): δ (ppm) = 30.5, 31.2, 40.8, 44.3, 45.5, 115.7, 119.2, 124.2, 128.7, 129.7, 129.8, 130.6, 152.0, 168.3, 183.0.

Elemental analysis for $C_{29}H_{34}N_6O_6S$: calcd C 58.57, H 5.76, N 14.13, S 5.39; found C 58.5, H 5.8, N 14.0, S 5.3.

(ESI): *m/z* calcd. for $C_{29}H_{34}N_6O_6S$: 594.23; found: 595.2 $[M+H]^+$.

Synthesis of N,N-bis(3-(benzylamino)-3,4-dioxocyclobut-1-en-1-yl)amino)propyl)-5-(dimethylamino)naphthalene-1-sulfonamide (L3)

A solution of benzylamine (**10**) (91.0 mg, 0.84 mmol) in ethanol (50 mL) was added dropwise to a stirred solution of **7** (0.260 g, 0.42 mmol) in ethanol (50 mL). The reaction mixture was stirred for 96 h. The precipitate that formed was filtered, washed with ethanol and re-crystallized from hot DMF affording pure **L3** as pearly-white solid (0.291 g, 93%).

^{1}H-NMR (400 MHz, DMSO-*d*$_6$): δ (ppm) = 1.69 (quint, 4H, *J* = 7.3 Hz), 2.81 (s, 6H), 3.31 (br s, 4H), 3.43 (br s, 4H), 4.72 (s, 4H), 7.19-7.25 (m, 1H), 7.25-7.41 (m, 10H), 7.49 (t, 1H, *J* = 8.0 Hz), 7.55 (t, 1H, *J* = 8.1 Hz), 7.75 (br s, 2H), 8.00-8.06 (m, 1H), 8.15 (d, 1H, *J* = 8.6 Hz), 8.40-8.46 (m, 1H).

^{13}C NMR (100 MHz, DMSO-*d*$_6$): δ (ppm) = 47.2, 30.3, 41.3, 44.9, 45.5, 115.7, 119.1, 123.9, 127.9, 128.0, 128.6, 129.1, 129.7, 129.8, 130.3, 135.3, 139.5, 151.9, 167.9, 168.2, 183.0.

Elemental analysis for $C_{40}H_{42}N_6O_6S$: calcd C 65.38, H 5.76, N 11.44, S 4.36; found C 65.3, H 5.8, N 11.3, S 4.3.

(ESI): *m/z* calcd. for $C_{40}H_{42}N_6O_6S$: 734.29; found: 735.2 $[M+H]^+$.

3.2.2 Synthesis and Characterization of L4

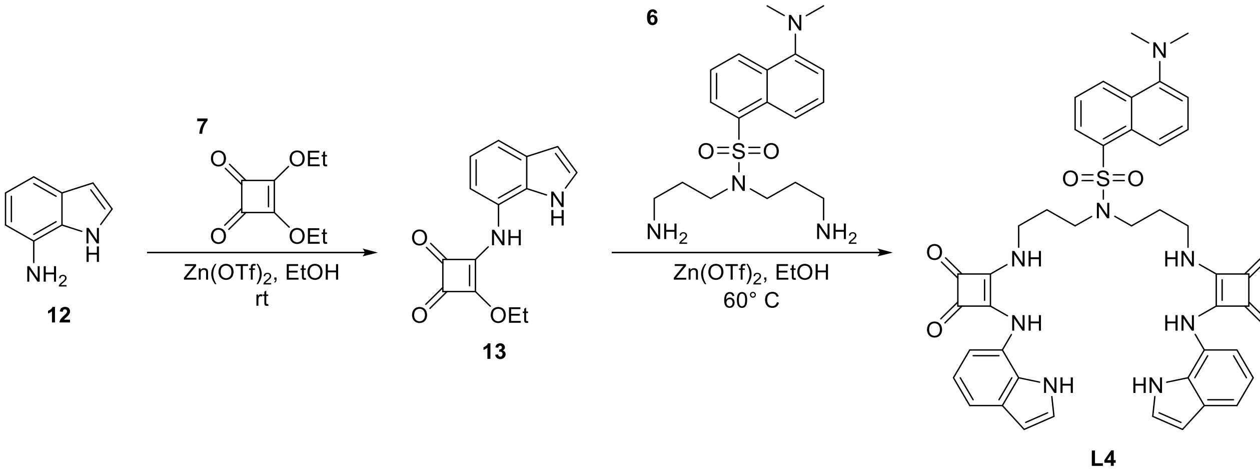

Synthesis of 3-((1H-indol-7-yl)amino)-4-ethoxycyclobut-3-ene-1,2-dione (13)

To a stirred solution of 3,4-diethoxycyclobut-3-ene-1,2-dione (**7**) (200 mg, 1.18 mmol) and zinc trifluoromethanesulfonate (10 mol %) in dry ethanol (10 mL) at room temperature the 7-aminoindole (**12**) (140 mg, 1.06 mmol) was added. Reaction progress was monitored by TLC chromatography (SiO_2, hexane/ethyl acetate 1:1). Once completed, the solvent was removed under reduced pressure and the crude was purified by column chromatography (SiO_2, hexane/ethyl acetate 3:2). The fractions containing the desired product were combined and the solvent evaporated, collecting it as crude brown solid (227 mg, 0.9 mmol). Yield: 0.25 g, 84%.

^{1}H-NMR (600 MHz, DMSO-d_6): δ (ppm) = 1.39 (t, 3H, J =7.3 Hz), 4.74 (q, 2H, J =7.1 Hz), 6.55 (t, 1H, J = 2.1 Hz), 7.05 (t, 1H, J = 7.7 Hz), 7.12 (s, 1H), 7.44 (t, 1H, J = 2.3 Hz), 7.47 (d, 1H, J = 7.7 Hz), 10.57 (s, 1H), 11.07 (s, 1H).

Synthesis of N,N-bis(3-((2-((1H-indol-6-yl)amino)-3,4-dioxocyclobut-1-en-1-yl)amino)propyl)-5-(dimethylamino)naphthalene-1-sulfonamide (L4)

To a solution of 3-((1H-indol-7-yl)amino)-4-ethoxycyclobut-3-ene-1,2-dione (0.1828 g, 0.7133 mmol) in 30 mL of ethanol, in the presence of $Zn(OTf)_2$ (20 mol %), heated up to 60° C, N,N-bis(3-aminopropyl)-5-(dimethylamino)naphthalene-1-sulfonamide (0.1280 g, 0.3512 mmol) was added. A pale-yellow precipitate formed immediately after the addition. The suspension was stirred for 24h. The precipitate was isolated through filtration and the product (0.175 g, 63.3%) was used without further purification.

^{1}H-NMR (600 MHz, DMSO-d_6): δ (ppm) = 2.08 (s, 4H), 2.81 (s, 6H), 3.36 (s, 4H), 3.55 (s, 4H), 6.47 (s, 2H), 6.94 (m, 4H), 7.25 (s, 2H), 7.33 (d, 2H, *J* = 12 Hz), 7.38 (s, 2H), 7.58 (m, 3H), 8.05 (d, 1H, *J* = 12 Hz), 8.17 (d, 1H, *J* = 12 Hz), 8.44 (d, 1H, *J* = 12 Hz), 9.50 (s, 2H), 10.93 (s, 2H).

^{13}C-NMR (151 MHz, DMSO-d_6): δ (ppm) = 27.8, 44.2, 46.2, 51.0, 102.4, 107.3, 110.7, 117.6, 119.9, 123.1, 123.7, 124.3, 124.9, 126.3, 127.9, 128.3, 129.0, 129.2, 133.0, 135.1, 143.3, 143.5, 146.1, 151.3, 187.0, 187.1.

Elemental analysis for $C_{42}H_{40}N_8O_6S$: calcd C 64.27, H 5.14, N 14.28, S 4.08; found C 64.2, H 5.2, N 14.3, S 4.1.

(ESI$^-$): *m/z* calcd. for $C_{42}H_{40}N_8O_6S$: 879 [M-H + DMSO+H_2O]$^-$; found: 783.3 [M-H]$^-$.

3.2.3 Synthesis and Characterization of L5

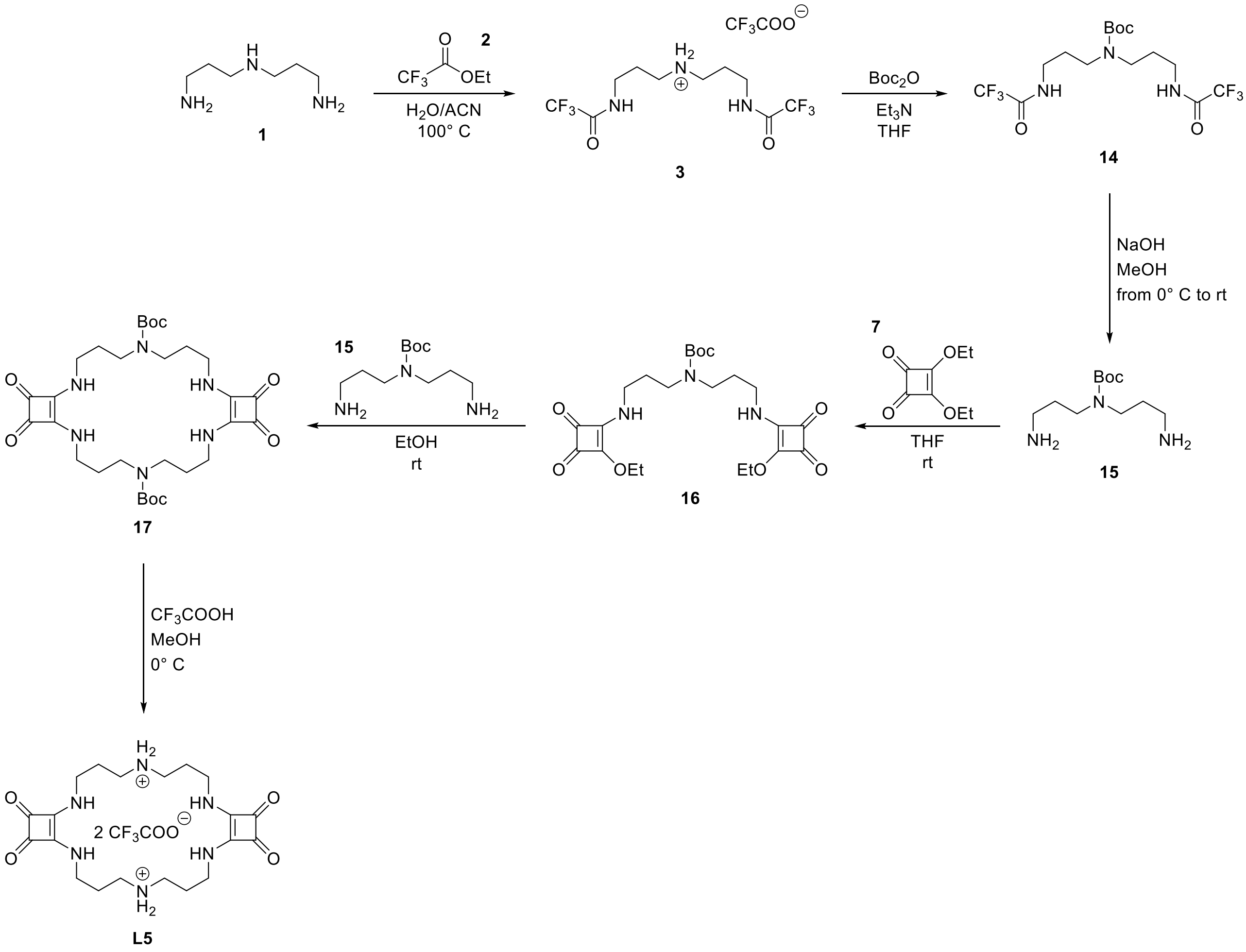

Synthesis of tert-butyl bis(3-(2,2,2-trifluoroacetamido)propyl)carbamate (14)

A solution of Boc_2O (2.75 g, 12.6 mmol) in tetrahydrofuran (8 mL) was added dropwise, in a nitrogen atmosphere, to a stirred solution of **3** (5.25 g, 0.012 mol) in triethylamine (5.1 ml, 0.037 mol) cooled with an ice bath. When the addition was complete, the cooling bath was removed and the mixture was stirred at rt overnight. The reaction was quenched with 100 mL of water and extracted with ethyl acetate (4x100 mL). The combined organic extracts were dried with anhydrous Na_2SO_4 and evaporated under reduced pressure affording 6.4 g of a yellowish oil which was purified by crystallization from hot toluene (an ice bath was used to increase the crystallization rate) to obtain **14** as white needle-like crystals (2.95 g. 58%).

^{1}H-NMR (400 MHz, $CDCl_3$): δ (ppm) = 1.48 (s, 9H), 1.74-1.81 (m, 4H), 3.34 (br s, 8H), 6.50 (s, 1H), 8.16 (s, 1H).

Synthesis of tert-butyl bis(3-aminopropyl)carbamate (15)

120 mL of 0.2 M sodium hydroxide in methanol was dropwise added to a stirred solution of **14** (4 g, 9.45 mmol) in 100 mL of methanol at 0° C under nitrogen atmosphere. When the addition was complete, the cooling bath was removed and the mixture was stirred at overnight at room temperature. The solvent was evaporated under reduced pressure obtaining an oily residue that was suspended in 100 mL of water and extracted with chloroform (4x150 mL). The combined organic extracts were dried with anhydrous Na_2SO_4 and evaporated under reduced pressure to obtain **15** as a yellow/orange oil (2.46 g, 100%).

^{1}H-NMR (400 MHz, $CDCl_3$): δ (ppm) = 1.44 (s, 9H), 1.63 (quint, 4H, *J* = 6.9 Hz), 2.67 (t, 4H, *J* = 6.6 Hz), 3.21-3.27 (m, 4H).

Synthesis of tert-butyl N,N-bis(3-(2-ethoxy-3,4-dioxocyclobut-1-en-1-yl)aminopropyl)carbamate (16)

Over a period of 3 h a solution of 3,4-diethoxycyclobut-3-ene-1,2-dione (**7**) (4.45 g, 26.2 mmol) in tetrahydrofuran (50 mL) was added to a stirred solution of **15** (2.75 g, 11.9 mmol) in tetrahydrofuran (60 mL) under nitrogen atmosphere. The mixture was stirred at room temperature for 96 h, then the solvent was evaporated under reduced pressure affording a yellow oil. The crude product was triturated with ethyl ether and filtered to obtain **16** as a pale-yellow wax (5.1 g, 89%).

^{1}H-NMR (400 MHz, $CDCl_3$): δ (ppm) = 1.41-1.50 (m, 13H), 1.85 (t, 6H, *J* = 6.9 Hz), 3.33 (br s, 4H), 3.47 (br s, 2H), 3.63 (br s, 2H), 4.74 (q, 4H, *J* = 7.0 Hz), 7.55 (br s, 1H).

Synthesis of 6,19-bis(*tert*-butyloxycarbonyl)-12,13,25,26-tetraoxo-2,6,10,15,19,23-hexaazatricyclo[22.2.0.0(11,14)]hexaicosa-1(24),11(14)-diene (17)

Over a period of 6 h a solution of **15** (0.19 g, 0.83 mmol) in ethanol (100 mL) was added dropwise to a stirred solution of **16** (0.40 g, 0.83 mmol) in ethanol (100 mL). The reaction mixture was stirred at room temperature for 72 h. The white precipitate that formed was filtered, washed with ethanol affording pure **17** as white solid (0.34 g, 66%).

^{1}H-NMR (400 MHz, DMSO-d_6): δ (ppm) = 1.37 (s, 18H), 1.72 (br s, 8H), 3.18 (br s, 8H), 3.47 (br s, 8H), 7.43 (br s, 4H).

Synthesis of 12,13,25,26-tetraoxo-2,6,10,15,19,23-hexaazatricyclo[22.2.0.0(11,14)]hexaicosa-1(24),11(14)-diene bis trifluoroacetate (L5·2CF$_3$COOH)

Compound **17** (0.34g, 0.55 mmol) was dissolved in 5 mL of trifluoroacetic acid cooled at 0° C and vigorously stirred for 8 h to warm at room temperature. The reaction mixture was added dropwise to 100 mL of diethyl ether in an ice bath obtaining the trifluoroacetate salt of **L5** as white solid that was filtered and washed with cold diethyl ether. Obtained 0.35 g of **L5** (quantitative yield).

^{1}H-NMR (400 MHz, DMSO-d_6): δ (ppm) = 1.82 (br s, 8H), 2.91 (br s, 8H), 3.61 (br s, 8H), 7.68 (br s, 4H), 8.45 (br s, 4H).

^{13}C-NMR (100 MHz, DMSO-d_6): δ (ppm) = 28.1, 40.7, 45.1, 168.4, 182.9.

Elemental analysis for $C_{24}H_{32}N_6O_8F_6$: calcd C 44.59, H 4.99, N 13.00; found C 44.5, H 5.1, N 12.9.

3.2.4 Synthesis and Characterization of L6 and L7

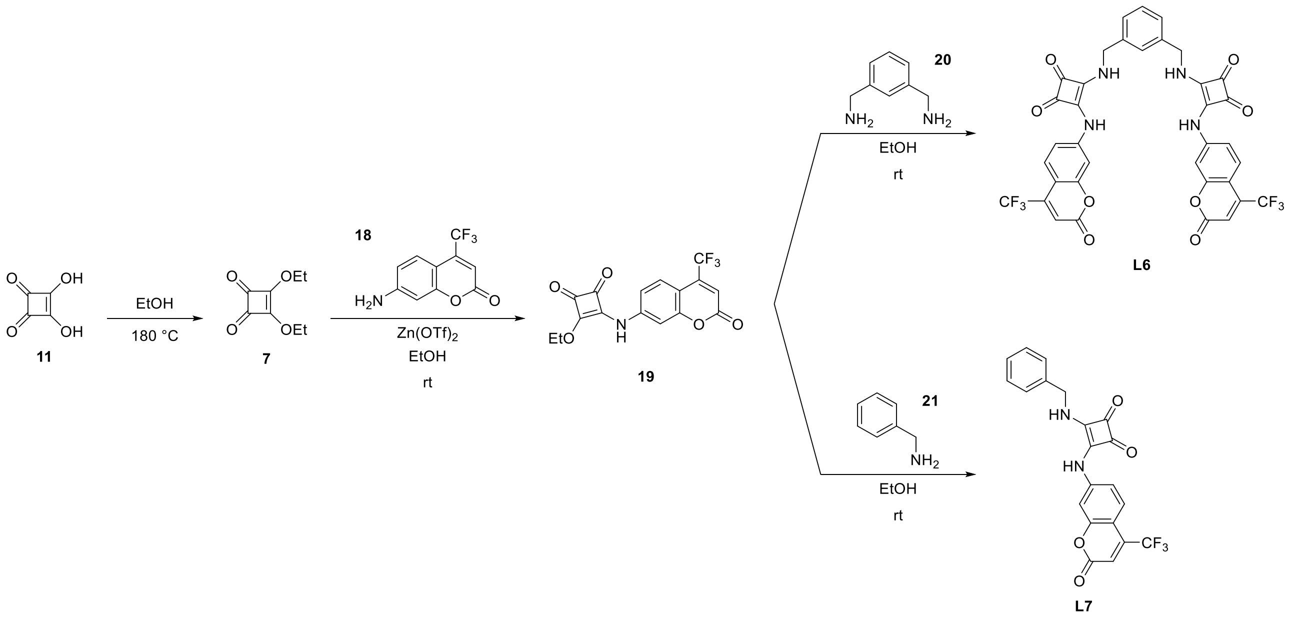

Synthesis of 3-ethoxy-4-((2-oxo-4-(trifluoromethyl)-2H-chromen-7-yl)amino)cyclobut-3-ene-1,2-dione (19)[34]

To a stirred solution of **7** (890 mg, 5.24 mmol) and zinc trifluoromethanesulfonate (160 mg, 0.436 mmol) in in the minimum amount of ethanol at room temperature was added 7-amino-4-(trifluoromethyl)coumarin (**18**) (1 g, 4.36 mmol) as a warm and clear solution in a volume to reach 40 mL of ethanol. The reaction was stirred overnight at room temperature. The yellow precipitate formed was filtered, washed with few ethanol and vacuum dried yielding **19** as a yellow solid (585 mg, 76%).

^{1}H-NMR (400 MHz, DMSO-d_6): δ (ppm) = 1.46 (t, 3H, J = 7.1 Hz), 4.83 (q, 2H, J = 7.1 Hz), 6.91 (s, 1H), 7.48 (dd, 1H, J_1 = 8.8 Hz J_2 = 2.3 Hz), 7.59 (d, 1H, J = 2.3 Hz), 7.70 (dd, 1H, J_1 = 8.8 Hz J_2 = 1.8 Hz), 11.17 (s, 1H).

Synthesis of 4,4'-((1,3-phenylenebis(methylene))bis(azanediyl))bis(3-((2-oxo-4-(trifluoromethyl)-2H-chromen-7-yl)amino)cyclobut-3-ene-1,2-dione) (L6)

To a stirred and warm suspension of **19** (100 mg, 0.283 mmol) in ethanol (50 mL) was added **20** (19 µL, 0.142 mmol). At the same time as the addition of the amine, the suspension turns from yellow to intense red. The suspension was stirred overnight at room temperature. The suspension was immersed in an ice bath to favour the sedimentation of the precipitate and the solid was further filtered, washed with few ethanol and vacuum dried yielding **L6** as a red/orange solid (95 mg, 89%).

^{1}H-NMR (400 MHz, DMSO-d_6): δ (ppm) = 4.87 (d, 4H, J = 5.2 Hz), 6.81 (s, 2H), 7.26 (dd, 2H, J_1 = 8.8 J_2 = 2.2 Hz), 7.34 (d, 2H, J = 7.5 Hz), 7.37 (s, 1H), 7.43 (t, 1H, J = 7.7 Hz), 7.57 (d, 2H, J = 8.1 Hz), 7.74 (s, 2H), 8.33 (s, 2H), 10.28 (br s, 2H).

^{13}C-NMR (100 MHz, DMSO-d_6): δ (ppm) = 48.7. 106.6, 111.0, 112.5 (d, J = 6.0 Hz), 113.0, 123.0 (q, J = 284.2 Hz), 124.9, 125.0, 126.7, 128.3, 137.4 (d, J = 32.1 Hz), 143.5, 144.0, 146.1, 155.0, 155.4, 160.8, 183.0, 187.0.

Elemental analysis for $C_{36}H_{20}F_6N_4O_8$: calcd C 57.61, H 2.69, N 7.46; found C 57.4, H 2.8, N 7.5.

(ESI): *m/z* calcd. for $C_{40}H_{42}N_6O_6S$: 750.12; found: 751.1 $[M+H]^+$.

Synthesis of 3-(benzylamino)-4-((2-oxo-4-(trifluoromethyl)-2H-chromen-7-yl)amino)cyclobut-3-ene-1,2-dione (L7)

To a stirred and warm suspension of **19** (100 mg, 0.283 mmol) in ethanol (50 mL) was added **21** (47 µL, 0.425 mmol). At the same time as the addition of the amine, the suspension turns from yellow to intense red. The suspension was stirred overnight at room temperature. The suspension was immersed in an ice bath to favour the sedimentation of the precipitate and the solid was further filtered, washed with few ethanol and vacuum dried yielding **L7** as a orange/yellow solid (83 mg, 71%).

^{1}H-NMR (400MHz, DMSO-d_6): δ (ppm) = 4.84 (d, 2H, J = 6.2 Hz), 6.87 (s, 1H), 7.31 (dd, 1H, J_1 = 8.8 J_2 = 2.3 Hz), 7.33-7.38 (m, 1H), 7.38-7.46 (m, 4H), 7.67 (dd, 1H, J_1 = 8.6 J_2 = 1.8 Hz), 7.81 (s, 1H), 8.17 (s, 1H), 10.15 (s, 1H).

^{13}C-NMR (100 MHz, DMSO-d_6): δ (ppm) = 47.8, 105.8, 107.9, 114.0 (d, J = 6.0 Hz), 115.6, 125.0 (q, J = 284.2 Hz), 128.1, 128.2, 129.2, 138.5, 139.8 (d, J = 32.1 Hz), 143.9, 155.8, 159.1, 162.9, 163.5, 170.1, 180.7, 185.5.

Elemental analysis for $C_{21}H_{13}F_3N_2O_4$: calcd C 60.88, H 3.16, N 6.76; found C 60.8, H 3.2, N 6.7.

(ESI): m/z calcd. for $C_{21}H_{13}F_3N_2O_4$: 414.08; found: 415.1 $[M+H]^+$.

3.2.5 Synthesis and Characterization of L8

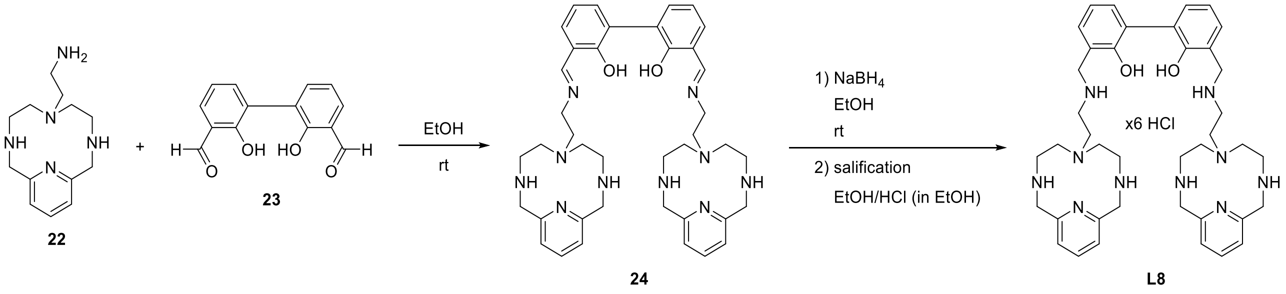

Synthesis of 3,3'-bis(((2-(3,6,9-triaza-1(2,6)-pyridinacyclodecaphane-6-yl)ethyl)imino)methyl)-[1,1'-biphenyl]-2,2'-diol (24)

97.11 mg of the amine **22** (0.39 mmol) were dissolved in 2 mL of ethanol in a round-bottomed flask and the solution was stirred in a nitrogen atmosphere. 47.17 mg of the aldehyde **23** (0.19 mmol) was subsequently added dropwise after solubilization in 3 mL of ethanol. The reaction was stirred at rt for at least 5 hours. Reaction progress was monitored by TLC (silica/EtOAc) up to total disappearances of **23**. The mixture thus obtained was used as it is in the next step without any purification or characterization.

3,3'-bis(((2-(3,6,9-triaza-1(2,6)-pyridinacyclodecaphane-6-yl)ethyl)amino)methyl)-[1,1'-biphenyl]-2,2'-diol hexahydrochloride (L8·6HCl)

In the previous round-bottomed flask, 37.48 mg of $NaBH_4$ (0.99 mmol) were added in small portions and it was then left to stir at rt with a $CaCl_2$ cap for at least 3 hours. During this time, an excess of 20 mg of $NaBH_4$ (0.53 mmol) was added. The progress of the reaction was monitored by TLC (alumina/EtOAc): the reaction was stopped when a purple spot appears (**24** has a yellow colour, both substances have Rf = 0). The suspension was filtered to remove solid residues and the solution was subsequently dried under reduced pressure. 6 mL of H_2O were added and then it was extracted with

CH_2Cl_2 (4x10 mL). The combined organic extracts were dried with anhydrous Na_2SO_4, filtered and evaporated under reduced pressure. The product thus obtained was dissolved again in EtOH to which HCl (in EtOH solution) was added – few drops of acetone were added to help the precipitation process. The product was thus precipitated and purified as white hexahydrochloride salt (98 mg, 54.25%).

^{1}H-NMR (400 MHz, D_2O): δ (ppm) = 2.83 (t, 8H, *J* = 5.2 Hz), 3.02 (t, 4H, *J* = 7.6 Hz), 3.18 (t, 8H), 3.26 (t, 4H, *J* = 7.7 Hz), 4.25 (s, 4H), 4.52 (s, 8H), 7.03 (t, 2H, *J* = 7.7 Hz), 7.33 (dd, 2H, J_1 = 7.8 Hz J_2 = 1.3 Hz), 7.36 (d, 6H), 7.88 (t, 2H, *J* = 7.8 Hz).

^{13}C-NMR (100 MHz, D_2O): δ (ppm) = 42.6, 45.9, 47.5, 49.5, 50.5, 50.8, 118.9, 121.4, 122.2, 125.0, 132.1, 133.5, 139.8, 148.9, 152.6.

Elemental analysis for $C_{40}H_{62}Cl_6N_{10}O_2$: calcd C 51.79, H 6.74, N 15.10; found C 51.8, H 6.7, N 15.2.

3.2.6 Synthesis and Characterization of L9

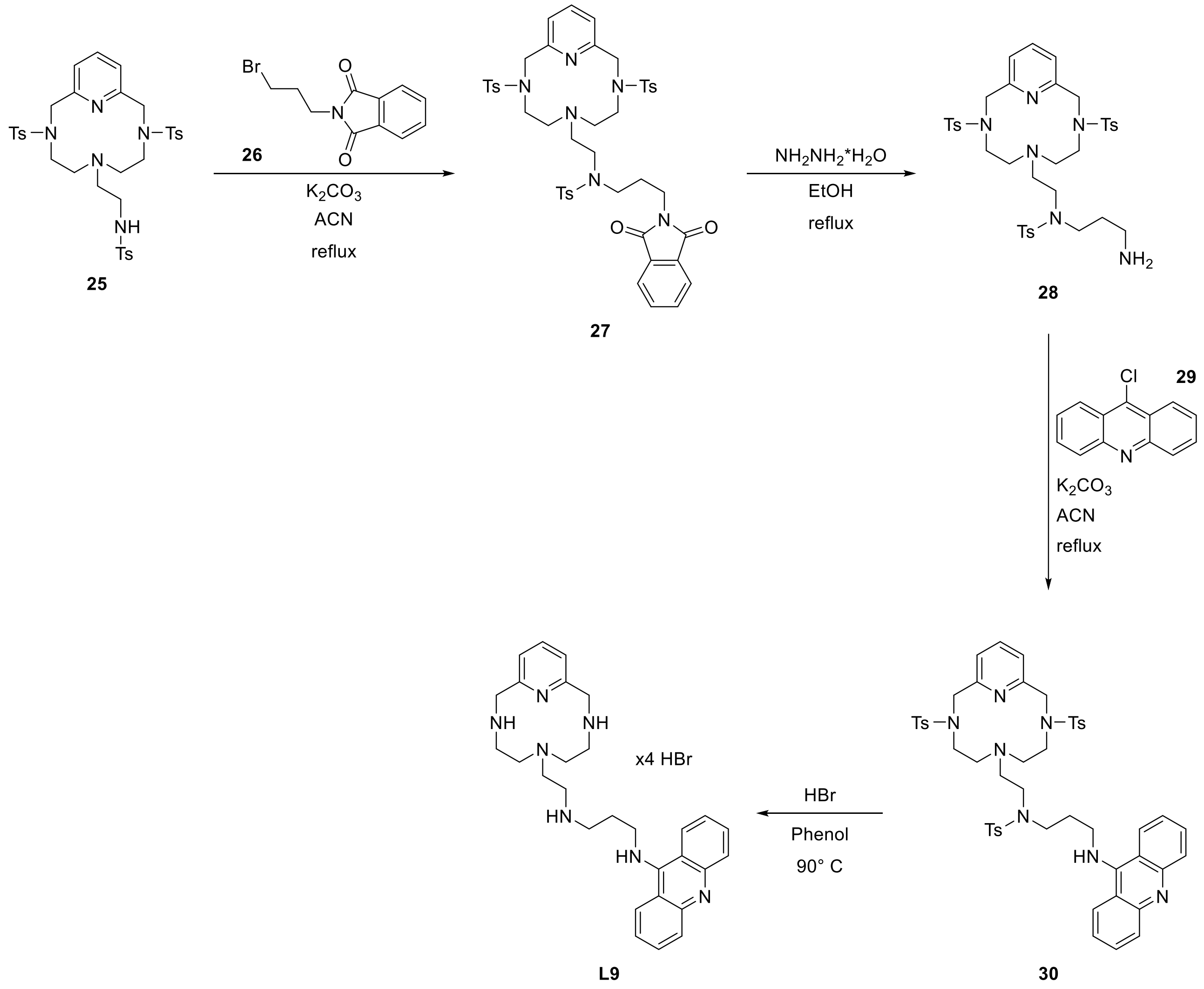

Synthesis of N-(3-(1,3-dioxoisoindolin-2-yl)propyl)-N-(2-(3,9-ditosyl-3,6,9-triaza-1(2,6)-pyridinacyclodecaphane-6-yl)ethyl)-4-methylbenzenesulfonamide (27)

4.32 g of **25** (6.07 mmol), 2.12 g of **26** (7.89 mmol) and 6.71 g of K_2CO_3 (48.55 mmol) were added together to a 200 mL of acetonitrile in a round-bottomed flask. The reaction mixture was reacted for 36 hours to reflux in nitrogen atmosphere. The resulting mixture was filtered, the carbonate salts were washed with acetonitrile and the solution was evaporated under reduced pressure to obtain quantitatively **27** as a yellow/orange foam (5.95 g, 100%). The product is used in the next step without any further purification.

Synthesis of N-(3-aminopropyl)-N-(2-(3,9-ditosyl-3,6,9-triaza-1(2,6)-pyridinacyclodecaphane-6-yl)ethyl)-4-methylbenzenesulfonamide (28)

5.95 g of **27** (6.62 mmol), were added to a 300 mL of ethanol in a round-bottomed flask and the mixture was refluxed in a nitrogen atmosphere until complete solubilization of the starting. Once the reagent has completely dissolved and a clear solution is obtained, 3.85 mL of hydrazine (79.41 mmol) were added. The reaction mixture was reacted for 24 hours to reflux in nitrogen atmosphere. After 24 hours the reaction appears as a slight suspension which was filtered to remove the white solid once cooled, it was washed with ethanol and the solution was vacuum dried to obtain a yellow oil. The oil was dissolved in dichloromethane to selectively solubilize the product getting another suspension which was filtered again and vacuum dried yielding **28** as a white/yellow foam (4.49 g, 88.23%).

^{1}H-NMR (300 MHz, $CDCl_3$): δ (ppm) = 1.63 (quint, 2H, J = 6.9 Hz), 2.35 (t, 4H, J = 7.7 Hz), 2.41 (s, 3H), 2.44 (s, 6H), 2.54 (t, 2H, J = 7.6 Hz), 2.71 (t, 2H, J = 6.6 Hz), 2.98 (t, 2H, J = 7.5 Hz), 3.08-3.18 (m, 6H,), 4.32 (s, 4H), 7.26 (s, 1H), 7.28 (s, 1H), 7.33 (td, 6H, J_1 = 9.1 Hz J_2 = 0.7 Hz), 7.67-7.77 (m, 7H).

Synthesis of N-(3-(acridin-9-ylamino)propyl)-N-(2-(3,9-ditosyl-3,6,9-triaza-1(2,6)-pyridinacyclodecaphane-6-yl)ethyl)-4-methylbenzenesulfonamide (30)

A solution of 333 mg of **29** (1.56 mmol) in 40 mL of warm acetonitrile was slowly added dropwise to a stirred solution/suspension of 1.20 g of **28** (1.56 mmol) and 2.16 g of K_2CO_3 (15.60 mmol) in 10 mL of acetonitrile. The reaction mixture was reacted for 72 hours in the dark to reflux. Reaction progress was monitored by TLC chromatography (SiO_2, DCM/MeOH 10:0.5). The carbonate in suspension was filtered and washed well with acetonitrile and the solution was then vacuum dried to obtain a dark orange foam. A silica gel flash chromatography was used to separate all impurities and recover the desired product (condition the column with DCM only and gradient elute up to

DCM/MeOH 100:10). The desired spot was recovered, and it was vacuum dried yielding **30** as an orange solid (420 mg, 28.45%).

^{1}H-NMR (300 MHz, $CDCl_3$): δ (ppm) = 1.63 (quint, 2H, *J* = 7.0 Hz), 2.33-2.38 (m, 4H), 2.41 (s, 9H), 2.56 (t, 2H, *J* = 7.1 Hz), 3.05 (t, 2H, *J* = 7.4 Hz), 3.11 (t, 6H, *J* = 7.4 Hz), 3.26 (t, 2H, *J* = 6.3 Hz), 4.28 (s, 4H), 7.22 (s, 1H), 7.25 (s, 1H), 7.28 (s, 3H), 7.31 (s, 3H), 7.33-7.39 (m, 2H), 7.63-7.68 (m, 2H), 7.70 (s, 4H), 7.73 (s, 3H), 8.14 (d, 2H, *J* = 8.6 Hz), 8.22 (dd, 2H, J_1 = 8.8 J_2 = 0.7 Hz).

Synthesis of N1-(2-(3,6,9-triaza-1(2,6)-pyridinacyclodecaphane-6-yl)ethyl)-N3-(acridin-9-yl)propane-1,3-diamine tetrahydrobromide (L9·4HBr)

0.420 g of **30** (0.444 mmol), 2.00 g of phenol and 30 mL of "HBr, pure, 33%wt in glacial acetic acid solution" were added together in a round-bottomed flask. The reaction mixture was reacted for 24 hours to 90° C with a gas trap. Once cooled at room temperature the suspension was vacuum filtered to recover the solid which is immediately washed with EtOH and subsequently vacuum dried yielding **L9** as a bromine yellow salt (0.80 g, 18.60%). To purify it as much as possible it was washed with EtOH for 24 hours, centrifuged and then the solid was dried under vacuum.

^{1}H-NMR (300 MHz, $CDCl_3$): δ (ppm) = 2.29 (quint, 2H, *J* = 7.6 Hz), 2.85 (t, 4H, *J* = 5.4 Hz), 2.99 (t, 2H, *J* = 7.5 Hz), 3.13-3.29 (m, 8H), 4.13 (t, 2H, *J* = 7.2 Hz), 4.56 (s, 4H), 7.38 (d, 2H, *J* = 7.9 Hz), 7.42-7.51 (m, 2H), 7.61 (dd, 2H, J_1 =8.6 J_2 = 0.7 Hz), 7.82-7.89 (m, 2H), 7.91 (d, 1H, *J* =7.9 Hz), 8.22 (d, 2H, *J* = 8.3 Hz).

^{13}C-NMR (300 MHz, $CDCl_3$): δ (ppm) = 26.0, 43.3, 45.4, 45.6, 45.8, 49.4, 50.5, 50.8, 112.7, 118.4, 122.2, 123.9, 124.9, 135.3, 139.3, 139.8, 148.8, 158.0

Elemental analysis for $C_{29}H_{41}Br_4N_7$: calcd C 43.15, H 5.12, N 12.15; found C 43.2, H 5.1, N 12.2.

References

---

[1] J. W. Steed, J. L. Atwood, *Supramolecular Chemistry Second Edition,* **2009**

[2] B. Wang, E. V. Anlyn, *Chemosensors: Principle, Strategies and Application*, **2011**

[3] E. V. Anlyn, D. A. Dougherty, *Modern Physical Organic Chemistry*, **2006**

[4] K. A. Connors, *Binding constants – the measurement of molecular complex stability*, **1987**

[5] J. Polster, H. Lachmann, *Spectrometric Titrations: Analysis of Chemical Equilibria*, **1989**

[6] B. Valeur, *Molecular Fluorescence: Principles and Applications*, **2002**

[7] M. Formica, V. Fusi, L. Giorgi, M. Micheloni, *Coordination Chemistry Reviews*, **2012**, *256*, 170–192

[8] G. Fukuhara, *Journal of Photochemistry and Photobiology C: Photochemistry Reviews*, **2020**, *42*, 100340

[9] G. Ambrosi, C. Battelli, M. Formica, V. Fusi, L. Giorgi, E. Macedi, M. Micheloni, R. Pontellini, L. Prodi, *New Journal of Chemistry*, **2009**, *33*, 171–180

[10] L. Conti, N. Flore, M. Formica, L. Giorgi, M. Pagliai, L. Mancini, V. Fusi, B. Valtancoli, C. Giorgi, *Inorganica Chimica Acta*, **2021**, *519*, 120261

[11] Directive 2013/39/EU of the European Parliament and of the Council, *Official Journal of the European Union*, **12 August 2013**, L226/1–L226/17

[12] P. E. Rosenfeld, L. G. H. Feng, *Risks of Hazardous Wastes,* **2011**

[13] V. Geissen, H. Mol, E. Klumpp, G. Umlauf, M. Nadal, M. van der Ploeg, S. E. A. T. M. van de Zee, C. J. Ritsema, *International Soil and Water Conservation Research*, **2015**, *3*, 57–65

[14] Emerging Pollutants in Water and Wastewater, *https://en.unesco.org/emergingpollutants*

---

[15] N. Z. Arman, S. Salmiati, A. Aris, M. R. Salim, T. H. Nazifa, M. S. Muhamad, M. Marpongahtun, *Water*, **2021**, *13*, 3258

[16] E. A. Tyumina, G. A. Bazhutin, A. d. P. Cartagena Gómez, I. B. Ivshina, *Microbiology*, **2020**, *89*, 148–163

[17] A. Rastogi, M. K. Tiwari, M. M. Ghangrekar, *Journal of Environmental Management*, **2021**, *300*, 113694

[18] Y. He, A. A. M. Langenhoff, R. N. J. Comans, N. B. Sutton, H. H. M. Rijnaarts, *Science of the Total Environment*, **2018**, *630*, 1335–1342

[19] A. L. Moreno Ríos, K. Gutierrez-Suarez, Z. Carmona, C. G. Ramos, L. F. Silva Oliveira, *Chemosphere*, **2022**, *291*, 132822

[20] D. Smiljanić, B. de Gennaro, F. Izzo, A. Langella, A. Daković, C. Germinario, G. E. Rottinghaus, M. Spasojević, M. Mercurio, *Microporous and Mesoporous Materials*, **2020**, *298*, 110057

[21] G. D. Alkimin, A. M. V. M. Soares, C. Barata, B. Nunes, *Environmental Pollution*, **2020**, *265*, 114993

[22] *National Centre for Biotechnology Information*, **2022**

[23] F. Caroleo, G. Magna, M. L. Naitana, L. Di Zazzo, R. Martini, F. Pizzoli, M. Muduganti, L. Lvova, F. Mandoj, S. Nardis, M. Stefanelli, C. Di Natale, R. Paolesse, *Sensors*, **2022**, *22*, 2649

[24] R. H. Farahi, A. Passian, L. Tetard, T. Thundat, *ACS Nano*, **2012**, *6*, 4548–4556

[25] G. M. Romano, L. Mummolo, M. Savastano, P. Paoli, P. Rossi, L. Prodi, A. Bencini, *Chemical Communications*, **2022**, *58*, 7022–7025

---

[26] L. A. Marchetti, L. K. Kumawat, N. Mao, J. C. Stephens, R. B. P. Elmes, *Chem*, **2019**, *5*, 1398–1485

[27] (a) R. I. Storer, C. Aciro, L. H. Jones, *Chemical Society Reviews*, **2011**, *40*, 2330–2346; (b) R. W. Frederik, K. Harm-Anton, *Chemical Society Reviews*, **2013**, *42*. 8220–8236; (c) C. Xiong-Jie, L. Zhi, C. Wen-Hua, *Mini-Reviews in Organic Chemistry*, **2018**, *15*, 148–156; (d) V. S. Saez Talens, P. Englebienne, T. T. Trinh, W. E. M. Noteborn, I. K. Voets, R. E. Kieltyka, *Angewandte Chemie International Edition*, **2015**, *54*, 10502–10506; (e) R. Prohens, A. Portell, M. Font-Bardia, A. Frontera, *Crystal Growth Design*, **2014**, *14*, 2578–2587

[28] J. I. Lachowicz, G. Picci, P. Coni, V. Lippolis, M. Mamusa, S. Murgia, G. Pichiri, C. Caltagirone, *New Journal of Chemistry*, **2019**, *43*, 10336–10342

[29] G. Picci, M. Kubicki, A. Garau, V. Lippolis, R. Mocci, A. Porcheddu, R. Quesada, P. C. Ricci, M. A. Scorciapino, C. Caltagirone, *Chemical Communications*, **2020**, *56*, 11066–11069

[30] G. Picci, J. Milia, M. C. Aragoni, M. Arca, S. J. Coles, A. Garau, V. Lippolis, R. Montis, J. B. Orton, C. Caltagirone, *Molecules*, **2021**, *26*, 1301

[31] M. C. Rotger, M. N. Piña, A. Frontera, G. Martorell, P. Ballester, P. M. Deyà, A. Costa, *Journal of Organic Chemistry*, **2004**, *69*, 2302–2308

[32] A. J. Sindt, M. D. Smith, P. J. Pellechia, L. S. Shimizu, *Crystal Growth Design*, **2018**, *18*, 1605–1612

[33] L. Qin, A. Hartley, P. Turner, R. B. P. Elmes, K. A. Jolliffe, *Chemical Science*, **2016**, *7*, 4563–4572

[34] A. Rostami, A. Colin, X. Y. Li, M. G. Chudzinski, A. J. Lough, M. S. Taylor, *Journal of Organic Chemistry*, **2010**, *75*, 3983–3992

---

[35] D. Quiñonero, A. Frontera, P. Ballester, P. M Deyà, *Tetrahedron Letters*, **2000**, *41*, 2001–2005

[36] G. Ambrosi, M. Formica, V. Fusi, L. Giorgi, A. Guerri, M. Micheloni, P. Paoli, R. Pontellini, P. Rossi, *Chemistry – A European Journal*, **2007**, *13*, 702–712

[37] G. Ambrosi, M. Formica, V. Fusi, L. Giorgi, E. Macedi, M. Micheloni, P. Paoli, R. Pontellini, P. Rossi, *Chemistry – A European Journal*, **2011**, *17*, 1670–1682

[38] V. Amendola, L. Fabbrizzi, L. Mosca, F.-P. Schmidtchen, *Chemistry European Journal*, **2011**, *17*, 5972–5981

[39] B. Verdejo, M. Inclán, M. P. Clares, I. Bonastre-Sabater, M. Ruiz-Gasent, E. García-España, *Chemosensors*, **2022**, *10*, 1–34

[40] K. Bowman-James, A. Bianchi, E. García-España, *Anion Coordination Chemistry*, **2012**

[41] (a) J. E. Richman, T. J. Atkins, *Journal of the American Chemical Society*, **1974**, *96*, 2228; (b) J. E. Richman, T. J. Atkins, W. F. Oetle, *Organic Synthesis*, **1988**; (c) b. L. Shaw, *Journal of the American Chemical Society*, **1975**, *97*, 3856

[42] B. Verdejo, A. Ferrer, S. Blasco, C. E. Castillo, J. González, J. Latorre, M. A. Máñez, M. G. Basallote, C. Soriano, E. García-España, *Inorganic Chemistry*, **2007**, *46*, 5707–5719

[43] (a) J. González, J. M. Llinares, R. Belda, J. Pitarch, C. Soriano, R. Tejero, B. Verdejoa, E. García-España, *Organic & Biomolecular Chemistry*, **2010**, *8*, 2367–2376; (b) M. Inclán, M. T. Albelda, J. C. Frías, S. Blasco, B. Verdejo, C. S., C. Salat-Canela, M. L. Díaz, A. García-España, E. García-España, *Journal of the American Chemical Society*, **2012**, *134*, 9644–9656; (c) M. Inclán, M. T. Albelda, E. Carbonell, S. Blasco, A. Bauzá, A. Frontera, E. García-España, *Chemistry European Journal*, **2014**, *20*, 3730–3741

---

[44] M. A. Ilies, W. A. Seitz, B. H. Johnson, E. L. Ezell, A. L. Miller, E. B. Thompson, A. T. Balaban, *Journal of Medicinal Chemistry*, **2006**, *49*, 3872–3887

[45] D. Genovese, M. Cingolani, E. Rampazzo, L. Prodi, N. Zaccheroni, *Chemical Society Reviews*, **2021**, *50*, 8414–8427

[46] A. Credi, L. Prodi, *Journal of Molecular Structure*, **2014**, *1077*, 30 – 39

[47] K. Burke, L. O. Wagner, *International Journal of Quantum Chemistry*, **2013**, *113*, 96–101

[48] W. Kohn, L. J. Sham, *Physical Review*, **1965**, *140*, A1133–A1138

[49] P. Makkar, N. N. Ghosh, *RSC Advances*, **2021**, *11*, 27897–27924

[50] W. Koch, M. C. Holthausen, *A Chemist's Guide to Density Functional Theory*, **2001**

[51] J. S. Arey, P. C. Aeberhard, I. C. Lin, U. Rothlisberger, *Journal of Physical Chemistry B*, **2009**, *113*, 4726–4732

[52] A. D. Boese, *ChemPhysChem*, **2015**, *16*, 978–985

[53] S. Kozuch, J. M. L. Martin, *Journal of Chemical Theory and Computation*, **2013**, *9*, 1918–1931

[54] A. Siiskonen, A. Priimagi, *Journal of Molecular Modeling*, **2017**, *23*

[55] C. Bleiholder, D. B. Werz, H. Köppel, R. Gleiter, *Journal of the American Chemical Society*, **2006**, *128*, 2666–2674

[56] A. P. M. Arca, G. Ciancaleoni, *Chalcogen Chemistry: Fundamentals and Applications*, **2023**

[57] W. Wang, B. Ji, Y. Zhang, *Journal of Physical Chemistry A*, **2009**, *113*, 8132–8135

[58] M. C. Aragoni, M. Arca, F. A. Devillanova, F. Isaia, V. Lippolis, *Crystal Growth and Design*, **2012**, *12*, 2769–2779

---

[59] R. Montis, M. C. Aragoni, M. Arca, S. J. Coles, V. Lippolis, J. Milia, J. B. Orton, L. Pala, G. Picci, T. Pivetta, C. Caltagirone, *European Journal of Inorganic Chemistry*, **2021**, *2021*, 3878–3885

[60] C. Adamo, V. Barone, *Journal of Chemical Physics*, **1998**, *108*, 664–675

[61] F. Weigend, R. Ahlrichs, *Physical Chemistry Chemical Physics*, **2005**, *7*, 3297–3305

[62] P. Rossi, P. Paoli, L. Chelazzi, S. Milazzo, D. Biagi, M. Valleri, A. Ienco, B. Valtancoli, L. Conti, *Crystal Growth and Design*, **2020**, *20*, 226–236

[63] A. Portell, R. Prohens, *Crystal Growth Design*, **2014**, *14*, 397–400

[64] P. Gans, A. Sabatini, A. Vacca, *Talanta*, **1996**, *43*, 1739–1753

[65] P. Gans, A. Sabatini, A. Vacca, *Annali di Chimica*, **1999**, *89*, 45–49

[66] T. K. Macklin, Victor Snieckus, *Organic Letters*, **2005**, *7*, 2519–2522

[67] D. A. Case, H. M. Aktulga et al., *Amber 2021*, University of California, San Francisco, **2021**

[68] L. Conti, N. Flore, M. Formica, L. Giorgi, M. Pagliai, L. Mancini, V. Fusi, B. Valtancoli, C. Giorgi, *Inorganica Chimica Acta*, **2021**, *519*, 120261

[69] A. Bianchi, E. García-España, *Journal of Chemical Education*, **1999**, *76*, 1727–1734

[70] *Gaussian 16*, *Revision C.01*, M. J. Frisch, G. W. Trucks, H. B. Schlegel, G. E. Scuseria, M. A. Robb, J. R. Cheeseman, G. Scalmani, V. Barone, G. A. Petersson, H. Nakatsuji, X. Li, M. Caricato, A. V. Marenich, J. Bloino, B. G. Janesko, R. Gomperts, B. Mennucci, H. P. Hratchian, J. V. Ortiz, A. F. Izmaylov, J. L. Sonnenberg, D. Williams-Young, F. Ding, F. Lipparini, F. Egidi, J. Goings, B. Peng, A. Petrone, T. Henderson, D. Ranasinghe, V. G. Zakrzewski, J. Gao, N. Rega, G. Zheng, W. Liang, M. Hada, M. Ehara, K. Toyota, R. Fukuda, J. Hasegawa, M. Ishida, T. Nakajima, Y. Honda, O. Kitao, H. Nakai, T. Vreven, K. Throssell, J. A. Montgomery, Jr., J. E. Peralta, F. Ogliaro, M. J.

Bearpark, J. J. Heyd, E. N. Brothers, K. N. Kudin, V. N. Staroverov, T. A. Keith, R. Kobayashi, J. Normand, K. Raghavachari, A. P. Rendell, J. C. Burant, S. S. Iyengar, J. Tomasi, M. Cossi, J. M. Millam, M. Klene, C. Adamo, R. Cammi, J. W. Ochterski, R. L. Martin, K. Morokuma, O. Farkas, J. B. Foresman, D. J. Fox, *Gaussian, Inc.*, *Wallingford CT*, **2016**

[71] C. Adamo, V. Barone, *The Journal of Chemical Physics*, **1998**, *108*, 664–675

[72] J. P. Perdew, K. Burke, Y. Wang, *Physical Review B*, **1996**, *54*, 16533–16539

[73] A. Schäfer, H. Horn, R. Ahlrichs, *The Journal of Chemical Physics*, **1992**, *97*, 2571–2577

[74] F. Weigend, R. Ahlrichs, *Physical Chemistry Chemical Physics*, **2005**,*7*, 3297–3305

[75] R. Dennington, T.A. Keith, J.M. Millam, *GaussView, Version 6, Semichem Inc.*, *Shawnee Mission, KS*, **2016**

[76] J.-L. Brisset, *Revue Roumaine de Chimie*, **1983**, *28*, 941–949

[77] E. García-España, M.-J. Ballester, F. Lloret, J.-M. Moratal, J. Faus, A. Bianchi, *Journal of the Chemical Society, Dalton Transactions*, **1988**, *1*, 101–104

[78] https://www.metrohm.com/en/service/software-center/tiamo.html

[79] (a) G. Gran, *Analyst*, **1952**, *77*, 661–671; (b) F. J. Rossotti, H. Rossotti, *Journal of Chemical Education*, **1965**, *42*, 375–378

Acknowledgments

Thanks to my colleagues at the Supramolecular Chemistry laboratory in Urbino:

- my Supervisor, Professor Vieri Fusi
- my Co-Supervisor, Professor Luca Giorgi
- Professor Mauro Formica
- Professor Eleonora Macedi
- Dr. Riccardo Montis
- Dr. Gianluca Ambrosi
- Dr. Roberto Pontellini
- Dr. Daniele Paderni
- Dr. Erika Palazzetti
- Dr. Daniele Lopez

And to my colleagues from the Supramolecular Chemistry group in Valencia:

- Professor Enrique García-España
- Dr. Mario Inclán

A heartfelt thanks also to the Supramolecular Chemistry teams of Bologna and Cagliari and their respective head:

- Professor Luca Prodi
- Professor Claudia Caltagirone